INFORMATION TO USERS

This manuscript has been reproduced from the microfilm master. UMI films the text directly from the original or copy submitted. Thus, some thesis and dissertation copies are in typewriter face, while others may be from any type of computer printer.

The quality of this reproduction is dependent upon the quality of the copy submitted. Broken or indistinct print, colored or poor quality illustrations and photographs, print bleedthrough, substandard margins, and improper alignment can adversely affect reproduction.

In the unlikely event that the author did not send UMI a complete manuscript and there are missing pages, these will be noted. Also, if unauthorized copyright material had to be removed, a note will indicate the deletion.

Oversize materials (e.g., maps, drawings, charts) are reproduced by sectioning the original, beginning at the upper left-hand corner and continuing from left to right in equal sections with small overlaps.

Photographs included in the original manuscript have been reproduced xerographically in this copy. Higher quality 6" x 9" black and white photographic prints are available for any photographs or illustrations appearing in this copy for an additional charge. Contact UMI directly to order.

ProQuest Information and Learning
300 North Zeeb Road, Ann Arbor, MI 48106-1346 USA
800-521-0600

Active Magnetic Regenerators: Performance in the Vicinity of Para-Ferromagnetic Second Order Phase Transitions

by

Andrew Michael Rowe
B.Eng., Royal Military College of Canada, 1992
M.A.Sc., University of Victoria, 1997

A Dissertation Submitted in Partial fulfillment of the Requirements for the Degree of

DOCTOR OF PHILOSOPHY

in the

Department of Mechanical Engineering

We accept this dissertation as conforming
to the required standard

Dr. J.A. Barclay, Supervisor (Department of Mechanical Engineering)

Dr. S. Dost, Member (Department of Mechanical Engineering)

Dr. H.W. King, Member (Department of Mechanical Engineering)

Dr. G. Bees, Outside Member (Department of Physics and Astronomy)

Dr. R. Chahine, External Examiner (Université du Québec à Trois-Rivières)

Supervisor: Dr. John A. Barclay

Abstract

A technology that has the potential to liquefy hydrogen and natural gas efficiently is an Active Magnetic Regenerative Liquefier (AMRL). An AMRL exploits the magnetocaloric effect displayed by magnetic materials whereby a reversible temperature change is induced when the material is exposed to a magnetic field. This effect can be used to produce cooling. By using the magnetic materials in a regenerator as the heat storage medium and as the means of work input, one creates an Active Magnetic Regenerator (AMR). Because the adiabatic temperature change is a strong function of temperature for most materials, to span a large temperature range such as that needed to liquefy hydrogen, a number of different materials may be needed to make up one or more regenerators. Single material AMRs have been proven, but layering with more than one material has not.

This thesis is a study of AMRs using magnetic refrigerants displaying second-order paramagnetic to ferromagnetic ordering. An analysis of AMR thermodynamics is performed and results are used to define properties of ideal magnetic refrigerants. The design and construction of a novel test apparatus consisting of a conduction-cooled superconducting solenoid and a reciprocating AMR test apparatus are described. A numerical model is developed describing the energy transport in an AMR. Experiments using Gd are performed and results are used to validate the model. A strong relationship between flow phasing is discovered and possible reasons for this phenomenon are discussed. Simulations of AMRs operating in unconventional modes such as at temperatures greater than the transition temperature reveal new insights into AMR behaviour. Simulations of two-material layered AMRs suggest the existence of a jump phenomenon occurring regarding the temperature span. These results are used to explain the experimental results reported by other researchers for a two-material AMR.

Examiners:

Dr. J.A. Barclay, Supervisor (Department of Mechanical Engineering)

Dr. S. Dost, Member (Department of Mechanical Engineering)

Dr. H.W. King, Member (Department of Mechanical Engineering)

Dr. G. Beer, Outside Member (Department of Physics and Astronomy)

Dr. R. Chahine, External Examiner (Université du Québec à Trois-Rivières)

Table of Contents

List of Figures

List of Tables

Nomenclature

Acronyms

AMR(R)	Active Magnetic Regenerator (Refrigerator)
MCE	Magnetocaloric Effect (adiabatic temperature change)
MR	Magnetic Refrigerator
RTD	Resistive Temperature Device

Symbols

A	Cross sectional area/ Surface area
B	Magnetic flux density
C	Capacity rate/ Geometric coefficient
c	Heat capacity
D	Diameter
E	Energy
F	Helmholtz potential
f	Friction factor
G	Mass flow per unit area
g	Landé g-factor
H	Magnetic field intensity
h	Heat transfer coefficient
I	Current
J	Total angular momentum
K	Thermal conductance/ Coupling parameter
k	Thermal conductivity/ Boltzmann constant
L	Inductance/ Length/ Orbital angular momentum
M	Magnetization
m	Mass/ Mass magnetization
N	Number of atoms/ demagnetizing factor
N_{tu}	Number of transfer units
P	Pressure
Q	Energy flux/ heat transfer
R	Heat capacity ratio

r	Radius
Re	Reynold's number
S,s	Entropy, entropy per unit mass/ Entropy generation/ Stroke/ Source/ Spin angular momentum
T	Temperature
t	Time
u	Velocity
W	Work

Greek

Φ	Utilization
α	Porosity
β	Balance/ Isothermal compressibility
γ	Molecular field coefficient
φ	Fluid thermal capacity
μ	Viscosity
μ_B	Bohr magneton
ρ	Density
σ	Refrigerant symmetry
τ	Period

Subscripts

ref	Reference value
Curie	Curie point
C	Cold
H	Hot
x	Location
low	Low
high	High
B	Constant field/ Blow
b	Bed
f	Fluid
P	Pressure/ particle

s	Solid
peak	Peak value
g	Generation
min	Minimum
max	Maximum
h	Hydraulic
eff	Effective
T	Total
M	Magnetic
rev	Reversible
irr	Irreversible
d	Demagnetizing/ Displacer
a	Applied
o	Outer
l	Inner

Superscripts

ideal	Ideal value
′	Per unit length
‴	Per unit volume
*	Non-dimensional value
¯	Average

Acknowledgements

Much of the work in this thesis would not have been possible without the financial support of the Natural Sciences and Engineering Research Council of Canada as well as Natural Resources Canada.

I would like to thank my advisor, John Barclay, for his support. This came in many ways, but there were some particular elements I would like to acknowledge. As anyone who has worked with John knows, his enthusiasm and real excitement with all aspects of applied science is infectious. As a result, I, too, became afflicted with this condition and it made me imagine trying things that previously I thought myself incapable of doing. John then gave me the resources and intellectual freedom to exercise these ideas. At times, this seemed overwhelming, but, after clearing my own small path through the forest of knowledge, the resulting feeling of satisfaction made the effort worthwhile.

I would also like to thank everyone in the group and department who provided valuable assistance by sharing their own expertise. Finally, the support of family and friends was a crutch I sometimes leaned on.

Chapter 1
Introduction

1.1 Background

Recently, there has been renewed interest in alternative energy carriers and technologies that rely on fuels other than oil [1]. In contemporary usage, alternative generally means liquid or gaseous fuels that have a lower carbon to hydrogen ratio than gasoline or diesel. More specifically, natural gas and hydrogen are alternative fuels. Hydrogen is considered the most desirable because there is no carbon, reaction with oxygen produces water, and it is considered relatively safe. One topical issue driving research in alternative fuels is the impact of global carbon emissions on the environment.

A more distant perspective shows that a general trend in the evolution of the energy system over the past 150 years has been the movement towards decarbonization. If this trend continues, then one can imagine a time when system evolution would bring what some call a Hydrogen Age, a time when hydrogen is the dominant energy carrier replacing fossil fuels. Regardless of the forces driving this evolution, there are some clear difficulties impeding the broad use of gaseous fuels such as methane and hydrogen [2].

Although gaseous methane is already used widely in stationary applications, and it would seem that gaseous hydrogen could be employed in a similar manner, research is largely focused on mobile use. One of the reasons for this is that transportation consumes approximately one third of all fossil fuels in North America, most of this as liquid hydrocarbons [3]. The use of natural gas and hydrogen in transport is limited by the low volumetric energy density associated with the gaseous state at moderate pressures. Storage of these fuels in sufficient quantity to provide consumers with vehicle ranges of 400 kilometres or greater is an area of intense research. For a fuel cell vehicle running on hydrogen, it is estimated that approximately 4 kg must be stored to satisfy this range constraint [4].

Various storage technologies are being pursued. In the case of hydrogen, some of the better-known methods are: compressed gas, metal hydrides and liquid hydrogen. There are other ideas that are in development; however, their utility is still in question. For natural gas, compression and liquefaction seem to be the only two established methods. If one were to gauge the viability of these various storage means for hydrogen by surveying the literature, it would appear that there

is no clear winner. One of the key drawbacks in using liquid hydrogen is the large amount of energy needed to liquefy the gas. The ideal work needed to liquefy hydrogen is 10% of the lower heating value whereas for methane it is 2%. If these gases are liquefied using a device with a second law efficiency of 40%, the work to liquefy hydrogen would be 25% of the lower heating value and for methane only 5%. If liquefier efficiency scales with the refrigeration temperature as is suggested by [57], then hydrogen becomes a more difficult challenge. At atmospheric pressure, hydrogen liquefies at a temperature of approximately 20 K; methane liquefies near 110 K.

The above considerations suggest that liquefying methane with conventional technologies is a reasonable way to store the fuel. On the other hand, the viability of storing hydrogen as a liquid appears to rely on a technological breakthrough in liquefier efficiency. Devices using magnetic refrigerants may be a solution to this problem as well as an efficient means of refrigeration from room temperature to the cryogenic regime. A brief description of the ideas behind these devices and their history follows.

1.2 Magnetic Refrigeration

The reversible temperature change induced in some magnetic materials by the application of a magnetic field is known as the magnetocaloric effect, originally discovered by Warburg [6] in iron. The use of this effect to produce cooling was suggested by Debye [7] and Giauque, and was subsequently proven by the latter to produce a low temperature of near 0.5 K [8]. The method used in this experiment created a "one shot" cooling whereby the material is isothermally magnetized and then adiabatically demagnetized to decrease the temperature of a sample for a limited amount of time. A means of producing continuous cooling was suggested by Daunt and Heer in 1949 [9]. A magnetic Carnot cycle was proposed in which the material undergoes isothermal magnetization, adiabatic demagnetization, isothermal demagnetization and heat absorption, and adiabatic magnetization to return to the initial conditions. In 1954 Heer *et al.* built a continuous magnetic refrigerator (MR) producing temperatures below 0.2 K [10].

Until the 1970s, magnetic refrigeration remained a means of cooling for low temperatures only. For a material to have a significant magnetocaloric effect, the magnetic entropy change must be large relative to the total entropy of the material. At low temperatures, the lattice and electronic contributions to the entropy are relatively small; however, the lattice component increases as a cubic function of temperature while the electronic component increases as a linear function of temperature. Thus, with moderate field changes, it was presumed that magnetic cooling was only effective at low temperatures where small magnetic entropy changes are relatively large

compared to the total entropy. In the sixties, superconducting magnets became more readily available providing larger field strengths and increasing the useable magnetocaloric effect.

In the 1970s, some exciting progress in magnetic refrigeration occurred at Los Alamos National Laboratory. One of the reasons for these new developments was due to a report by van Geuns [11] suggesting that a regenerator be used with a paramagnetic material to produce a MR from 4 to 15 K. The realization that temperature spans could be increased by using regeneration to remove lattice entropy led to research on devices with larger temperature spans using Ericsson cycles instead of Carnot cycles. The other breakthrough came with the work of Brown [12]. He demonstrated magnetic refrigeration near room temperature using a ferromagnetic substance as the working material. Prior to this, paramagnetic materials were used as the working substance. Research on a number of different devices, in particular rotating and reciprocating geometries, quickly followed [13-16].

In the early 1980s, research into magnetic refrigeration could be divided into two sub-problems: device design, and material research. Rare earth elements were characterized as potential refrigerant materials while alloying these materials with other lanthanides and transition metals was an area of intense activity. Researchers at several labs focused on the engineering problems associated with magnetic devices. A new concept was introduced by Barclay in 1982 that became known as an Active Magnetic Regenerator (AMR) [17]. Unlike previous gas cycles, or magnetic cycles, the AMR concept coupled what had been two separate processes into a single component. Instead of using a separate material as a regenerator to *recuperate* the magnetic material, the AMR made use of the refrigerant itself as the regenerator. In essence, a temperature gradient is established throughout the AMR and a fluid is used to transfer heat from the cold end to the hot. This subtle but important idea produced a new magnetic cycle distinct from Carnot, Ericsson, Brayton, or Stirling. In the AMR, *each section* of the bed undergoes its own cycle; the entire mass of working material no longer experiences a similar cycle where all the material temperatures are the same. The AMR concept was given further complexity by another new idea, the use of multiple magnetic refrigerants in a single AMR.

At the time, interest in magnetic refrigeration intensified for two main reasons: (1) the materials of interest were those undergoing a second-order magnetic phase transition i.e. order-disorder, in which the magnetocaloric effect is highly reversible; and, (2) the working substance is a solid with high volumetric entropy compared to a gas. The first item means that device efficiencies could be significantly higher than gas cycles while the second suggests that magnetic devices could have high power densities; thus, be small in size.

In hindsight, the 1980s can be seen as the years where the AMR concept was proposed, spread to other labs and researchers, and proven in novel devices. Many of these devices were focused on the 77 to 20 K range to liquefy hydrogen. With increased activity in the field, the complex interactions between device and regenerator design, material development and system integration revealed new and unexpected problems. Many of the difficulties were engineering; however, it became clear that the fundamental thermodynamic interactions in the AMR demanded further research as well [24].

The past decade has been one of mixed progress for magnetic refrigeration. Materials research is prolific [25, 26] and there have been some interesting new alloys discovered that have the potential to be good magnetic refrigerants. In particular, a series of ternary alloys in the $Gd_5(Si_xGe_{1-x})_4$ family was found to display high entropy changes due to a first-order phase transition [27]. Although this material was touted to be a breakthrough in magnetocaloric materials, subsequent work has shown that there may be reason to question this claim [28]. The phase change in this material is reported to be a magnetic-crystallographic transformation, and there is significant hysteresis in the magnetization curves for the $x = 0.5$ species. More recently, a transition metal based compound, $MnFeP_{0.45}As_{0.55}$, has been reported to have a large magnetic entropy change near room temperature again due to a first order phase change [29]. The entropy change for this material was determined using magnetization data only, but not the adiabatic temperature change so it is still not clear how promising this material is.

At the start of the last decade devices tended towards the 77 –20 K temperature range and then seemed to progress to room temperature as time went on [30-34]. The Cryofuels group at the University of Victoria began working on a rotary AMR to liquefy natural gas. The intended temperature span was from 240 to 110 K and used an AMR made up of five different magnetic refrigerants. In 1998 researchers at Astronautics Corporation reported a room-temperature device using Gd refrigerant and a water-glycol heat transfer fluid. The cooling power of this device was high, but more significantly, they were able to show refrigeration with an applied field as low as 1.7 Tesla [34]. In collaboration with Ames Lab, this work is now being directed towards the development of a commercial refrigerator near room temperature using permanent magnets [35]. Significantly, all research concerning MR devices operating above 20 K is now using the AMR concept.

1.2.1 The Active Magnetic Regenerator

In contemporary materials, the magnetocaloric effect is a strong non-linear function of temperature. In addition, it is a function of the magnitude of the field change and the initial field strength. For most magnetic materials, the magnetocaloric effect is modest even near the transition temperature. Near room temperatures, a material with an adiabatic temperature change larger than 2 K/Tesla is unusual. For example, a sample of gadolinium near room temperature will exhibit a temperature change of approximately 10 K with the application of a 5 Tesla magnetic field. Gadolinium is considered one of the best-known magnetocaloric materials. Until recently, because the MCE increases with field strength, superconducting magnets were used almost exclusively in MR devices. Figure 1.1 shows experimental data taken from Dan'kov *et al.* for Gd with a field change from 0 to 2 Tesla [36].

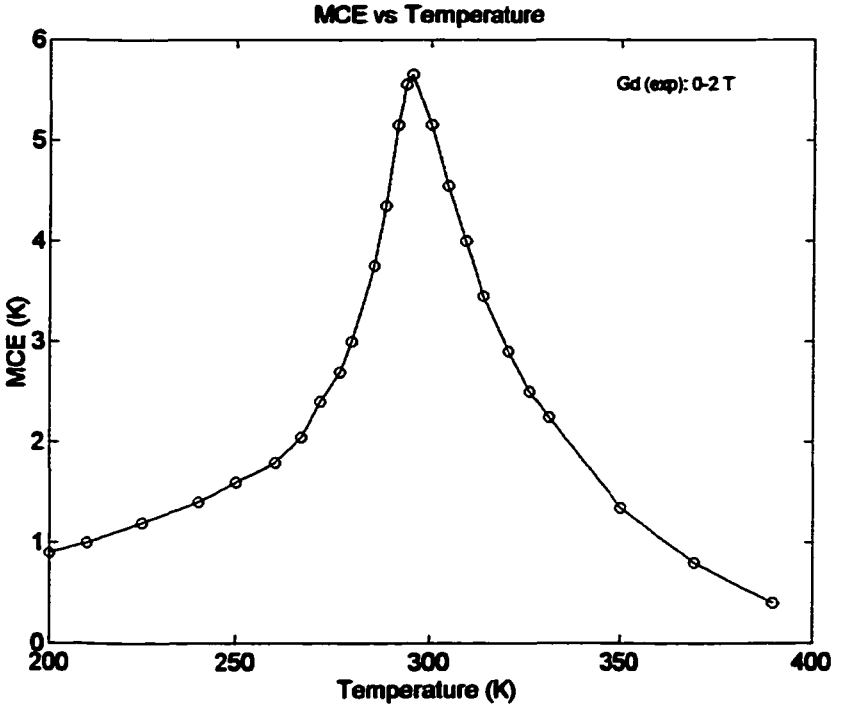

Figure 1.1 Adiabatic temperature change in Gd for a magnetic field change from 0 to 2 T [36].

Gadolinium undergoes a second-order phase transition at a temperature near 294 K. Above this temperature Gd behaves like a paramagnetic material i.e. there is no long range order, and as the temperature decreases it spontaneously transforms to a ferromagnet at the Curie temperature. This spontaneous formation of ordered magnetic domains causes a large change in entropy to occur over a relatively small temperature span. Near the phase transition region, the application of a

magnetic field can produce significant ordering (magnetization) and therefore a magnetic entropy change. If magnetization or demagnetization is performed isentropically, the lattice entropy (assuming electronic contributions are small) is changed by an amount equivalent to the magnetic entropy change and therefore a temperature difference is produced in the material. If the total entropy is written as a function of temperature, T, and applied field, H, a differential change in entropy can be written

$$ds(T,H)=\left(\frac{\partial s}{\partial T}\right)_H dT+\left(\frac{\partial s}{\partial H}\right)_T dH\,, \tag{1.1}$$

where s is the entropy per unit mass. Using the definition of heat capacity, the above can be rewritten as,

$$ds(T,H)=\frac{c_H(T,H)}{T}dT+\left(\frac{\partial s}{\partial H}\right)_T dH\,. \tag{1.2}$$

If an isentropic field change is produced, the temperature change is,

$$dT=-\frac{T}{c_H(T,H)}\left(\frac{\partial s}{\partial H}\right)_T dH\,. \tag{1.3}$$

If Maxwell's relations for the equivalence of the second derivatives hold, the partial derivative in parentheses can be replaced to give

$$dT=-\frac{T}{c_H(T,H)}\left(\frac{\partial m(T,H)}{\partial T}\right)_H dH\,, \tag{1.4}$$

where m is the mass magnetization.

From this simple explanation, one can deduce that a material with no significant work modes other than magnetic should have a high ratio of magnetic entropy change to total entropy to produce a large adiabatic temperature change. However, magnetic entropy alone is insufficient to classify a refrigerant as being useful since the heat capacity is not a constant.

As can be seen in Figure 1.1, for a 0 to 2 Tesla field change in Gd the MCE is slightly less than 6 K at the transition temperature. And, the MCE decreases quickly as the temperature is moved away from the Curie point. This behaviour is the reason that non-regenerative magnetic cycles are not feasible at higher temperatures (>20 K). It is difficult to produce a useful temperature span based on a Carnot cycle when the effective isentropic temperature change is small.

Given the above constraint, one can see the attraction of the AMR cycle. Acting as a regenerator as well as the means of work input, the AMR increases the temperature span of a device many times the adiabatic temperature change. Like any other cyclic refrigerator, a designer wants to maximize cooling for a given work input. A simple entropy balance on an AMR suggested that the magnetocaloric effect must scale with temperature according to the following relation [21]:

$$\Delta T_{ad}^{ideal}(T) = T\frac{\Delta T_{ref}}{T_{ref}}, \tag{1.5}$$

where ΔT_{ad}^{ideal} is the ideal MCE at temperature T, ΔT_{ref} is the MCE at the hot end of the AMR, and T_{ref} is the temperature of the AMR at the hot end in the low magnetic field. Equation (1.5) states the ideal magnetocaloric effect should be a linearly increasing function of temperature. If correct, this expression implies that if the magnetocaloric effect at the cold end of the AMR exceeds that at the hot end, the second law of thermodynamics will be defied. This constraint has led researchers to search for magnetic refrigerants that match this linear expression for MCE. With no single material able to do this over the large temperature spans required for hydrogen or natural gas liquefiers, Barclay proposed a multi-material layered AMR [37]. A hypothetical example of how a layered AMR may approximate the constraint of Equation (1.5) is shown in Figure 1.2. The solid straight line starting at the peak of the Gd MCE curve is Equation (1.5).

It would seem from Figure 1.2 that an AMR bed composed of the materials shown in the figure would perform better than a bed composed of Gd because the superimposed MCE profiles more closely match the ideal line; however, a number of questions arise. Questions such as, how much of each material should be used?, how many materials does one need?, will the AMR operate if an MCE peak exceeds the ideal scaling?, how are work and heat flows satisfied?, and, what is the temperature as a function of position in the bed?, to name only a few. Addressing some of these questions for single and multi-material AMRs has been the objective of many experimental and numerical studies [17-24, 38-45]. The relatively slow progress in answering some of these questions and developing better performing magnetic refrigerators can be attributed to the complexity of the problem on many different levels. Some of the difficulties associated with AMR research will be described.

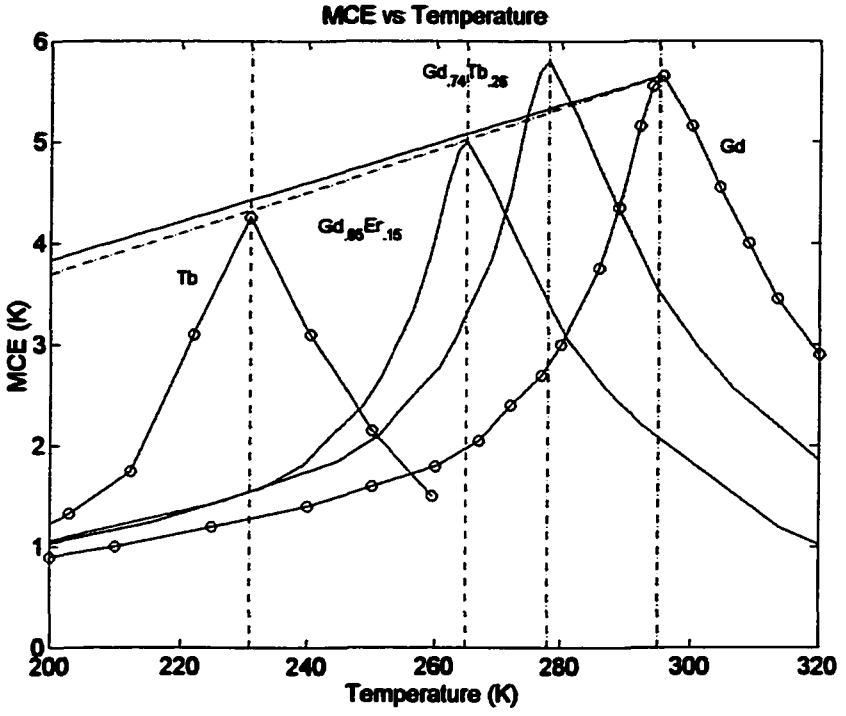

Figure 1.2 MCE curves for various materials with a field change of 0-2 T. (*o* represent experimental data points, lines are extrapolated data.)

1.3 Research Impediments

AMR Refrigerator (AMRR) development can be broken into three broad tasks: material synthesis, device engineering, and experiment and analysis. Material synthesis involves the search, characterization and fabrication of good AMR refrigerants. Device engineering requires the design and construction of the superconducting magnet sub-system (or permanent magnet array), fluid and heat transfer apparatus, vacuum housing, instrumentation, drive system, regenerator housing and many other items particular to cryogenics. Experiment and analysis require the collection of data, interpretation and application; analysis is typically numerical in nature due to the complex thermodynamic interactions in the AMR and non-linear properties associated with magnetocaloric materials. The difficulties encountered in magnetic refrigeration research are present among all three tasks.

1.3.1 Materials

As discussed earlier, substantial research is directed towards the development of better magnetocaloric materials, but the question as to what a "better" material is has still not been clearly answered. Two properties tend to be discussed in the literature: the adiabatic temperature

change and the isothermal entropy change. A large value for the latter does not necessarily imply that the former will also be significant. In a gas-cycle, the property of primary importance largely depends on the working cycle i.e. a Brayton cycle may be weighted more towards adiabatic temperature change than a Stirling cycle which would tend to want a large isothermal entropy change. A similar argument can be put forward regarding an AMR device; however, it is still not clear what the ideal AMR cycle should be. Furthermore, unlike regenerative gas cycles, in an AMR the working medium is also the regenerator. An efficient regenerator should have a large thermal capacity; thus, a large volumetric heat capacity is another important property for good AMR materials. Unfortunately, a large heat capacity means that the magnetic entropy change must also be large to produce a significant MCE.

Increased cycle frequency is a logical method of creating larger power densities. In this regard, the adiabatic temperature change should not display significant kinetic effects. A material that displays a large adiabatic temperature change but also has a time constant on the order of one quarter of the cycle frequency may perform worse as an AMR refrigerant than a material that has a smaller magnetocaloric effect but fast response time. Potter and Wood published a paper in 1985 that classified magnetocaloric materials based upon a parameter they called the refrigerant capacity [46]. As the authors state, the refrigerant capacity is applicable to cycles with isothermal heat transfer with constant temperature heat sinks. It can also be applied to cycles that use a regenerator to increase the temperature span. This parameter may only be applicable to isothermal heat transfer AMR cycles if at all. There has been some confusion in the literature because this parameter has been incorrectly adopted as a general measure of a good magnetocaloric material [47]. To try to classify a good magnetocaloric material without considering the thermodynamic cycle is of limited use.

A final concern is the material cost. It has been found that the purity or precursor materials can impact material performance significantly [48]. Unfortunately, high purity materials can be costly as is processing refrigerants into suitable geometries for good regenerators.

1.3.2 Device Engineering

There have been a number of different AMR refrigerators built previously, and the different geometries can be classified as one of the following: reciprocating, rotary or pulsed field. Each geometry has advantages over others. Some of the difficulties associated with AMRR design and construction are:

a. large magnetic forces (scale with field strength, gradient and regenerator volume,)

b. operating frequency (one wants this to be high to minimize material requirements and magnet size, and to maximize power density,)

c. sealing (leaks by-passing the regenerator beds can negate any useful cooling power); and,

d. regenerator design. A good passive regenerator requires a balance between fluid pressure drop, longitudinal conduction and heat transfer; an AMR is subject to these constraints, but must also satisfy entropy and energy balances particular to the AMR cycle. A vast literature exists dealing with the optimization of passive regenerators.

Another issue of practical concern for AMR devices is the volume of magnetic material used. This is an important parameter because it directly affects the size of the magnet system and the intensity of magnetic forces. The former is of concern because the cost of the magnet subsystem can be a large fraction of the total capital cost. The latter item makes the engineering problem more difficult in terms of structural and drive components, and, peculiar to magnetic devices, the regenerator itself. It is important to design the regenerator housing so that parasitic heat leaks are minimized, but this constraint is made more difficult because the magnetic refrigerant is subject to a body force. Each grain of the bed (assuming particles) contributes to the total magnetic force, which can be substantial (this problem exists even with force-balanced geometries such as rotary devices.)

Finally, past efforts to develop AMRRs (i.e. refrigerators) have tended to emphasize cooling power. Without using a high operating frequency, the way to increase cooling power is with higher magnetic field strengths and larger amounts of refrigerant. Increasing these parameters tends to make the design problem more difficult and expensive due to the reasons given above.

1.3.3 Experiment and Analysis

Unlike refrigerators that use a gas as the working substance, materials that appear to be useful as magnetic refrigerants display non-linear properties that are not well predicted by contemporary theory and models. This problem is further exacerbated because: (a) even materials displaying similar magnetic order transitions can have large differences in thermodynamic properties; and, (b) the temperature where refrigerant materials tend to be most effective is around the phase transition region.

Modeling of passive regenerator beds using more than one magnetic material is an area of intense research and tends to be numerically intensive while having varying degrees of success predicting actual performance. Attempts at numerically attacking a similar problem that includes

magnetic work interactions face an even more daunting task. One of the problems limiting modeling success is the lack of a sufficiently accurate general constitutive equation describing magnetocaloric materials. Qualitative behaviour can be modeled using Mean Field Theory; however, accurate property relations must still be experimentally determined for each material. Most AMR models that have been developed still face the litmus test of experimental corroboration. No known model has been rigorously validated with experimental data.

1.4 Problem Description

While the AMR refrigerator is, in principle, a simple concept, it has proven to be difficult to apply. Realizing a commercially viable device has yet to occur. The AMR concept using a single material has been proven and the process can be extremely efficient over limited temperature spans. Experimental and numerical studies have shown this [34, 41, 39]. Without a single material that can span the 77 – 20 K range or room temperature to 110 K, staged devices or multi-material AMRs must be used to liquefy hydrogen or natural gas. A proof of the layered AMR structure has yet to be demonstrated although there is one reported attempt in the literature [24]. Proof of this principle is an important step in advancing the status of regenerative magnetic liquefiers.

1.4.1 AMR Operating Regimes

Using Figure 1.2 as a reference, one can imagine a layered AMR consisting of three or more materials. For this type of bed, materials inside the AMR (as well as the material at the cold end) may operate around their transition temperatures. In addition to this condition, two other general operating points can be identified for a single ferromagnetic material:

a. $T_{Curie} > T$,

b. $T_H > T_{Curie} > T_C$ and,

c. $T > T_{Curie}$.

T_H is the temperature of the refrigerant material at the hot end of a material in the low field, T_C is the temperature of the refrigerant at the cold end in the low field, T_{Curie} is the material Curie temperature, and T is the temperature at different locations in the refrigerant. Condition *a* says that the temperature at all points in the material is less than the Curie point – this is a common operating condition for most devices with single material AMRs. Condition *b* can also be considered a single material operating condition, or, more likely, an operating condition for a

material inside a layered AMR. In this state, the material is operating 'around' the transition temperature so that the cold end is below the Curie point and the hot end is above. Finally, condition *c* represents a material operating above its Curie temperature. This condition is of interest since, in a transient state, during start-up for example when the working temperature span has not yet been established, a material will have to progress through this condition to reach steady-state.

Given the constraint imposed by Equation (1.5), it would appear that condition *c* can not occur while simultaneously producing cooling. In this state, the MCE at the cold side of the material will be greater than the MCE at the hot end. This condition is important if transient behaviour is to be understood. State *b* is hypothesized to be the condition for some or all materials in a multi-material AMR and, therefore, is also important to understand. However, there have been few studies addressing these two conditions in detail. Matsumoto *et al.* gave steady-state solutions for a single material AMR operating in condition *b*, but no transient details are given. Some simple steady-state model predictions for two-material AMRs are given in [20] and [49]. The only other studies pertaining to these conditions are discussed below.

Two previous studies [20, 24] by Green *et al.* at the David Taylor Research Center are of particular interest to the work reported in this thesis. Together, these two studies provide experimental results concerning the development of a pulsed field AMR apparatus. In the first paper, test data using a Gd AMR are described. Experimental conditions are given including the temperature span developed. In the second study, the same apparatus is used to test an AMR composed of Gd and Tb. Instead of having two discrete layers, this AMR was divided into three equal sections. The first was made of Gd, the last was Tb, and the center was made up of equal amounts of Gd and Tb mixed together. For similar operating conditions, the Gd AMR developed a 50 K temperature span whereas the Gd-Tb AMR only managed 24 K.

These results were a surprise to the authors since their model results predicted an increased temperature span using more than one material. The authors could not give a clear explanation for the poor performance of the second AMR, but speculated that the mismatch between the ideal MCE and the real MCE as well as the variation in heat capacity above the Curie point for Tb were problems.

1.4.2 Magnetic Material Properties

Large variability in the properties of magnetocaloric materials makes it difficult to make broad based conclusions concerning AMR performance characteristics. In this thesis, "first-order"

magnetic materials are those that show a discontinuous change in entropy versus temperature; "second-order" materials have a gradual, continuous change in entropy due to magnetic ordering. The emergence of first-order materials as possible magnetic refrigerants has complicated AMR design due to their discontinuous change in entropy and the associated difficulty in applying standard thermodynamic relations. Second-order materials currently make the most practical refrigerants; furthermore, mean field theory provides reasonable predictions for these materials. For these reasons, the work in this thesis is focused on second-order materials only. To further simplify the numerical work, a prototype second-order material is used to represent the properties of all materials. To differentiate amongst various specific refrigerants, properties are scaled using the transition temperature and the peak heat capacity in zero field. This is discussed in more detail later.

Gadolinium is a second-order material displaying a good magnetocaloric effect and has been well studied. With the application of a 5 T magnetic field, the adiabatic temperature change is approximately 10 K near the ordering temperature. Furthermore, tests on single crystal Gd have been unable to detect any hysteresis at all temperatures [36]. This is an important property since the reversibility of the magnetocaloric effect is one of the important characteristics that makes magnetic refrigeration an attractive alternative to conventional cycles.

The spontaneous magnetic ordering process in gadolinium is known to be a paramagnetic to ferromagnetic process. In this regard, gadolinium is an anomaly compared to the other rare earth elements that tend to order antiferromagnetically with no applied field. When a magnetic field is applied below the transition temperature these materials tend to display a more complex helical antiferromagnetic to ferromagnetic phase transition [50]. However, in spite of this difference, many of the rare earth elements are qualitatively similar to gadolinium as to their variation in MCE and heat capacity as a function of temperature and field.

For the reasons mentioned above and because it has been studied in detail, gadolinium can be considered to be a prototype material for AMRs and one that can be used as a benchmark for comparison to other materials. In this study, the properties of gadolinium are assumed those that define a good magnetocaloric material undergoing a second-order para-ferromagnetic phase transition. The relative MCE and heat capacity as a function of reduced temperature are assumed to represent other second order refrigerants with ordering temperatures above 200 K.

1.5 Objective

Performance improvements using a layered AMR have not been demonstrated. An attempt to do this failed, and there have been no further reports of research addressing the failure. There are few studies examining the impacts of refrigerant properties and operating conditions on multi-material AMRs. Some materials research has neglected the AMR cycle in the search for better materials and, in doing so, has created some confusion. Studies addressing the complete range of operating conditions for second order magnetic materials are limited. As a result, there is still an incomplete understanding of what an "ideal" material should be. For these reasons an analysis of the problems from an engineering perspective is warranted. In particular, a study of conditions *b* (operation around the transition temperature) and *c* (above the Curie temperature) is needed if multi-material AMRs are to be developed. To do this, the logical progression is to begin with a single material and to increase the number of materials gradually as our understanding of AMR behaviour is enhanced.

This thesis addresses these problems as follows:

a. a simplified thermodynamic analysis of an AMR is performed. Expressions for entropy production are derived. These results are used to determine the characteristics of "ideal" magnetocaloric materials,

b. a novel apparatus to test Active Magnetic Regenerators from room temperature to 20 K is designed, fabricated and tested. This work includes the design of a conduction-cooled superconducting magnet sub-system, as well as a dynamic test apparatus that uses smaller amounts of material and operates at frequencies higher than previous devices,

c. a numerical model is developed reflecting the operation of the test apparatus. The model provides transient information for AMR operation. The performance of single material and a two material layered AMRs is simulated, and,

d. experiments using Gd AMRs are performed examining conditions *b* and *c*. Experimental results are used to validate the numerical model.

Previous works have shown the potential of AMR liquefiers, and the movement towards a hydrogen economy now provides a powerful service demand for AMR technology. The engineering challenge to produce AMR devices is multi-disciplinary problem requiring sustained work. Recent work suggests that this technology may soon be commercially viable.

Chapter 2
Thermodynamics of AMRs

The purpose of this chapter is to analyze ideal AMR behavior. A cycle capturing the essence of an AMR is described and an expression for entropy generation in the AMR is derived. Zero entropy generation is used to determine an analytic expression for the ideal MCE as a function of temperature. The implications of the ideal MCE function on material heat capacity are discussed.

2.1 AMR Cycle

The system under consideration is shown schematically in Figure 2.1. The envelope of an AMR bed is shown with a dashed line while a section of differential thickness is highlighted. The bed is made up of a porous solid material that is the magnetic refrigerant, and a fluid within the pores acts as the heat transfer medium. The fluid transfers heat between a cold heat exchanger, the refrigerant, and a hot heat exchanger. The mass flow rates of the fluid are shown as $\dot{\varphi}$. Over a complete cycle, heat is absorbed in the cold heat exchanger and rejected in the hot heat exchanger. The AMR should be recognized as the combined solid-fluid system.

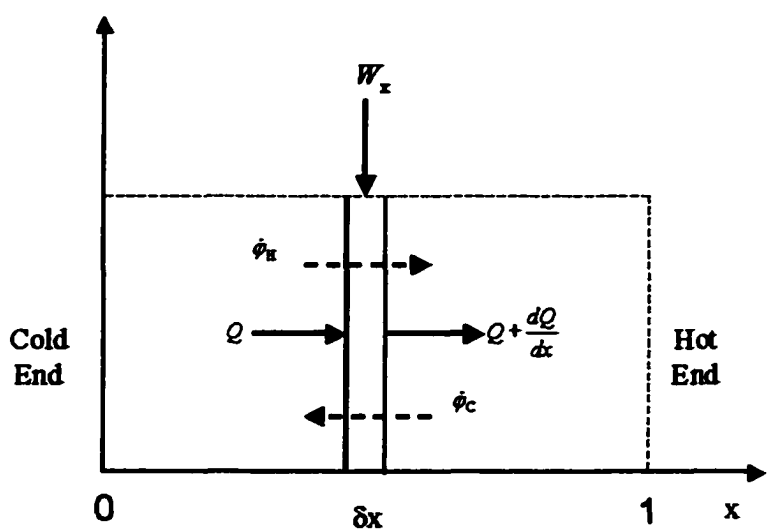

Figure 2.1 A schematic representation of an AMR showing the net work and heat flux at a differential section.

Most AMR devices built and tested to date have mimicked a reverse magnetic Brayton cycle in each section of the regenerator bed by using four distinct steps:

(1) while the AMR is in a low magnetic field the fluid is blown from the hot side to the cold side of the bed, thereby warming the refrigerant,

(2) the AMR is exposed to a high magnetic field in an adiabatic process, thereby causing a temperature rise at each section of the bed equal to the MCE at the local temperature,

(3) heat transfer fluid is blown through the bed from the cold side to the hot side causing a small constant-field temperature change in each section; and,

(4) the bed is isentropically removed from the magnetic field thus reducing the temperature of each section by the local MCE. In the analysis that follows, the adiabatic steps are assumed to occur instantaneously while the hot and cold blows occur over some time, τ_B.

Figure 2.2 shows the assumed refrigerant cycle occurring in the differential section at some location in the AMR. The cycle as described above is equivalent to the process starting at point '*a*' and proceeding alphabetically to return to the starting point. The refrigerant temperature change in the low isofield process, δT_C, is due to regeneration occurring during the cold blow, $\dot{\varphi}_C$.

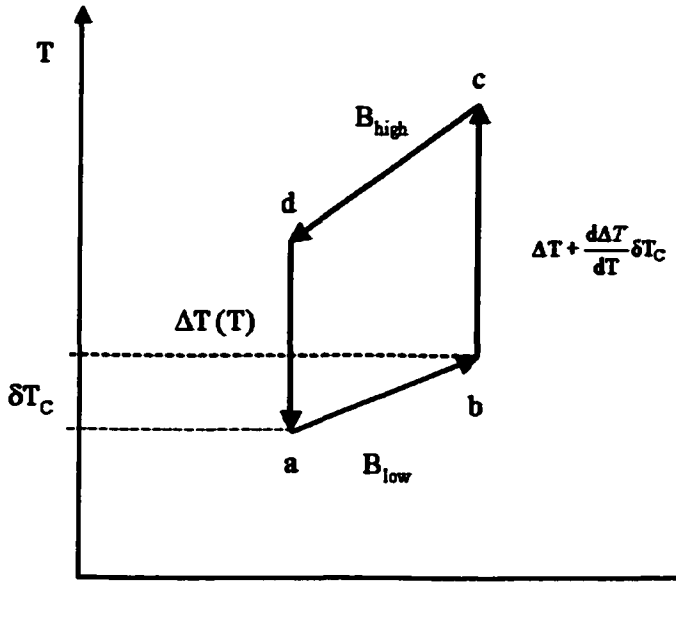

Figure 2.2 The hypothetical cycle for the magnetic refrigerant at some cross-section of the AMR.

It is assumed that the magnitude of the MCE for the process *b-c* is described by a first order Taylor series approximation in reference to point *a*. In the reversible case, the resulting area

within the *T-s* diagram is equivalent to the magnetic work input per unit mass for a complete cycle.

2.2 Utilization

A parameter that will be shown to be of significance when determining the performance of an AMR is the utilization, Φ. This parameter will be used throughout this thesis; therefore, the definition of utilization and its physical meaning will be described here.

In the context of this thesis, utilization is defined as,

$$\Phi(T,B) \equiv \frac{m_f c_p}{M_b c_B(T,B)}. \tag{2.1}$$

m_f is the total mass of fluid displaced during a blow phase, c_p is the fluid heat capacity, M_b is the mass of refrigerant in the AMR, and c_B is the refrigerant heat capacity. Of the properties that define utilization, only the refrigerant heat capacity needs to be considered a function of temperature, T, and field strength, B. The utilization is the ratio of fluid thermal capacity to refrigerant thermal capacity.

When solving the differential equations describing the AMR, a parameter of the following form appears,

$$\dot{\Phi}' \equiv \frac{\dot{m}_f c_p}{(1-\alpha) A \rho_s c_B} \tag{2.2}$$

where α is the bed porosity, A is the cross-sectional area of the AMR, and ρ_s is the density of the refrigerant. This is the ratio of the instantaneous thermal flux rate to the refrigerant thermal mass per unit length. If the mass flow rate is constant over the time of a blow, τ_B, and the blow is sufficiently small so that the local refrigerant heat capacity can be considered constant then,

$$\Phi' \equiv \int_0^{\tau_B} \frac{\dot{m}_f c_p}{(1-\alpha) A \rho_s c_B} dt = \frac{\dot{m}_f c_p \tau_B}{(1-\alpha) A \rho_s c_B}. \tag{2.3}$$

Φ' is the local utilization, or utilization per unit length.

It will be convenient to define a reference value for the utilization to generalize both experimental and numerical results. Because the hot heat sink temperature and cold temperature are independent of AMR refrigerant, they are not useful for specifying a reference heat capacity

value. Instead, the peak heat capacity of the refrigerant in zero field will be used. This peak occurs near the transition temperature,

$$c_{B,peak} = c_B(T \cong T_{Curie}, B = 0), \tag{2.4}$$

thus,

$$\Phi_{ref} \equiv \frac{m_f c_p}{M_b c_{B,peak}}. \tag{2.5}$$

In terms of passive regenerators, Φ is sometimes referred to as the matrix capacity rate ratio and varies little throughout the regenerator for constant fluid heat capacity. For an AMR, the local utilization is a function of field and temperature and, in general, is position dependent.

2.3 Entropy Generation

Focusing on the heat transfer fluid, an expression for the entropy generation per unit length in the AMR will be derived. In the following derivation, the diffusion term is assumed negligible and the mass flow rates for each blow phase are assumed constant. The general equation describing entropy generation per unit length in the differential section δx is,

$$\frac{\partial S'}{\partial t} + \nabla \cdot \dot{S} = \dot{S}'_S + \dot{S}'_g. \tag{2.6}$$

S' is the entropy per unit length, $\dot{S}$ is the rate of entropy flux through the section, $\dot{S}'_S$ is an entropy source per unit length, and $\dot{S}'_g$ is the rate of entropy generation per unit length.

If a complete cycle for the AMR is considered when periodic steady-state operation has been achieved, the net entropy generation is found by integrating over a cycle,

$$S'_g = \oint \frac{\partial S'}{\partial t} dt + \oint \nabla \cdot \dot{S} dt - \oint \dot{S}'_S dt. \tag{2.7}$$

Using Figure 2.1 as a guide, an equation describing the local time-averaged entropy generation for the fluid can be derived. The entropy source is due to heat transfer between the solid and the fluid. For periodic steady-state and assuming the refrigerant undergoes a reversible cycle as shown in Figure 2.2, the last term in Equation (2.7) is zero. Furthermore, since the first term on the right-hand side is zero for periodic steady-state the entropy generation relation becomes,

$$S'_g = \oint \nabla \cdot \dot{S} dt. \tag{2.8}$$

Assuming the mass flow rate is independent of space, Equation (2.8) can be written using the mass flow rate and mass specific entropy explicitly in one dimension,

$$S_g' = \oint \dot{m} \frac{ds}{dx} dt. \tag{2.9}$$

For an ideal gas with negligible pressure drop, the mass specific entropy is related to heat capacity by,

$$\begin{aligned} dh &= Tds + vdp, \\ c_p dT &= Tds. \end{aligned} \tag{2.10}$$

Thus, the local entropy generation becomes,

$$S_g' = \oint \frac{\dot{m} c_p}{T} \frac{dT}{dx} dt. \tag{2.11}$$

If the thermal mass of fluid is small, it can be assumed that the local temperature gradient remains constant over the duration of a blow and the temperature change of the material is small. The cycle integral can then be easily evaluated for the hypothetical process consisting of two adiabatic steps and two isofield blows by noting that the mass flux is zero in the two adiabatic steps;

$$S_g' = \frac{(\dot{m} c_p \tau_B)_H}{T + \Delta T} \frac{dT}{dx}_H - \frac{(\dot{m} c_p \tau_B)_C}{T} \frac{dT}{dx}. \tag{2.12}$$

Finally, using the relations,

$$\begin{aligned} T_H &= T + \Delta T \\ \frac{dT}{dx}_H &= \frac{dT}{dx} + \frac{d\Delta T}{dx} \\ \frac{dT}{dx}_H &= \left(1 + \frac{d\Delta T}{dT}\right) \frac{dT}{dx}, \end{aligned} \tag{2.13}$$

the entropy generation per unit length is,

$$S_g' = \left[\frac{(\dot{m} c_p \tau_B)_H}{T + \Delta T} \left(1 + \frac{d\Delta T}{dT}\right) - \frac{(\dot{m} c_p \tau_B)_C}{T} \right] \frac{dT}{dx}. \tag{2.14}$$

Equation (2.14) can be written using the following definitions,

$$\begin{aligned} \varphi_C &\equiv (\dot{m} c_p \tau_B)_C, \\ \varphi_H &\equiv (\dot{m} c_p \tau_B)_H, \end{aligned} \tag{2.15}$$

$$S_g' = \left[\frac{\varphi_H}{T+\Delta T}\left(1+\frac{d\Delta T}{dT}\right)-\frac{\varphi_C}{T}\right]\frac{dT}{dx}. \tag{2.16}$$

The parameters φ are seen to be the total fluid thermal capacity over the cold and hot blows. If these fluxes are equal, the AMR is said to be operating in a balanced condition; however, in general, this need not be true. A balance parameter can be defined as,

$$\beta \equiv \frac{\varphi_C}{\varphi_H}. \tag{2.17}$$

We know from the second law that entropy generation is a positive quantity. Therefore, the following must be satisfied,

$$\left[\frac{\varphi_H}{T+\Delta T}\left(1+\frac{d\Delta T}{dT}\right)-\frac{\varphi_C}{T}\right]\frac{dT}{dx}>0. \tag{2.18}$$

If we assume that

$$\frac{dT}{dx}>0 \tag{2.19}$$

at all locations in the AMR then the following inequality must be true for small perturbation,

$$\left(1+\frac{d\Delta T}{dT}\right)>\frac{\varphi_C}{\varphi_H}\left(1+\frac{\Delta T}{T}\right). \tag{2.20}$$

2.3.1 Ideal MCE

A fundamental question that has been studied since the idea of the AMR was developed is what should the MCE as a function of temperature be to maximize cooling capacity over a desired temperature span. An early analysis by Cross *et al.* [21] specified that to satisfy the second law, the ideal MCE should vary linearly with temperature throughout the bed according to,

$$\Delta T^{ideal}(T)=\frac{\Delta T(T_{ref})}{T_{ref}}T, \tag{2.21}$$

where ΔT is the MCE at a temperature T, and the subscript *ref* is a reference point which could be the Curie point. Equation (2.21) is derived assuming the net entropy flows entering and leaving the AMR are equal and determined by the adiabatic temperature change of the material at the end temperatures.

Further analysis of the problem was performed by Hall *et al.* [43] and determined that the ideal MCE need only satisfy Equation (2.21) at the ends of the AMR and not throughout the bed. They also suggested that no unique ideal MCE exists for an AMR, however the material should satisfy the constraint,

$$\frac{d\Delta T}{dT} \geq -1. \tag{2.22}$$

A recent study [51] reports that the ideal MCE profile is a function of AMR operating conditions and is given by,

$$\Delta T^{ideal}(T) = f(B)T^{m_{fC}/m_{fH}} - T, \tag{2.23}$$

where $f(B)$ is a function of magnetic field strength B, m_f is the fluid mass flow rate for the hot, $_H$, and cold blows, $_C$, and T is the temperature of the bed at the cold end. The details of this derivation are not published.

The purpose of this section is to derive an analytic expression for the ideal MCE as a function of temperature. If the "ideal" AMR is defined as one with zero entropy generation, then, using Equation (2.16), the following relation is true,

$$\frac{\varphi_H}{T+\Delta T}\left(1+\frac{d\Delta T}{dT}\right)-\frac{\varphi_C}{T}=0. \tag{2.24}$$

The above can be rewritten in the form of a differential equation,

$$\frac{d\Delta T^{ideal}}{dT} - \frac{\varphi_C}{\varphi_H}\frac{\Delta T^{ideal}}{T} = \frac{\varphi_C}{\varphi_H} - 1. \tag{2.25}$$

Equation (2.25) is an ordinary first-order differential equation for the ideal MCE as a function of temperature and can be solved using the boundary condition $\Delta T(T_{ref}) = \Delta T_{ref}$,

$$\Delta T^{ideal}(T) = (\Delta T_{ref} + T_{ref})\left(\frac{T}{T_{ref}}\right)^{\beta} - T, \tag{2.26}$$

where the balance parameter has been used. As can be seen, Equation (2.26) is similar in form to Equation (2.23), and, if the AMR is balanced (β=1), the resulting expression is the same as Equation (2.21). Thus, Equation (2.21) is a particular case of the more general expression, Equation (2.26). Figure 2.3 shows some ideal MCE curves for various conditions of balance. The reference conditions are for Gd with a field change of 0 to 2 T shown as the dashed curve.

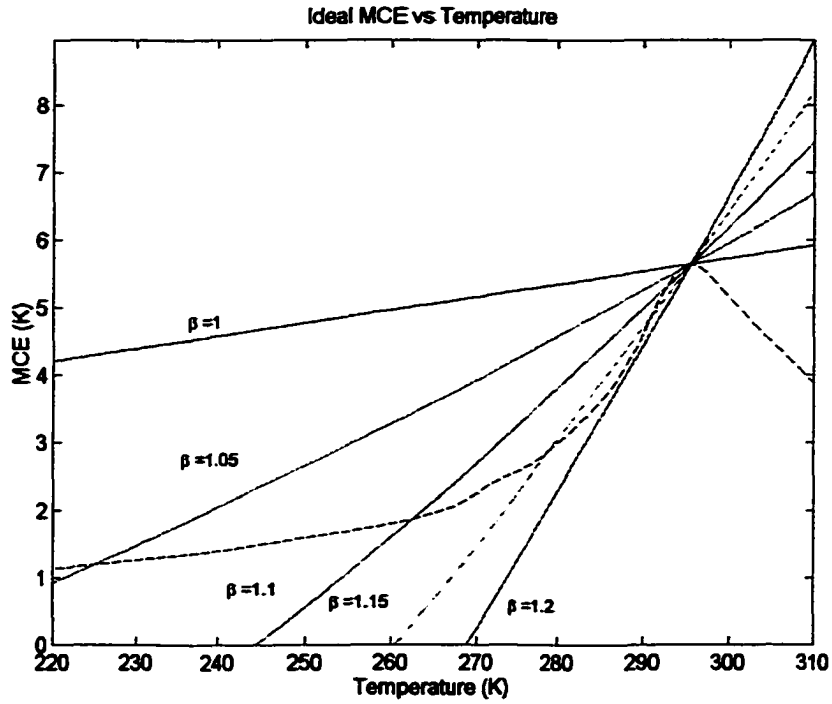

Figure 2.3 Ideal MCE curves for various conditions of balance. The reference condition is for Gd with a field change of 0 to 2 Tesla (dashed line).

2.4 Refrigerant Cycle

In the above analysis, the entropy generation was derived by an entropy balance focusing on the heat transfer fluid. The assumed cycle for the solid, shown in Figure 2.2, is reversible; thus, if there is entropy generation it is assumed external to the refrigerant. Using the short blow assumption, a simple entropy balance on the refrigerant is easily derived. The temperature change of the refrigerant during the cold blow is δT_C. The temperature change during the hot blow can be found using the Taylor series expansion and subtracting the temperature at c from d,

$$\delta T_H = \left(T + \delta T_C + \Delta T + \frac{d\Delta T}{dT}\delta T_C \right) - (T + \Delta T). \tag{2.27}$$

Further manipulation gives the following,

$$\frac{\delta T_H}{\delta T_C} = 1 + \frac{d\Delta T}{dT}. \tag{2.28}$$

Now, because the refrigerant cycle is reversible, the entropy change during the hot blow equals the entropy change during the cold blow. The entropy change can be approximated by,

$$ds = \frac{c_B \delta T}{T}, \tag{2.29}$$

so, equating hot to cold gives,

$$\frac{\delta T_H}{\delta T_C} = \frac{T_H}{T}\frac{c_{BC}}{c_{BH}} = \frac{T+\Delta T}{T}\frac{c_{BC}}{c_{BH}}. \tag{2.30}$$

The isentropic ratio of the low-field heat capacity to the high-field heat capacity is defined as the refrigerant symmetry, σ,

$$\sigma \equiv \frac{c_{BC}}{c_{BH}} = \frac{c_B(T, B_L)}{c_B(T+\Delta T, B_H)}, \tag{2.31}$$

where B_L is the low-field strength, and B_H is the strength of the high-field.

Using the definition of symmetry, the equivalence of Equation (2.28) and Equation (2.30) results in the following differential equation,

$$\frac{d\Delta T}{dT} - \sigma\frac{\Delta T}{T} - (\sigma - 1) = 0. \tag{2.32}$$

2.5 "Ideal" Material Properties

There are some interesting implications of the basic thermodynamic analysis. Two key differential equations were derived, one for zero entropy generation for the fluid and the other for the refrigerant:

Fluid Ideal MCE:
$$\frac{d\Delta T}{dT} - \beta\frac{\Delta T}{T} = \beta - 1 \tag{2.33}$$

Solid Ideal MCE:
$$\frac{d\Delta T}{dT} - \sigma\frac{\Delta T}{T} = \sigma - 1. \tag{2.34}$$

If both equations are to be satisfied and entropy generation is to remain zero, then the solid and fluid temperatures must be equal at all locations and the following must be true,

$$\sigma = \beta. \tag{2.35}$$

Thus, for an ideal AMR, the condition of balance must match the refrigerant symmetry. Because the ideal MCE as a function of temperature is determined by the balance, intuitively, there must be a relationship between balance and symmetry since heat capacity and MCE are derived from the entropy curves. In practice, balance is generally constant throughout the AMR (i.e. the fluid

thermal flux at all locations is the same during a blow); therefore, the refrigerant symmetry must be independent of position. For a position independent field change in the AMR, the symmetry must be independent of temperature to satisfy the constraint of Equation (2.35). Carpetis [41] qualitatively discussed this inherent cycle irreversibility in an AMR due to non-deal entropy curves of the refrigerant. However, this is the first time the required entropy functions have been quantified and linked to AMR balance.

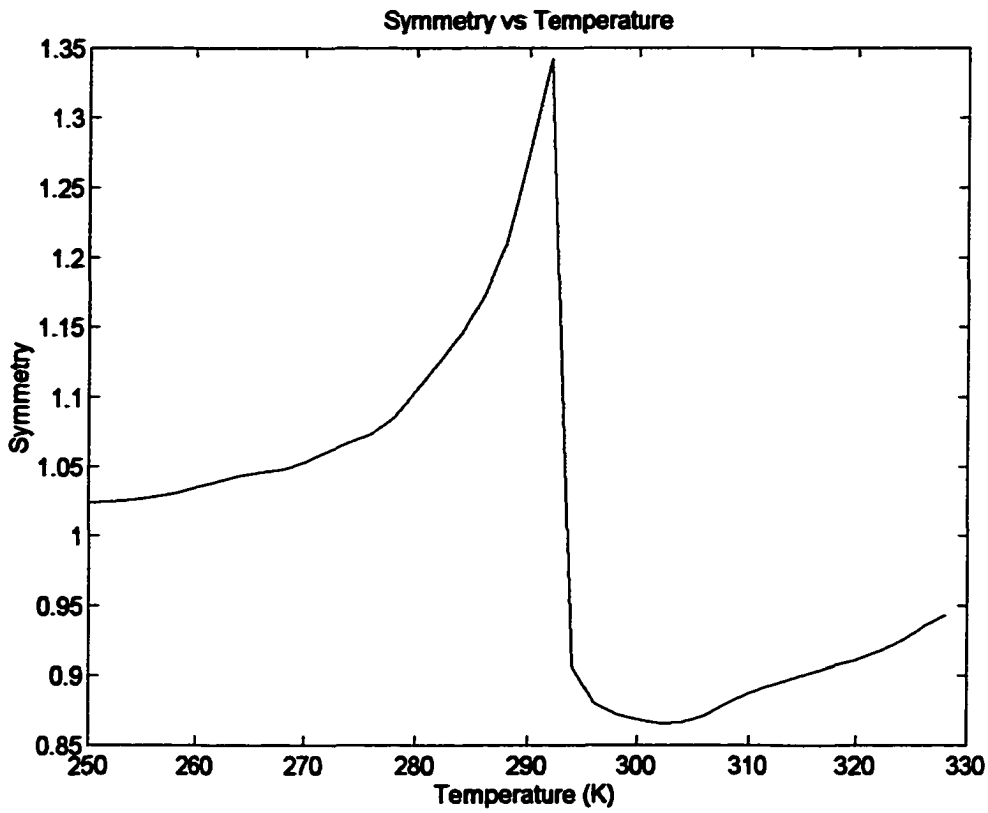

Figure 2.4 Symmetry of Gd for a 0 to 2 T field change.

Figure 2.4 shows the symmetry of Gd for a 0 to 2 Tesla field change using the data of [36]. Near the phase transition temperature, the refrigerant symmetry is a strong non-linear function of temperature. Thus, for an AMR with constant β the constraint of Equation (2.35) will not be satisfied over any significant temperature span. Moreover, even if the AMR has zero longitudinal conduction, the heat transfer coefficient is infinite, and the fluid has zero viscosity the simple assumed cycle does not satisfy a local solid-fluid entropy balance. This suggests that the isofield-

adiabatic cycle shown in Figure 2.2 cannot satisfy an entropy balance with known refrigerants and the real AMR cycle must be different.

The properties of an ideal refrigerant can be specified. The functional relationship between the low and high field entropy curves for an ideal material is defined using Equations (2.26), (2.35) and the definition of heat capacity,

$$c_B \equiv T\left(\frac{\partial s}{\partial T}\right)_B . \tag{2.36}$$

An expression of the following form results,

$$\frac{\left(\frac{\partial s}{\partial T}\right)_L}{\left(\frac{\partial s}{\partial T}\right)_H} = \beta\left(\frac{\Delta T_{ref} + T_{ref}}{T}\right)\left(\frac{T}{T_{ref}}\right)^{\beta} \tag{2.37}$$

where H and L signify the derivatives at the high and low fields respectively on an isentrope. Thus, as previously reported for a balanced AMR [21], the entropy curves are diverging for all conditions of balance greater than one.

Chapter 3
Field Generator

This chapter describes the design, fabrication, and operation of an apparatus to generate magnetic fields in a 20 cm room temperature bore. This was the first step in the development of the AMR Test Apparatus. The field generator consists of an 84 cm x 54 cm high cylindrical chamber designed around a converted immersion-cooled solenoid. The magnet spool is wound with NbTi superconductor and is conduction-cooled by a single two-stage Gifford-McMahon cryocooler with 1 W of cooling power at 4.2 K. The design operating current is 362 Amps for a 5 T field. A detailed description of the Field Generator follows.

3.1 Magnetic Field Generator

A Magnetic Refrigerator consists of a number of systems, one of which is the magnet sub-system. Until recently, Magnetic Refrigerators have used superconducting magnets as the source of the magnetic field. The reasoning behind this has been that the magnetocaloric effect is proportional to field strength and is relatively small for fields less than 2 Tesla. Field strengths larger than 2 Tesla in useable volumes rely on the use of superconducting windings. Advances in permanent magnet strengths over the last 15 years have approached inductions on the order of 2 Tesla; however, making use of the generated field over a volume large enough to accommodate bulk quantities of magnetic refrigerant is still challenging. For cooling powers requiring large volumes of refrigerant, superconducting magnets are the only means of efficiently producing significant field strengths. If high frequency operation is possible, smaller volume AMRs may be used thereby making permanent magnets feasible for some conditions.

Magnet geometries can take on a variety of forms. The easiest to fabricate is a solenoid and this is reflected in the cost. Some other geometries are split-pairs, race-track windings for transverse fields, and Tokamaks. Many different field shapes and volumes can be created, but practical limitations such as winding stress, critical field and currents, and thermal requirements restrict the designer in choosing magnet geometry. The scale of a device will also impact the form of the magnet sub-system.

3.1.1 Conduction Cooling

The generation of high magnetic fields has traditionally been achieved with immersion-cooled superconducting magnets. In essence, immersion-cooling is achieved by submerging the

superconducing magnet in a bath of liquid cryogen such as helium. This type of apparatus is made up of a complex arrangement of vacuum housing, dewars, liquid nitrogen and liquid helium transfer lines, radiation shielding, structural supports and insulation to maintain the temperature of a magnet in the superconducting state with minimum boil-off. In the case of a typical immersion cooled solenoid made with NbTi wire, the transition temperature is near 9.5 K and the magnet is designed with the expectation that it will be operating in a liquid helium environment at approximately 4.2 K. With the development of commercially available High Temperature Superconducting (HTSC) leads and closed cycle cryocoolers that achieve substantial cooling powers at temperatures near 4 K, it is now possible to design superconducting magnet devices that are cooled conductively [53].

Conduction cooling is achieved by thermally linking the magnet to the cold finger of a cryocooler via a solid medium and no longer requires liquid cryogens or as much associated ancillary equipment. Magnet systems designed to be conduction-cooled have several features that are different from immersion-cooled magnets as described in the recent literature. However, there are few reports of immersion-cooled magnets that have been successfully conduction cooled. In this work an existing 5 T, immersion cooled NbTi solenoid is integrated into a conduction-cooled apparatus.

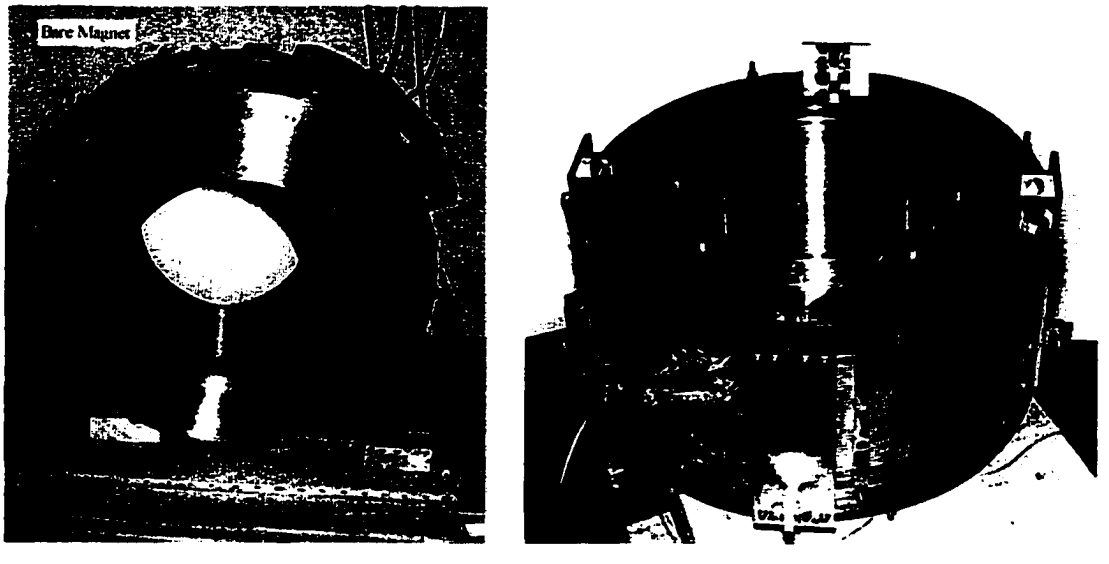

Figure 3.1 Recovered solenoid from immersion cooled apparatus (left). Solenoid with addition of OFHC copper conduction plates and clamping (right).

3.1.2 Apparatus Design

The magnetic field is generated by a 25 cm inner diameter pancake-wound superconducting solenoid designed and built by Darien Magnetics. This magnet was salvaged from a liquid helium cooled device whereby the immersion-cooled apparatus was disassembled and the solenoid removed. A picture of the bare solenoid is shown in Figure 3.1. The spool of the magnet is made of 304 SS and a layer of machined G-10 (glass-epoxy composite) separates the spool flanges from the windings. The G-10 is approximately 6 mm thick with radial grooves machined to allow for the circulation of liquid helium around the windings. The circumference of the winding is wrapped with aluminum wire that acts as a structural piece countering the magnetic pressure on the windings. Detailed specifications of the solenoid are listed in Table 3-1.

Table 3-1. Solenoid specifications.

Type	Pancake Wound Solenoid
Clear Bore	253 mm
Hmax/H(0,0)	1.43
Current at 5T	362.3 A
T/A	0.0138
I/Ic (B(0,0)=5T, 4.2K)	0.5
Inductance	5.5 H
Mass	136 kg
Superconductor	Nb-48%Ti
Total Winding Length	4570 m
Number of filaments	2000
Cu/SC ratio	1.8:1
Twist Pitch	1 per 50 mm
Cu matrix RRR	180

To convert to conduction cooling, the magnet is sandwiched between two 6 mm thick OFHC copper plates that act as thermal conductors. A thin layer of thermally conductive grease is spread between the spool flanges and the copper plates to ensure the contact area is as large as possible. Four aluminum clamps on the outer diameter of the spool hold the plates together. The plate centres are located with stainless steel rings bolted to the magnet spool. The magnet is positioned within the cold-box housing by eight G-10 suspenders. One end of the suspender attaches to the clamps on the magnet and the other end attaches to tabs on an aluminum plate termed the strongback. The strongback is connected to the first stage of a 1 W at 4.2 K GM Sumitomo cryocooler. A copper radiation shield is attached to the strongback and surrounds the inside and

outside of the magnet. A 6 mm thick OFHC (Oxygen Free, High Conductibity) copper busbar is bolted to the second stage of the cryocooler and is used as a thermal anchor point for leads and connections from the first stage. Figure 3.2 shows the major components of the field generator in position.

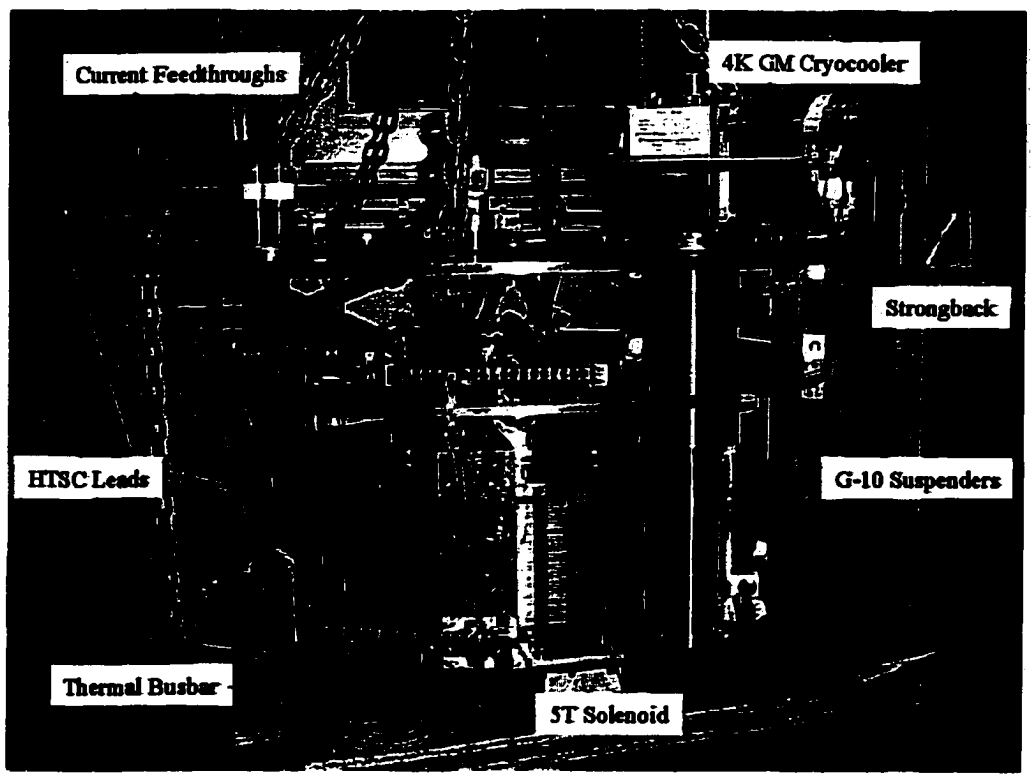

Figure 3.2 Partial magnet assembly showing the major components.

Conventional (copper) current leads optimized for minimum heat leak with a current of 250 Amps connect the room-temperature feedthroughs to the warm end of High Temperature Superconducting leads. The length of the copper current leads must be carefully chosen so that the heat leak to the first stage due to conduction and joule heating is minimized. The aspect ratio for the leads is optimized for a lower current rating than is needed for full field operation. This was done to facilitate testing, and because the initial application of the field generator was for a field of 2 Tesla. The electrical connections to the magnet are completed using two HTSC leads rated at 500 Amps purchased from American Superconductor. The HTSC leads conduct electricity from the ends of the conventional leads at the first stage to the busbar where the magnet leads are connected. Copper blocks thermally connect the joints to the structure.

Table 3-2. Calculated heat leaks to the first and second stages assuming a charging rate of 0.08 A/s.

Heat Source	First Stage	Second Stage
Conduction		
Suspenders	0.3 W	20 mW
Leads	18 W	130 mW
Radiation	2.5 W	300 mW
Steady-State Load	20.8 W	450 mW
Joule Heating	30 W	50 mW
Eddy Currents (structure only)	Negligible	280 mW
Transient Load	50.8 W	780 mW

The magnet is thermally linked to the second stage of the cryocooler via flexible ribbon connectors. The ribbon connectors are manufactured using flexible 0.4 mm thick OFHC copper foil. Ten layers of foil are soldered together creating a connection with a large cross-sectional area and minimum length. One connector attaches to each copper plate on the magnet. Indium foil is used between all thermal joints to ensure the contact area is as large as possible. The entire assembly is placed in a 304 SS vacuum chamber known as the cold box. Insulating blankets made with multilayers of aluminized mylar surround the magnet inside the radiation shield as well as outside the shield. Table 3-2 shows the calculated heat loads expected for steady-state operation, and while charging at a rate of 0.08 A/s.

When the magnet is operating, energy is stored in the magnetic field. The amount of energy, E, can be determined using,

$$E = \frac{1}{2} L I^2 \tag{3.1}$$

where L is the self inductance of the solenoid and I is the current. In the case of this particular solenoid, the stored energy at 5 Tesla is approximately 360 kJ. When the magnet transits uncontrollably from the superconducting state to the normal state it is said to quench. This can occur if there is a loss of cooling power or if there is power dissipation in the solenoid at a rate that is too fast for heat transfer to stabilize. All superconducting magnets are protected in some manner to ensure the windings are not damaged if a quench occurs. A common practice is to use diodes in parallel with the windings to clamp the maximum voltage generated when the field collapses. This practice is implemented here. The complete apparatus is shown in Figure 3.3.

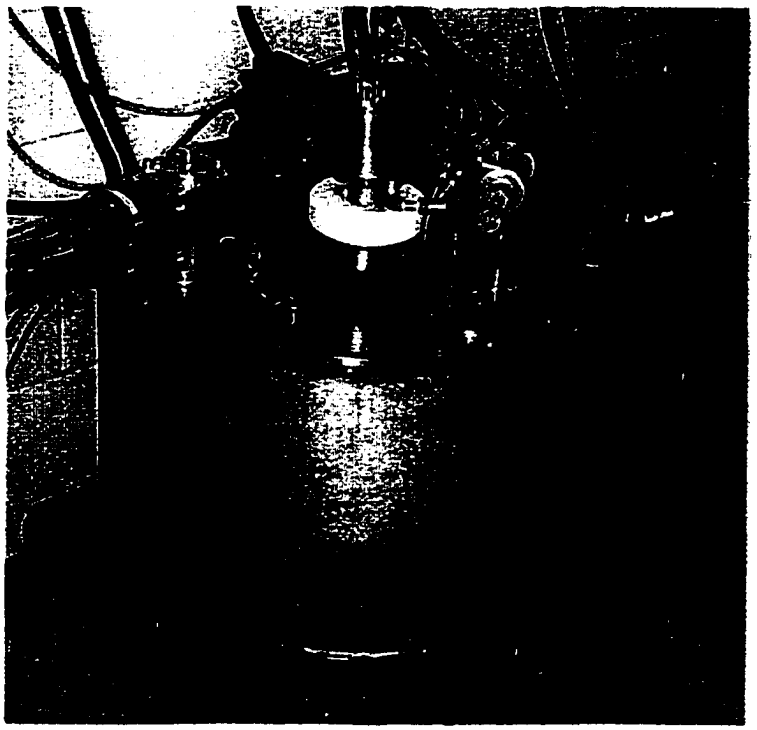

Figure 3.3 Completed Field Generator.

3.1.3 Testing

At the time of writing, the magnet has been tested and operated without a persistent current switch. A persistent current switch allows the magnet to be charged and then put into persistent mode by a switch creating a superconducting loop. The magnet power supply can then be turned off. Without a persistent current switch the heat load on the apparatus is much greater due to the Joule heating effects in the conventional current leads. The maximum operating current has been limited to 185 A (2.5 Tesla) due to the effects of stray field, and because the current leads are optimized for only 250 A. Further modifications should increase the realizable field strength.

The apparatus is cooled without the aid of a thermal accelerator as is used on some other conductively cooled devices. A thermal accelerator can be a heat pipe connecting the first and second stages. When the second stage reaches a predetermined temperature the fluid in the heat pipe solidifies thereby severing the thermal link and preventing an additional heat load from the first stage to the second stage. Prior to this temperature, the heat pipe efficiently transfers heat from the second stage to the first effectively increasing the cool-down time. The cool-down curve for the magnet is shown in Figure 3.4 and is typical of cooling curves presented by other authors for similar magnets. Initially, the temperature decrease of the magnet is approximately linear and

then begins to accelerate at about 75 K. Below 20 K the rate of temperature decrease is reduced. This may be explained in terms of changing thermal diffusivity and decreasing cooling capacity of the second stage.

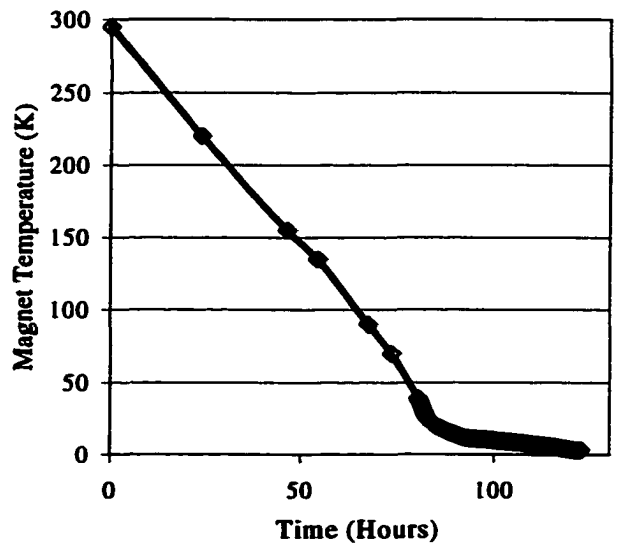

Figure 3.4 Magnet temperature during cool-down.

Figure 3.5 and 3.6 show the response of the magnet when charged to 20 A at 0.02 A/s. Figure 3.5 are the results when held at 20 A and allowed to reach steady-state, while Figure 3.6 shows the magnet temperature for a ramp up and down without a pause. The magnet temperature is measured by a Cernox™ RTD in one of the cooling channels in the G-10 end plates and is in contact with the end of the windings. Although the degree of thermal contact between the windings and the sensor is difficult to verify, test results suggest that while the sensor may not accurately indicate winding temperature it does give useful data reflecting winding thermal response. In all figures, the temperatures have been non-dimensionalized according to Equation (3.2) where T_{min} is 3.69 K and T_{max} is 6.2 K,

$$T^* \equiv \frac{T - T_{min}}{T_{max} - T_{min}}, \tag{3.2}$$

(3.69 K and 6.2 K correspond to the minimum and maximum magnet temperatures measured during the experiments.) The current has been non-dimensionalized by the peak current for each test (i.e. 20 A in Figure 3.5 and 3.6, 145 Amps in Figures 3.7 and 3.9.)

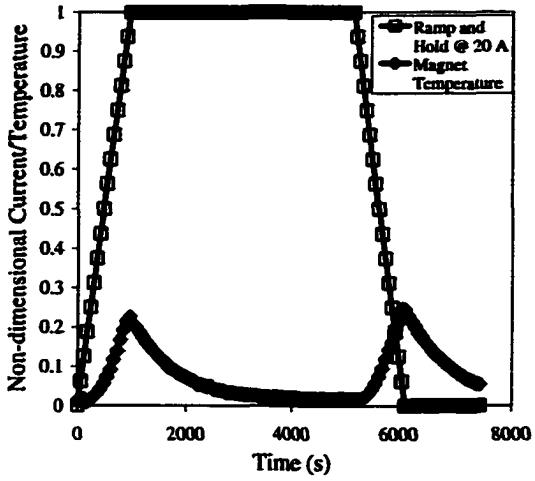

Figure 3.5 Magnet response when ramped to 20 Amps at 0.02 Amps/s and allowed to come to equilibrium.

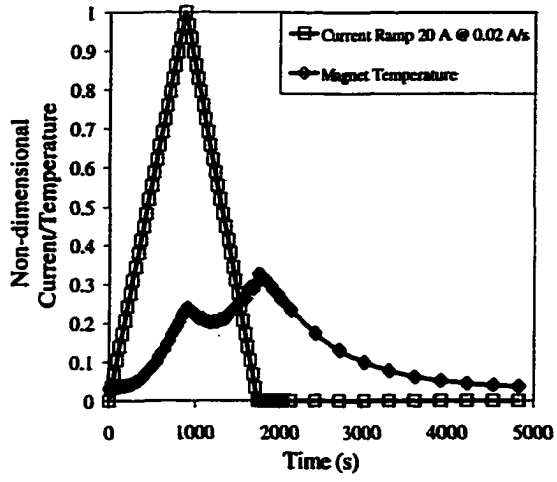

Figure 3.6 Magnet response when ramped up and down at 0.02 Amps/s to a peak of 20 Amps.

Figure 3.6 shows that although the joule heating effect decreases during the ramp down, there are first order effects significant enough to cause the magnet temperature to continue to rise even with a modest ramp rate of 0.02 A/s.

Figures 3.7 and 3.8 further highlight the effects of ramp duration (i.e. peak current) on time-varying losses and joule heating effects. These tests show the magnet and HTS cold-end temperatures for three cycles to 20 and 50 A respectively at 0.07 A/s. These figures clearly show the effect of ramp duration on hysteresis and eddy current heat generation. Once the cycling is complete, the magnet temperature decays slowly which is in accordance with what one would expect given the design of the solenoid (thermally isolated.) During testing it was noted that the copper plates on the magnet showed little change in temperature for currents less than 100 Amps, indicating that the windings of the magnet were well isolated thermally.

Charging characteristics for a ramp rate of 0.07 A/s and a peak current of 145 Amps (2 T) are shown in Figure 3.9 where the magnet was ramped up and down twice at a constant rate. The magnitude of joule heating has increased significantly. After 14 hours of operation at 145 A the magnet non-dimensional temperature decayed to 0.36 (4.59 K) while the HTSC steady-state temperature rose slightly to 0.59 (5.17 K). It is interesting to note in Figures 3.7 to 3.9 that while there is a large increase in magnet temperature when the peak current is changed from 20 to 50 Amps, the magnet temperature for two cycles to 145 A is only slightly higher than the ramps to 50 A.

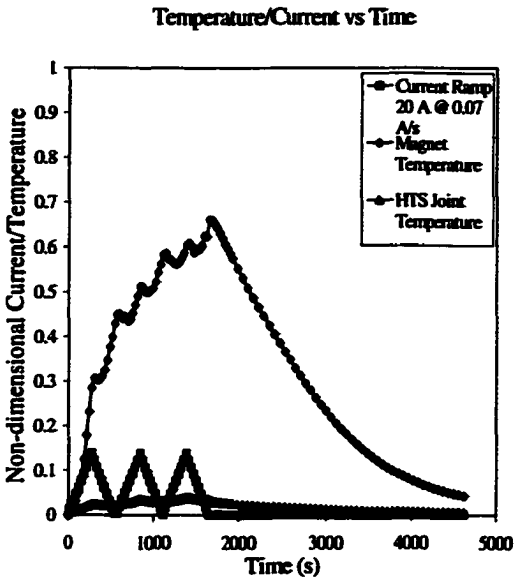

Figure 3.7 Magnet response to 3 cycles of ramping to 20 A at 0.07 A/s. (Current of 1 = 145 A.)

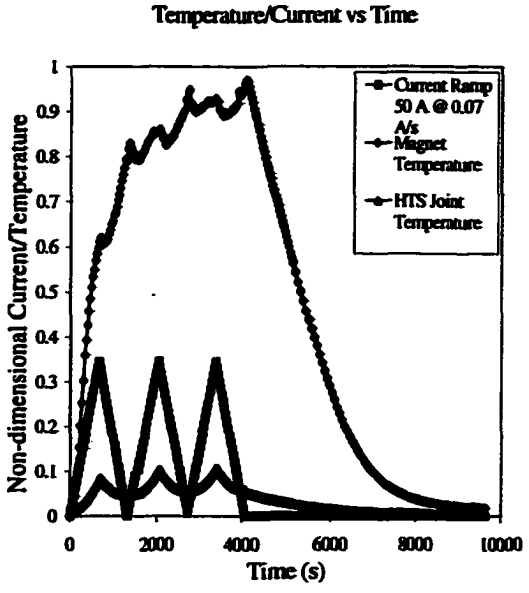

Figure 3.8 Magnet response to 3 cycles of ramping to 50 A at 0.07 A/s. (Current of 1 = 145 A.)

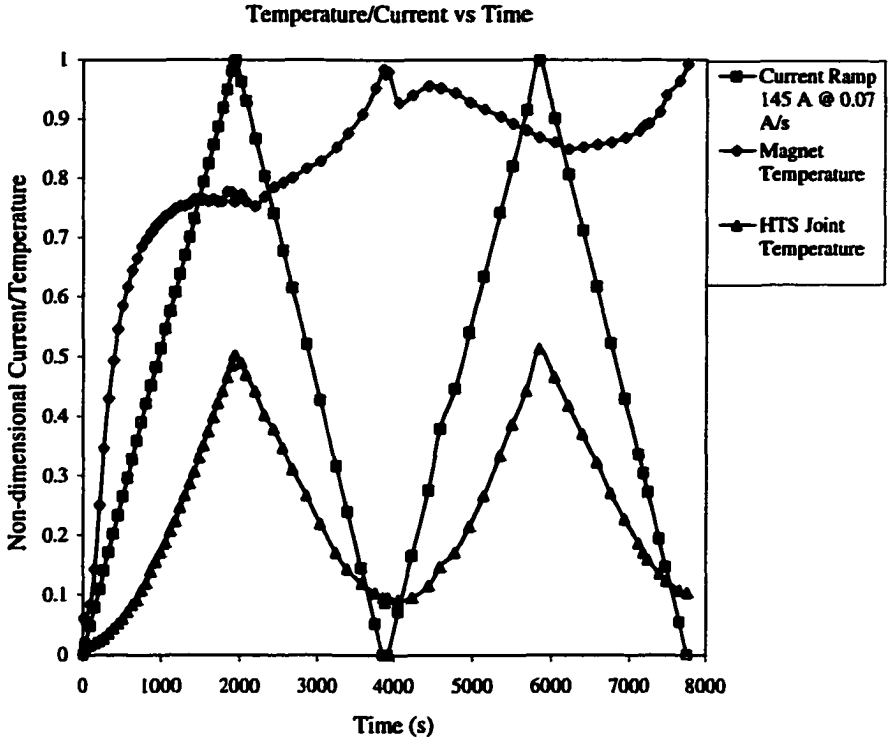

Figure 3.9 Temperature response ramping to 145 A twice at 0.07 A/s.

Although increasing temperature may enhance the rate of heat transfer, this reduced temperature rise is better explained by the rapidly increasing heat capacity of the magnet. For a typical epoxy impregnated NbTi winding, the volumetric enthalpy increases by nearly an order of magnitude when the temperature is increased from 4 to 6 K [54].

3.2 Summary

Testing of the field generator proved that the performance was sufficient for use in the AMR test apparatus. Higher field strengths would be preferable; however, time constraints required work to proceed with the rest of the apparatus design. With additional modifications, the full field of 5 Tesla may be attainable.

Test results indicate that the operating current is limited due to overheating at the joints between the normal leads and the High Temperature Superconducting leads. The temperature rise at the joint eventually causes the HTS leads to quench and the magnet to shutdown. The heat load at the joint is dominated by three mechanisms: conduction down the normal leads, joule heating in the leads, and joint resistance ohmic losses. The first mechanism is not significant. As described earlier, the leads are currently optimized for lower operating currents to keep the conduction loss low; thus, joule heating in the leads is the dominant lead loss. A new set of leads optimized for higher current will correct this problem. The additional loss due to the joint resistance can also be reduced by soldering the connections. Currently, the joint is a mechanical connection with indium foil in between to increase contact area.

An additional modification will help reduce temperature gradients at both first and second stages. In conduction cooling, the effective thermal conductivity is maximized by using large cross-sectional areas, short lengths, and high conductivity materials. By reducing the distance between the electrical connections and the first and second stages of the cryocooler, thermal gradients will be reduced. This is important at both stages. Although the HTS leads have a high transition temperature, this temperature is being exceeded. Once this problem is solved, the second stage critical temperatures must not be exceeded. The magnet windings and the connetions are NbTi wire with a critical temperature on the order of 9 K. For full field operation, the magnet windings are operating at 50% of the critical value, at a temperature of 4.2 K. Thus, the magnet temperature cannot be much higher than 5 K without substantially reducing the safety factor.

Chapter 4
Active Magnetic Regenerator Test Apparatus

4.1 Apparatus Design

The AMR sub-system is a component designed to be independent of the magnet. The combination of magnet and AMR sub-systems comprises the AMR Test Apparatus (AMRTA.) A cylinder carrying two AMR beds reciprocates in and out of a high field region. The cylinder carries two heat exchangers on either end that act as the hot heat sinks. Cooling fluid is carried to the heat exchangers by flex hoses, which can be water, LN_2, or some other fluid. Helium is used as the heat transfer fluid in the AMR with a maximum pressure of 10 bar. The gas oscillates sinusoidally through the cylinder by a gas displacer mechanically coupled to the cylinder drive shaft. Flex hoses attach to feed throughs on the vacuum vessel and to fittings on the cylinder. A DC motor and regenerative controller drive the entire apparatus. Operating frequencies can be set between 0.2 and 1.2 Hz. Currently, in place of a cold heat exchanger, two heaters in between the AMR beds act as a heat load. A schematic of the apparatus is shown in Figure 4.1.

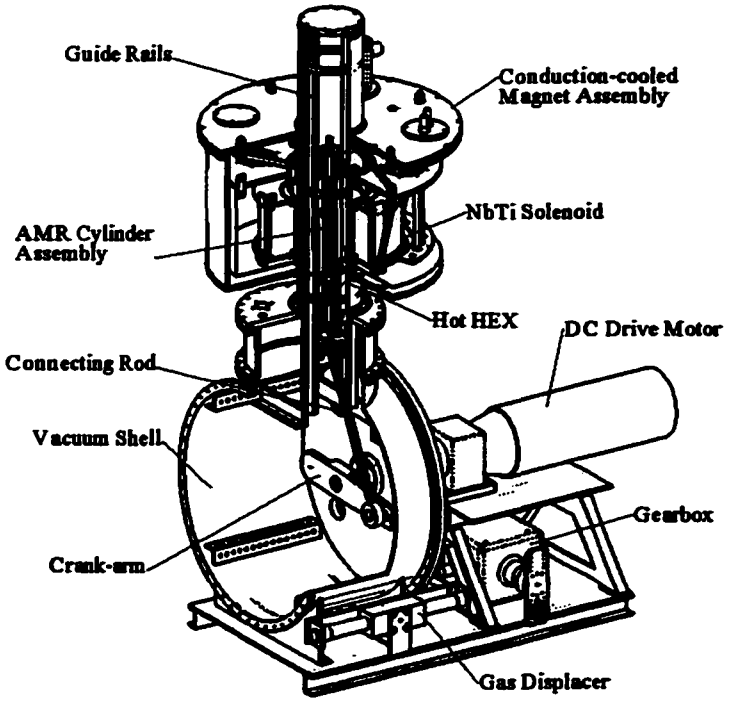

Figure 4.1 AMR Test Apparatus cut-away. Major components are labeled. Flex hoses, fluid lines and instrumentation are not shown.

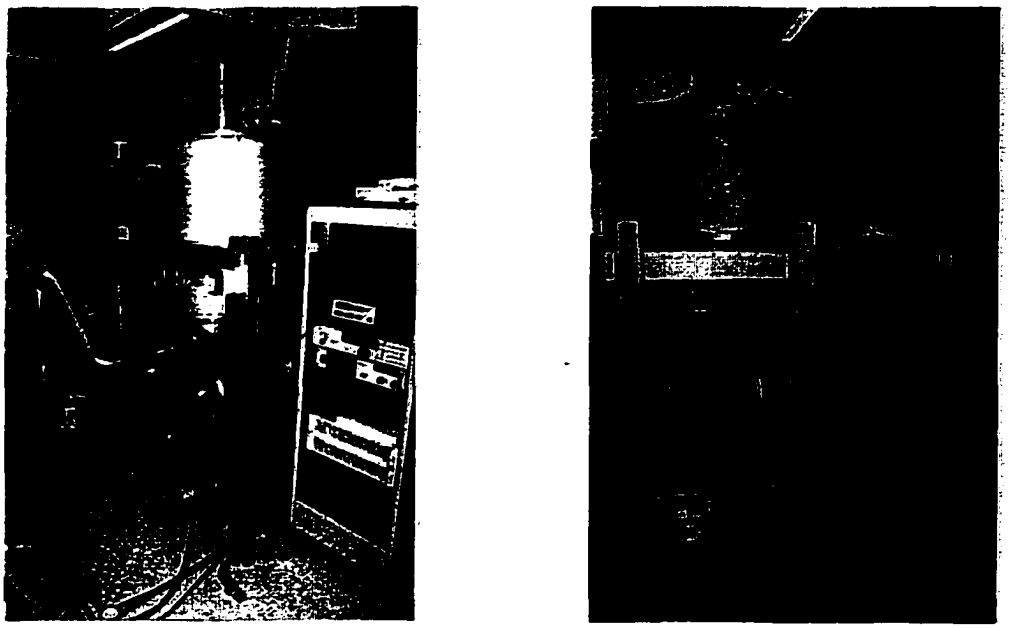

Figure 4.2 Assembled AMR Test Apparatus in operation (left); profile view (right).

Figure 4.1 shows the conceptual layout with most of the key components. The wiring, electrical connections, gas lines, coolant lines, feed throughs and many other items are not shown for clarity. Figure 4.2 shows more of the assembly details including a stand needed to support the field generator in position above the AMR system. The vacuum housing consists of a stainless steel shell, an aluminum extension with top plate, two one inch aluminum plate end-caps, and a stainless steel rolled tube. The vacuum tube is capped and sealed with an aluminum ring containing o-rings and a separate blank flange. The housing is mounted on a wheeled aluminum base plate also used to mount the drive system. To minimize the convective heat leak during low temperature testing, the shell is evacuated to a vacuum of 10^{-5} torr or better.

The magnetic forces on the cylinder generate large reversing torques. Results of force modeling (see Appendix A) indicate that the magnetic torque with Gd beds is on the order of 150 N-m at 1 Hz with a field of 5 T (depending on regenerator volume and temperature.) A rotary shaft feed through from FerroFluidics™ transmits this torque into the vacuum chamber. Because the feed through uses a magnetic field to contain the sealing fluid, the device must not be exposed to a background field strong enough to overcome the rare earth magnets. The stray field strength at the location of the feed through was determined to be approximately 250 G and consultations with the manufacturer indicated that this field would not compromise operation. The fatigue limit of the shaft is sufficiently high so that reversing loads will not limit the life of the device.

A 3 hp DC motor and regenerative drive package is used to harmonically reciprocate the cylinder. This drive package allows a 20:1 turndown ratio for frequency, and speed regulation within 5% for a 95% load change. Coupled through a reducing gearbox, this allows the operating frequency to be set at a maximum of 1.2 Hz.

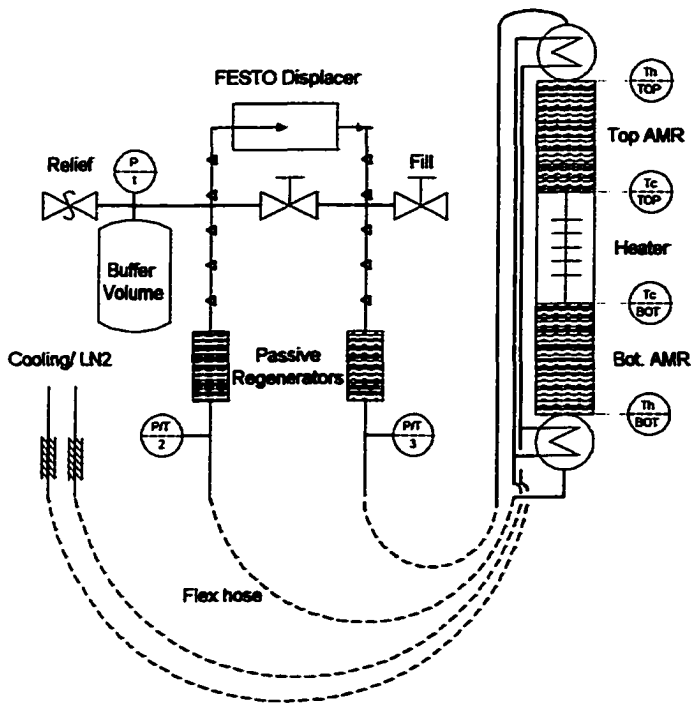

Figure 4.3 Schematic of the gas transfer and cooling fluid system for the AMR Test Apparatus.

4.1.1 Fluid Transfer System

The fluid transfer system encompasses those components that contain and control the movement of fluid through ther regenerators. A schematic of the complete fluid transfer system is shown in Figure 4.3. Each end of the cylinder carries a shell and tube heat exchanger rated for cryogenic service. On the tube side, helium gas rejects heat to a cooling fluid. A series of tubes connect the heat exchangers to flex hoses at the base of the cylinder and these hoses connect to feed throughs on the top of the vacuum shell and then to the external coolant source. For 77 K operation, one of the coolant lines connects to a LN_2 dewar while the other hose exhausts the nitrogen to atmosphere. Inside the vacuum chamber, passive regenerators are used with low temperature testing to minimize the heat load on the heat exchangers and allow the gas displacer to be at room temperature outside of the vacuum shell. The passive beds are approximately 25 mm in diameter and 75 mm long and are composed of 450 μm stainless steel spherical particles.

The heat transfer fluid is forced to oscillate through the regenerator beds by using a reciprocating, hermetically-sealed, rodless cylinder from Festo™. A diagram of the displacer is shown in Figure 4.4. The displacer is forced to reciprocate about its center position by coupling to the drive motor through a gearbox. Since it is mechanically coupled, the phasing between the blow waveform and the regenerator position is fixed; however, it can be adjusted by changing the angular position of the displacer crank-arm. The stroke length of the gas displacer can also be set by changing the throw on the crank. Finally, another degree of freedom is the gas pressure. The displacer is rated to 8 bar nominal with a maximum of about 10 bar. The only clear drawback with the displacer at this point is the friction between the seals and the cylinder; however, the power dissipated by friction in the displacer is small compared to the power required to drive the cylinder and, moreover, is out of phase with the cylinder so does not significantly influence the drive rating.

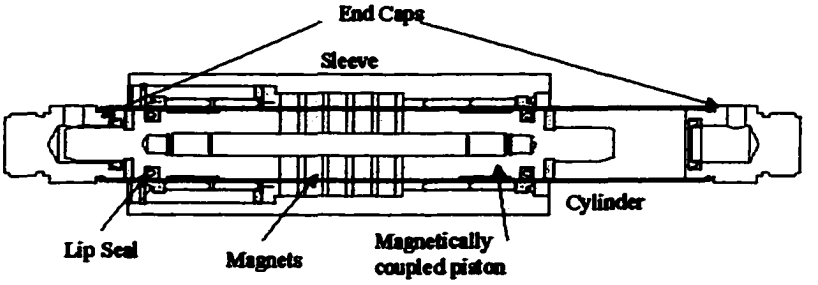

Figure 4.4 Internal cross-section of the Festo™ fluid displacer.

One of the key aspects of AMRR design is to have a small pressure drop in order to produce high efficiency; however, this must be optimized against heat transfer, porosity and other parameters. Pressure drop through the entire flow system was calculated using empirical correlations for friction factor (described further in section 4.2). Figure 4.5 shows the pressure drop in the main components of the fluid transfer system as a function of angular position (the passive regenerators are not shown). As is to be expected, the dominant loss is the regenerator. For the conditions shown, the peak pressure drop is nearly 1 bar across both regenerator beds. The pressure drop across the regenerators is relatively high operating at 0.8 Hz, but decreases rapidly as the frequency is lowered. Currently, particles are the most readily available geometry; however, other configurations need to be investigated for optimized high frequency operation.

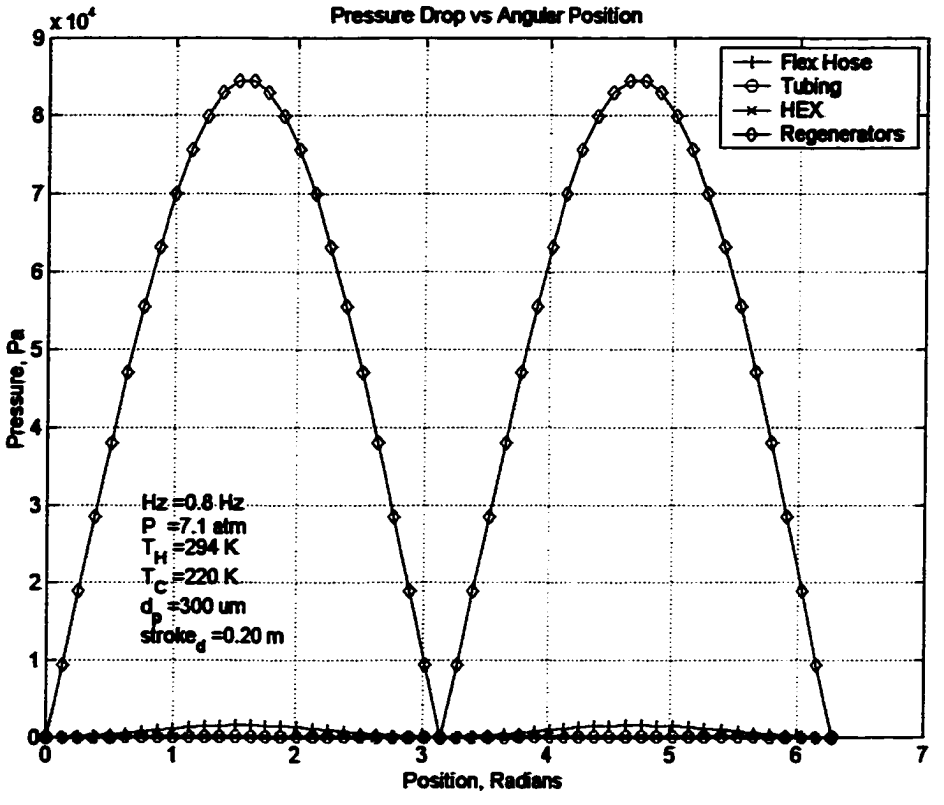

Figure 4.5 Pressure drop through the major components in the fluid transfer subsystem as a function of angular position.

4.1.2 Cylinder Assembly

The cylinder assembly is the heart of the apparatus. This component carries the regenerators and is oscillated in and out of the high field region of the magnet. Unlike other reciprocating AMRs, the hot heat exchangers are carried on the cylinder in order to minimize the dead volume between the heat sink and the AMR beds. It is non-metallic to limit thermal conduction and eddy-current heat generation, strong enough to withstand the magnetic forces on the regenerators, and gas tight to contain helium at pressures up to 10 bar. A 1-¼ inch outer diameter G-10 tube with 1/8 inch thick wall makes up the cylinder housing. A wire harness connects to a feed through on the vacuum chamber and transmits PRT signals, heater current, and sensor excitation to the cylinder. Stainless steel flex hoses attach the cylinder lines to feed throughs on the vacuum shell. Figure 4.6 shows the complete cylinder assembly and Figure 4.7 shows the internal arrangement. The cylinder rides on as many as six bearings on rails inside the vacuum bore. Commercial self-aligning contact bearings made of a Teflon impregnated material called Frelon™ are used.

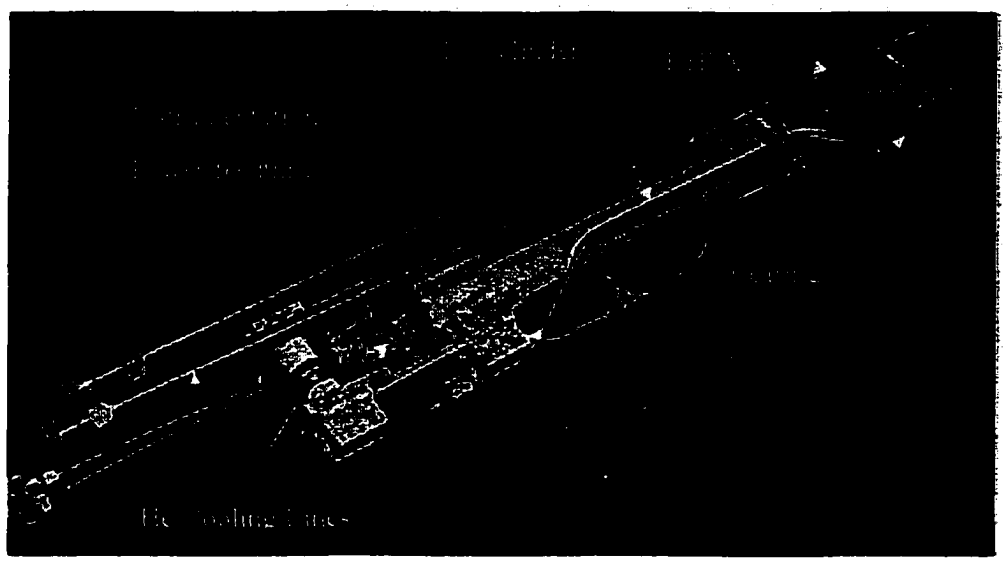

Figure 4.6 AMR cylinder assembly showing G-10 tube, fluid lines bearings and heat exchangers.

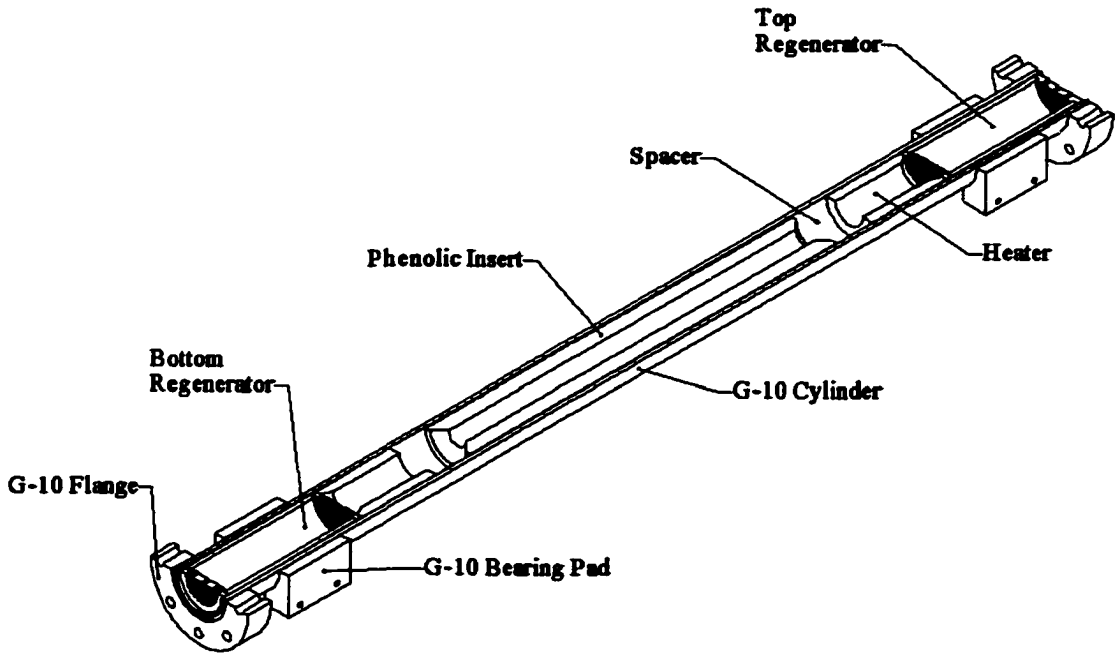

Figure 4.7 Cylinder cross-section showing the location of the regenerators and other sub-components.

The nominal stroke of the cylinder is 0.5 m (total movement of cylinder) based upon the field shape produced by the magnet subsystem and the need to ensure that the low field is as small as possible. From the maximum field position the cylinder moves up 0.25 m and down 0.25 m in order to move each bed from the high field region to a low field region. One of the desirable design characteristics of the apparatus is the ability to change the stroke length. Replacing the 0.25 m crank pin with one that has the pin offset to either a shorter or a longer radius changes the stroke. The stroke length can be varied a maximum of +/- 4.5 cm. If the stroke is increased, "overstroked," or decreased, "understroked," the field distribution in the bed can be varied. For understroking, the cold ends of the regenerator beds see a larger change in applied field than the hot ends. The reverse is true for overstroking. Because the working materials currently available have adiabatic temperature changes that vary with temperature in a non-ideal fashion, some valuable insights may be gained by the ability to change the field distribution.

4.2 Regenerator Fabrication

Regenerators are designed to maximize heat transfer while trying to minimize pressure drop and other modes of entropy generation. To produce large heat transfer rates, the wetted area and heat transfer coefficient are large. In practice, this requirement is met by the use of geometries with high specific areas such as particle beds, mesh screens, parallel plates, foils, etc. In passive regenerators, materials are often chosen for high volumetric heat capacities. In an AMR, the materials are chosen based primarily on the magnetocaloric effect. Particle beds are often used since it can be expensive to have the materials processed into other more effective geometries. There is a vast literature associated with thermal regenerator design issues and the reader is referred to other studies for more detailed information [55].

A novel problem associated an AMR as compared to a passive bed is the magnetic body force the material is subject to. When the AMR is composed of particles, the magnetic force acting on each particle can dislodge particles and destroy the bed. Furthermore, even if the particles are well contained the bed, housing, and apparatus must be designed to accommodate the net magnetic force, which can be large. Other experimental devices have used elaborate regenerator structures in order to accommodate the magnetic forces. Here, the particle beds are epoxy impregnated inside a phenolic shell to produce a monolithic particle bed [52]. This process creates a simple and compact regenerator that acts as one structural unit. Thus, it is relatively easy to deal with the magnetic forces on the particles. The device is then designed in such a way that the shell is adequately supported and, as long as the designer has ensured that the net force on the

bed does not exceed the shear strength of the epoxy bond between the bed and the shell, the regenerator and particles are constrained.

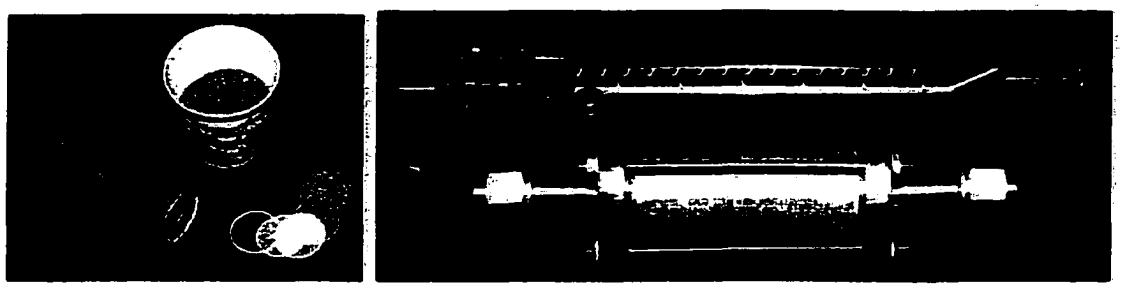

Figure 4.8 Fabrication of a single-section single material bed (left). Regenerator prior to pressure drop test (right).

Figure 4.8 shows the components that make up a particle bed AMR and an assembled bed prior to a pressure drop test. A phenolic shell and end-caps contain the material while the caps are drilled with many small holes to allow for gas flow. A 200 mesh stainless steel screen supports a 50 um and 37 um nylon mesh. A delrin retaining ring holds the screens in position and seals the inside edge of the tube to prevent particles from leaking by the wall prior to epoxy impregnation. The essence of the monolithic process is to coat all the particles with a thin layer of epoxy so that the particles bond together into one structural unit while minimizing the reduction in porosity. As discussed above it is also important that the bed bond to the phenolic shell. Once the fabrication process is completed, a shallow channel is milled down the side of the regenerator housing. The milled channel is used to locate the wires for the PRTs and the heaters in the cold section. It may also be possible to drill holes through the phenolic to acquire a temperature profile through the bed using PRT temperature sensors. The picture on the right side of Figure 4.8 shows the regenerator mounted in flanged fittings prior to testing the pressure drop through the bed.

If the epoxy impregnation process is performed correctly, the pressure drop through the monolithic bed should deviate little from that for a particle bed without impregnation. There are several correlations for estimating the pressure drop through packed beds most of which are based on the friction factor definition [55]. The friction factor can be considered as the energy dissipation per unit volume in a flow relative to the average kinetic energy per unit volume of the flow stream. Using the Fanning friction factor, f, the pressure drop can be determined from [56],

$$\frac{\Delta P}{L} = \frac{f4}{D_p}\frac{G^2}{2\rho}. \tag{4.1}$$

G is the interstitial mass flow per unit area, D_p is the particle diameter, ρ is the density, and L is the length. In this case the correlation for the friction factor is,

$$f = \frac{1-\alpha}{\alpha}\left(0.875 + \frac{(1-\alpha)^2}{\alpha}\frac{142.5}{\mathrm{Re}}\right) \tag{4.2}$$

Re is the particle Reynolds number and is defined as,

$$\mathrm{Re} = \frac{D_p G}{\mu}. \tag{4.3}$$

μ is the fluid viscosity.

Gd regenerator parameters:

- Mass Gd: 195.6 g
- ID 25 mm
- Length: 79 mm
- Particle diameter: 212>d>180 um
- Porosity (pre-epoxy): 0.39 (est.)

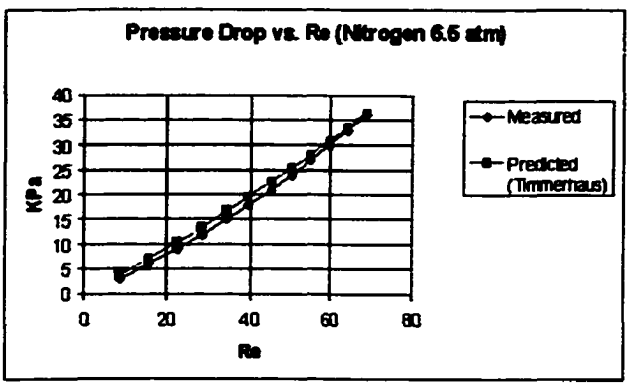

Figure 4.9 Regenerator properties and results of a pressure drop test.

Figure 4.9 shows some of the regenerator parameters and the experimental pressure drop as a function of particle Reynold's number. As can be seen, the measured pressure drop compares well to the empirical correlation for pressure drop through randomly packed spherical particle beds.

4.2.1 Puck Fabrication

A brief description of the regenerator fabrication procedure follows:

1. Prepare Stycast-1266 epoxy containing Part A and Part B and dilute the mixture with acetone to produce a water-like fluid;
2. Mix the particles into the epoxy solution stirring well to ensure that all of the particles are covered with epoxy;

3. Pour the particles into a prepared phenolic housing (end-cap and screens in place on the bottom, both sprayed with mold release to facilitate removal later;)
4. Tap the shell repeatedly with a stiff object like a glass stir-stick to force bubbles out and to help settle the solid particles evenly;
5. Use the epoxy that has drained out to pour back into the shell while continuing to tap (this may have to be performed a number of times to produce an even particle surface near the top of the shell;)
6. Place screens and end-cap on the shell to close. Clamp the regenerator in the flanged fittings and attach to nitrogen bottle;
7. Blow nitrogen through the bed for a couple of minutes, flip the regenerator around and blow through in opposite direction. Repeat until no fluid is observed to be leaving the bed;
8. Allow epoxy to cure at room-temperature for 24 hours before removing the end-caps and screens; and,
9. Post-cure the single bin in an oven at 45 degrees Celsius for at least 2 hours.

The above procedure ensures that the particles are all covered with epoxy and that the monolithic bed is bonded to the phenolic housing. The first regenerators made were the full-length versions as shown in Figure 4.8. Although the fabrication procedure described above was used successfully to make monolithic beds, a shortage of refrigerant material prompted a slight modification. Instead of making regenerators of the required length as one monolithic body, the AMRs were built up of identical pucks with a length to diameter ratio of one. The phenolic housing for each puck was turned in an appropriate fashion so that the sections fitted together with a slight interference fit and then epoxied together to make the shell gas tight and a single structure. Figure 4.10 shows a single puck and assembled two-puck regenerators.

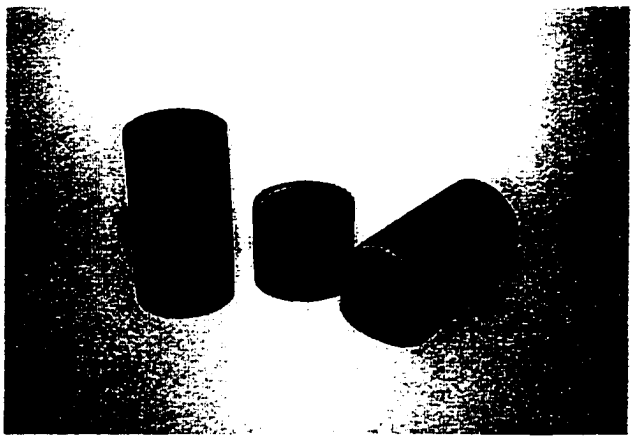

Figure 4.10 Single pucks were fabricated and then used together to build up larger regenerators.

Besides allowing puck sections to be re-used, an additional advantage to this method is that it makes it easier to ensure that epoxy is not being trapped in the beds thereby reducing the void volume. Six pucks using Gd were fabricated for the tests. The puck parameters are shown in Table 4-1.

Table 4-1. Puck masses.

Puck	Shell (g)	Epoxy (g)	Gd (g)
1	9.13	0.2	63.58
2	9.52	1.39	62.86
3	9.56	0.53	63.91
4	9.22	0.64	62.19
5	9.01	0.52	64.38
6	9.53	0.56	62.94

As can be see, fairly consistent results were obtained. In the case of puck-2, a significant residual mass of epoxy remains. Although on a mass-wise basis, the amount of epoxy is substantially less than the refrigerant mass (a desirable attribute so that the parasitic heat capacity is low) because the density of cured Stycast 1266 epoxy is approximately 8 times less than Gadolinium, the volume fraction of epoxy can be large. This can lead to larger pressure drops which, although not critical here, leads to a decrease in device efficiency due to larger pumping power requirements.

Chapter 5
Numerical Model

The purpose of this chapter is to derive a numerical model describing the operation of an AMR. Specifically, the solution domain is chosen to simulate the AMR Test Apparatus described in the previous chapter. The system is modeled in one spatial dimension using the fluid and solid energy equations.

5.1 Model Derivation

Thermal regenerator modeling often assumes plug flow prevails and one spatial dimension is sufficient to model the porous medium. Thus, the relations of primary interest are those describing the thermal energy change of the heat transfer fluid and the solid. In passive regenerator modeling, the regenerator solid has no work mode and the solid energy equation is easily derived. Models of AMRs incorporate or neglect various terms balancing desired accuracy with numerical simplicity. The general relations for an AMR can be derived starting with the heat equation in Eulerian coordinates [57],

$$\rho T \frac{Ds}{Dt} = \rho \frac{Dh}{Dt} - \frac{DP}{Dt} = -\nabla \cdot \vec{q} + q''' + \Phi \tag{5.1}$$

where s is the specific entropy, h is the specific enthalpy, P is the thermodynamic pressure, $\vec{q}$ is thermal diffusion, q''' is a volumetric source term, and Φ is a term representing energy dissipation (viscous dissipation for a fluid.) It is now assumed that Fourier's law is valid and the volumetric source term is due to heat transfer between solid and fluid and can be described by Newton's law of cooling. It is convenient to use the thermodynamic relations for a differential change in entropy to write the specific equations,

$$ds = \frac{c_p}{T} dT - \frac{\beta}{\rho} dP \tag{5.2}$$

$$ds = \frac{c_B}{T} dT - \left(\frac{\partial s}{\partial B} \right)_T dB \tag{5.3}$$

where Equation (5.2) is for the fluid substance and Equation (5.3) is for the magnetic material. For a second order magnetic material, Maxwell's relations give the following identity,

$$\left(\frac{\partial s}{\partial B}\right)_T = \left(\frac{\partial m}{\partial T}\right)_B. \tag{5.4}$$

(Note: B has been used in place of $\mu_0 H$ for the applied field.) The coefficient of thermal expansion is defined as

$$\beta \equiv -\frac{1}{\rho}\left(\frac{\partial \rho}{\partial T}\right)_P. \tag{5.5}$$

The differential equations for the energy change of solid and fluid can be written in terms of per unit length instead of per unit volume by multiplying all terms by the cross-sectional area of the AMR, A, and accounting for porosity, α (assuming the area and porosity are constant along the length of the AMR.) Substituting Equations (5.2) and (5.3) in Equation (5.1), applying Fourier's law and Newton's law of cooling, the coupled 1-dimensional fluid and solid energy equations describing an AMR bed can now be written in the following form:

$$\alpha A \rho_f c_p \left(\frac{\partial T_f}{\partial t} + u\frac{\partial T_f}{\partial x}\right) - \alpha A \beta T_f \left(\frac{\partial P}{\partial t} + u\frac{\partial P}{\partial x}\right) = \frac{\partial}{\partial x}\left(\alpha A k_f \frac{\partial T_f}{\partial x}\right) + hA'(T_s - T_f) + S_f' \tag{5.6}$$

$$(1-\alpha)A\rho_s \left(c_B \frac{\partial T_s}{\partial t} + T_s \left(\frac{\partial m}{\partial T}\right)_B \frac{\partial B}{\partial t}\right) = \frac{\partial}{\partial x}\left((1-\alpha)A k_s \frac{\partial T_s}{\partial x}\right) + hA'(T_f - T_s) + S_s'. \tag{5.7}$$

α is the porosity, A is the cross-sectional area of the AMR bed, ρ is the density, c is the heat capacity per unit mass, u is the fluid velocity, β is the coefficient of thermal expansion, P is the pressure, k is the thermal conductivity, h is the heat transfer coefficient, A' is the surface area per unit length, S' is a general source term per unit length (in place of Φ), B is the magnetic field strength ($\mu_0 H$), and m is the mass magnetization of the refrigerant. Equation (5.6) is the energy equation for the heat transfer fluid while Equation (5.7) is for the solid refrigerant.

The time and space variables can be non-dimensionalized using the following definitions,

$$t^* \equiv \frac{t}{\tau_B}, \tag{5.8}$$

$$x^* \equiv \frac{x}{L}, \tag{5.9}$$

where τ_B is the blow period, and L is the regenerator length. In the one-dimensional case, mass flow rate is a more useful parameter and is given by $\dot{m} = \alpha A \rho_f u$. Making these substitutions, Equations (5.6) and (5.7) can be written,

$$\frac{\alpha A \rho_f c_p}{\tau_B}\frac{\partial T_f}{\partial t^*} + \frac{\dot{m} c_p}{L}\frac{\partial T_f}{\partial x^*} = \frac{1}{L}\frac{\partial}{\partial x^*}\left(\frac{\alpha A k_f}{L}\frac{\partial T_f}{\partial x^*}\right) + hA'(T_s - T_f) + \left\{S_f' + \alpha A \beta T_f\left(\frac{\partial P}{\partial t} + u\frac{\partial P}{\partial x}\right)\right\} \quad (5.10)$$

$$\frac{(1-\alpha) A \rho_s c_B}{\tau_B}\frac{\partial T_s}{\partial t^*} = \frac{1}{L}\frac{\partial}{\partial x^*}\left(\frac{(1-\alpha) A k_s}{L}\frac{\partial T_s}{\partial x^*}\right) + hA'(T_f - T_s) + \left\{S_s' - (1-\alpha) A \rho T_s\left(\frac{\partial m}{\partial T}\right)_B \frac{\partial B}{\partial t}\right\}. \quad (5.11)$$

The terms in parentheses have not been normalized because they will be included in the general source term and dropped.

Equations (5.10) and (5.11) are the full equations for the solid-fluid system and can be numerically solved as is. An alternative approach is implied by the groupings in parentheses. In general, pressure variations in both time and space are small relative to the other terms and may be neglected for simplicity. If one chooses to include these terms, the impacts can be determined using empirical correlations instead of also solving the continuity and momentum equations. In this case, they appear as a source term; hence, the grouping in parenthesis.

Equation (5.11) is derived by the application of Maxwell's equations for a *simple* magnetic substance to the energy equation. The term *simple* is included as it specifies the assumption of a single work mode just as the phrase *simple compressible* does. As with the fluid energy equation, one could numerically solve the complete equation; however, there are several good reasons why this may not be the simplest or most accurate method. The property deemed to be of primary importance for AMR cycles is the reversible adiabatic temperature change; the next most important is the heat capacity. This is reflected in the model derivation that follows.

One of the ways of approximating a full cycle is to assume that it is composed of a number of small isofield and adiabatic steps. This is the assumption used by Carpetis [39]. This approximation is similar to a step-wise integration of a curve. In the limit as the step size goes to zero, the integration becomes exact. The validity of this approximation is expected to increase as the number of steps comprising a complete cycle is increased (i.e. as the magnitude of the time step decreases.) Further, this may be an accurate method if the cycle is composed of only four distinct steps as long as the flow and field waveforms are step functions. This type of reasoning has been used in previous models [38]. The major drawback is that, in practice, these types of waveforms (step functions) are not feasible in real devices.

It can be argued that the isofield-adiabatic assumption is not consistent with the physical process occurring. While this may be true for some cycles, it is not necessarily any worse than using the full form with Maxwell's equations if the material exhibits hysteresis. Also, when modeling materials exhibiting first-order magnetic phase changes, the validity of Maxwell's equations is still somewhat questionable [28]. One of the benefits of this approximation is that the adiabatic temperature change and heat capacity properties are used directly, each of which can be measured independently. These can be experimentally derived (most accurate), predictions from MFT calculations, or results from other models.

The simplified forms of the energy equations for the isofield-adiabatic assumption are:

$$\frac{\alpha AL\rho_f c_p}{\tau_B}\frac{\partial T_f}{\partial t}+\dot{m}c_p\frac{\partial T_f}{\partial x}=\frac{\partial}{\partial x}\left(\frac{\alpha Ak_f}{L}\frac{\partial T_f}{\partial x}\right)+hA'L\left(T_s-T_f\right)+S_f \tag{5.12}$$

$$\frac{(1-\alpha)AL\rho_s c_B}{\tau_B}\frac{\partial T_s}{\partial t}=\frac{\partial}{\partial x}\left(\frac{(1-\alpha)Ak_s}{L}\frac{\partial T_s}{\partial x}\right)+hA'L\left(T_f-T_s\right)+S_s. \tag{5.13}$$

The superscript * has been dropped for simplicity and the equations have been multiplied through by the length, L. It is useful to clearly state the source term definitions in the isofield-adiabatic approximation for later use:

$$S_f\equiv\left(S_f'''+\beta T_f\left(\frac{\partial P}{\partial t}+u\frac{\partial P}{\partial x}\right)\right)\cdot\alpha AL \tag{5.14}$$

$$S_s\equiv S_s'''\cdot(1-\alpha)AL, \tag{5.15}$$

where the terms S''' represent a volumetric power source. Note that the space and time coordinates have not been normalized in the above equations. The energy interaction due to the time varying magnetic field is no longer included in the expression for the solid source; this is a result of the cycle approximation.

The following physical groupings prove useful for clarifying the interaction between solid and fluid equations:

$$\Phi\equiv\frac{\dot{m}c_p\tau_B}{(1-\alpha)AL\rho_s c_B}, \tag{5.16}$$

$$N_{TU}\equiv\frac{hA'L}{\dot{m}c_p}, \tag{5.17}$$

$$R_c \equiv \frac{\alpha \rho_f c_p}{(1-\alpha)\rho_s c_B}, \tag{5.18}$$

$$C_R \equiv \frac{(1-\alpha)AL\rho_s c_B}{\tau_B}. \tag{5.19}$$

Equation (5.16) can be considered a type of *capacity ratio* in the language of heat exchangers. Φ is the ratio between fluid thermal capacity and refrigerant thermal capacity. Equation (5.17) is the well known grouping defining the *Number of Transfer Units*, N_{TU}, and is a measure of heat exchanger effectiveness. R_c is the ratio of fluid and solid thermal masses. C_R is the solid capacity rate. For the sake of simplicity, the following definitions are also made:

$$K_f \equiv \frac{\alpha A k_f}{L} \tag{5.20}$$

$$K_s \equiv \frac{(1-\alpha)Ak_s}{L}. \tag{5.21}$$

Using the above definitions, the energy equations can now be written in the following forms:

$$R_c \frac{\partial T_f}{\partial t} + \Phi \frac{\partial T_f}{\partial x} = \frac{1}{C_R}\frac{\partial}{\partial x}\left(K_f \frac{\partial T_f}{\partial x}\right) + N_{TU}\Phi(T_s - T_f) + \frac{S_f}{C_R}, \tag{5.22}$$

$$\frac{\partial T_s}{\partial t} = \frac{1}{C_R}\frac{\partial}{\partial x}\left(K_s \frac{\partial T_s}{\partial x}\right) + N_{TU}\Phi(T_f - T_s) + \frac{S_s}{C_R}. \tag{5.23}$$

Equations (5.22) and (5.23) are useful forms that correspond to the general energy equations for passive regenerators. Unlike a passive regenerator, the solid heat capacity is a strong function of temperature and magnetic field; thus, in the region of interest, near the phase transition temperature, the energy equations are non-linear and can be computationally intensive.

5.2 State Properties

As was discussed in Chapter 1, materials undergoing a second order magnetic phase transition have large variations in magnetization and heat capacity near the phase transition region. Near the Curie temperature, these properties are strong functions of both field and temperature. Likewise, the magnetocaloric effect (MCE) is dependent on the strength of the magnetic field, magnitude of field change and temperature. The two properties of interest for the model developed using the isofield-adiabatic assumption are heat capacity, c_B, and MCE. Some previous models have used

heat capacity and magnetization data provided by programs based on the Molecular Field Theory (MFT) as formulated by Weiss [59]. A brief description of the MFT model follows.

5.2.1 Molecular Field Model

Weiss' molecular field model is one of the simplest theories explaining the co-operative phenomenon of spontaneous magnetization arising from interactions between magnetic atoms [60]. To account for the behaviour of ferromagnetic materials, Weiss assumed a magnetic atom sees a total field that is due to the applied field, H, and an additional component, H_e, proportional to the average net magnetic moment of the rest of the atoms in the sample;

$$\bar{H}_T = \bar{H} + \bar{H}_e. \tag{5.24}$$

The effective field, H_e, is called the molecular field and is quantified by the molecular field coefficient, γ;

$$\bar{H}_e = \gamma \bar{M}. \tag{5.25}$$

For an isotropic magnetic material the magnetization, $\bar{M}$, in terms of the Brillouin function, $B_J(x)$ is written as,

$$M(T,H) = Ng\mu_B J B_J(x), \tag{5.26}$$

where the magnetization is in the direction of the applied field allowing the removal of the vector. The term g is known as the Landé g-factor and is defined as,

$$g = 1 + \frac{J(J+1) + S(S+1) - L(L+1)}{2J(J+1)}. \tag{5.27}$$

The argument of the Brillouin function is,

$$x = \frac{g\mu_B J(H + \gamma M)}{kT}, \tag{5.28}$$

and the molecular field coefficient is given by,

$$\gamma = \frac{3kT_C}{Ng^2\mu_B{}^2 J(J+1)}. \tag{5.29}$$

T_C is known as the Curie temperature and is an indicator of the strength of the exchange interaction.

The Hamiltonian of the spin system allows the Helmholtz potential, F, to be determined. The thermodynamic properties of interest can then be derived from the application of Maxwell's equations to the free energy. The magnetic entropy is given by,

$$S_M(T,H) = -\left(\frac{\partial F}{\partial T}\right)_H, \tag{5.30}$$

and the magnetic entropy change is determined by,

$$\Delta S_M(T,H) \equiv S(T,H) - S(T,0) = \int_0^H \left(\frac{\partial M(T,H)}{\partial T}\right)_B dH. \tag{5.31}$$

Equation (5.31) is valid when Maxwell's equations are applicable; the integral can be evaluated using Equation (5.26) [59]. The total entropy is obtained using the following,

$$S(T,H) = \Delta S_M(T,H) + S(T,0). \tag{5.32}$$

The entropy at zero field can be determined by,

$$S(T,0) = \int_0^T \frac{c_B(T,0)}{T} dT. \tag{5.33}$$

The heat capacity can be calculated using relations for electronic and lattice contributions or experimental data may be used directly. It is worth noting that the magnetic entropy can also be calculated using the following;

$$\Delta S_M(T,H) = \int_0^T \frac{c_B(T,H)}{T} dT - \int_0^T \frac{c_B(T,0)}{T} dT. \tag{5.34}$$

By definition, Equation (5.34) is true for any material.

5.2.2 Property Estimation

A well-known problem with MFT results is that magnetic heat capacity tends to correspond with experimental results only at conditions away from the Curie temperature ($>\pm 25$ K) [36]. Furthermore, MFT calculations for magnetization tend to be less accurate at temperatures less than T_C [60]. A plot of experimental data for c_B of Gd at 0 and 2 T is compared to MFT data in Figure 5.1 and Figure 5.2. The experimental data is taken from [36].

As can be seen in Figure 5.1, MFT predictions qualitatively mimic experimental heat capacity data fairly well; however, at temperatures near the Curie point and higher, MFT data tend to

underestimate experimental results significantly. Figure 5.2 shows the relative change in the heat capacity of Gd between 0 and 2 Tesla.

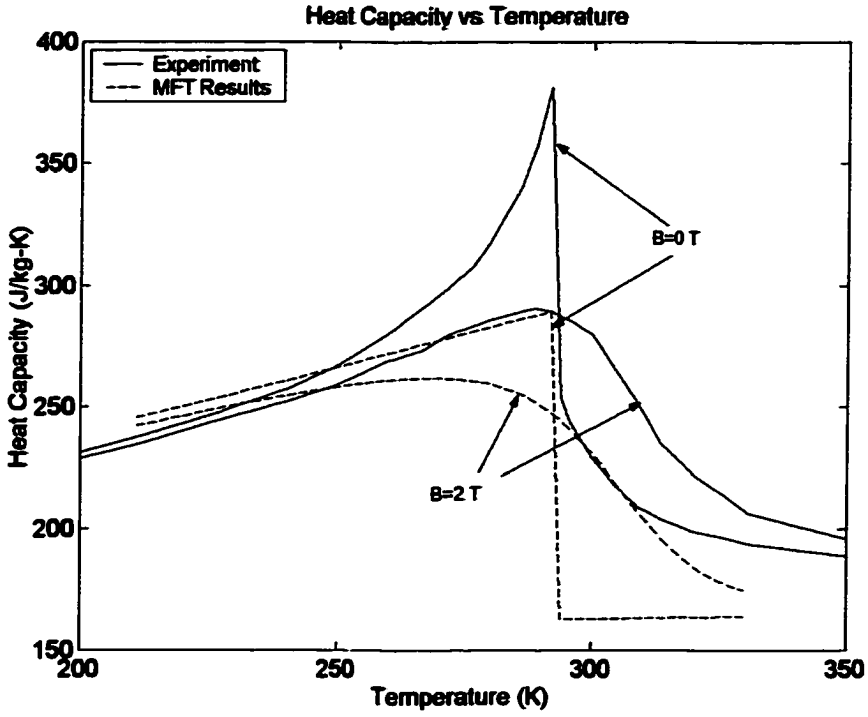

Figure 5.1 Molecular Field Theory and experimental data for heat capacity of Gd at 0 and 2 T.

Heat capacity, c_B, as a function of field strength is not a linear function. To minimize the amount of experimental data required while giving reasonably accurate property data for numerical calculations, the heat capacity is assumed to vary in the following manner,

$$c_B(T,H) \equiv c_B(T,0) + \sin\left(\frac{\pi}{2}\frac{H}{H_{\max}}\right)\left(c_B(T,H_{\max}) - c_B(T,0)\right). \tag{5.35}$$

Equation (5.35) requires heat capacity data at two field strengths only – 0 and maximum field, $H_{\max}$. The assumption of a sinusoidal impact due to field strength is more realistic than a linear assumption as can be seen in experimental results where the suppression of the peak is initially a strong function of field and decreases quickly as B is increased. On the contrary, the MCE is nearly linear for Gd up to about 5 Tesla [36]. Thus, for an adiabatic application of field, the MCE is assumed to vary according to,

$$\Delta T_{ad}(T,\Delta H) \equiv \left(\frac{\Delta H}{\Delta H_{\max}}\right)\Delta T_{ad}(T,\Delta H_{\max}). \tag{5.36}$$

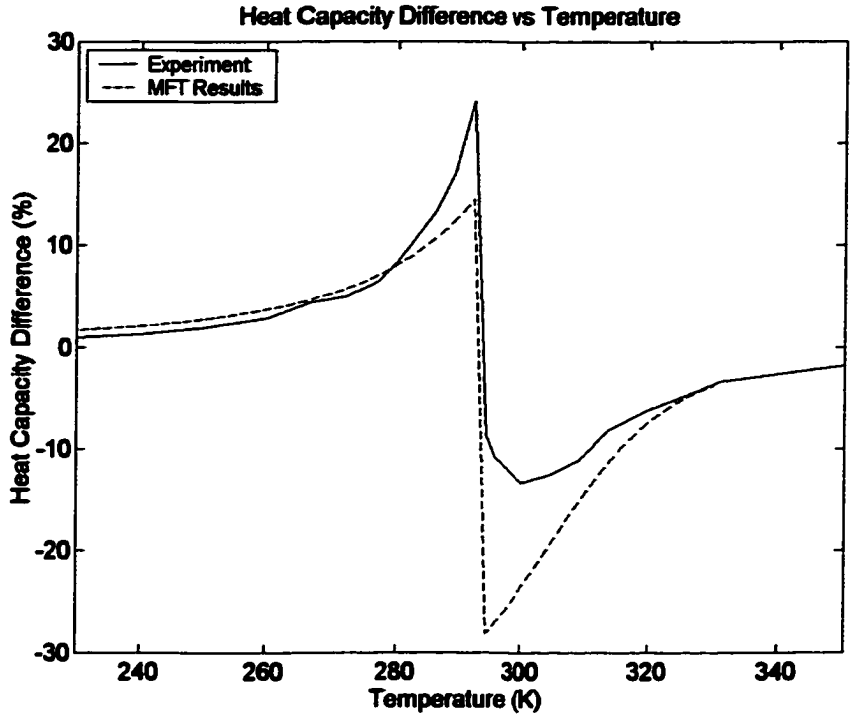

Figure 5.2 MFT and experimental data for relative heat capacity of Gd at 0 and 2 T.

The magnetic field seen by the regenerator is assumed to be unaffected by the presence of the magnetic material. This is not true in reality; however, this is a suitable first assumption for numerical simplicity. To determine the spatial variation of field, the solenoid was modeled in Ansys™ and the predicted field profile along the axis was calculated. A fifth-order polynomial was fit to the reduced field strength (H/H_{max}) and subsequently used in the model to determine field strength and rate of field change as a function of regenerator position. A plot of the field distribution on the solenoid axis is shown in Figure 5.3. Modeling other systems with different field profiles is relatively easy. All that is required is a reduced field distribution as a function of position.

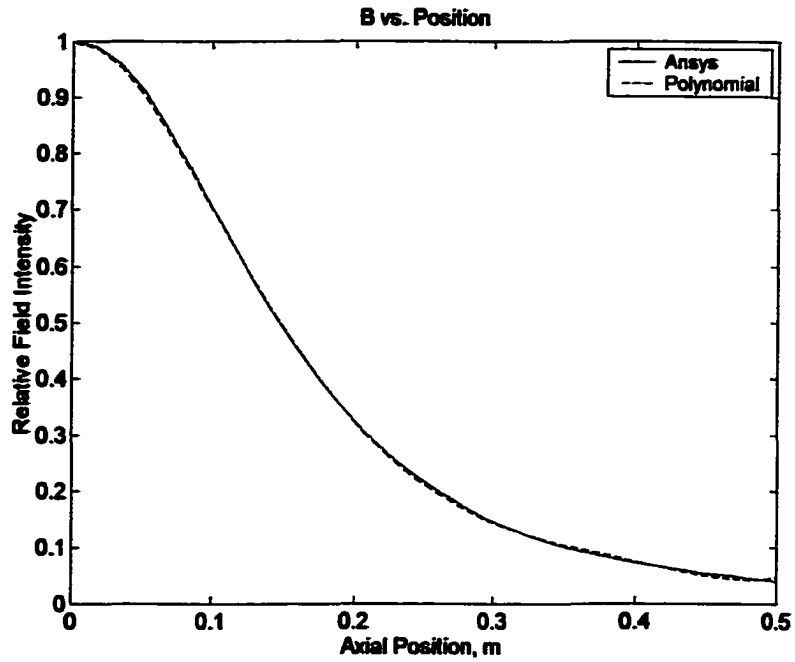

Figure 5.3 The relative field strength along the solenoid axis where the origin is the magnet center.

5.3 Solution Method

Numerical solution of the coupled energy equations for the solid matrix and fluid in a regenerator are typically computationally intensive problems. This is true for passive regenerators as found in many cryocoolers, but can be more of a problem with an AMR where variables can change abruptly and the solid equation is highly nonlinear. For the simulations discussed in this thesis, the system being modeled is the cylinder containing the regenerators. The energy equations are solved using a scheme known as the implicit-correction method.

5.3.1 Model Domain

The physical region being modeled encompasses more than just the regenerator beds. The spatial domain of interest is shown in Figure 5.4. The system is made up of the regenerator beds and the G-10 cylinder. A void space in the center holds the heaters (cold heat exchangers) and the hot ends (left and right) have a small void space representing the transition from the cylinder to the hot heat exchangers. A complete cycle of the system is modeled by assuming the system is temporally symmetric i.e. the blow is modeled from 0 to τ_B (half of the cycle period) which, with the sinusoidal waveform, starts and ends with $\dot{m} = 0$. Instead of reversing the blow to model the

second half of the cycle, the domain is flipped from left to right and then the last half of the cycle is completed. This simplification reduces the amount of memory required.

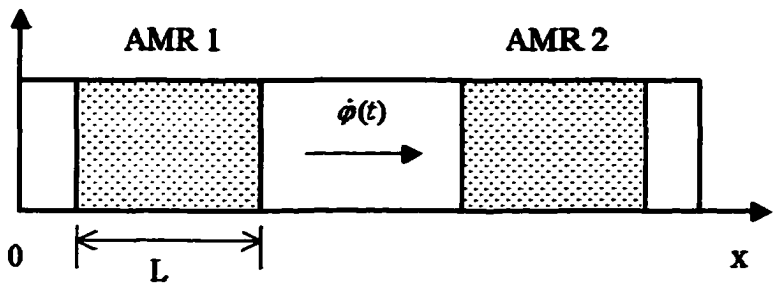

Figure 5.4 The model domain encompasses two regenerators as well as a cold section (where the cold heat exchanger would be) and a small void space on the hot ends of the regenerators.

To account for phase differences between the blow and the applied field a phase difference is incorporated into the field waveform. The blow phase is the reference point with the blow starting at $t = 0$. In fact, this is opposite to the actual conditions in the AMR Test Apparatus where the displacer offset is set to adjust the phasing. This does not impact the model approach as either the flow of the field could be used as a reference point.

5.3.2 Numerical Scheme

The solution of the coupled system represented by Equations (5.22) and (5.23) is performed using a finite volume technique known as the implicit correction scheme [61]. Patankar describes common methods used to solve convection-diffusion problems with the finite volume formulation [66]. The different methods are characterized by the scheme used to determine the interface properties i.e. upwind, central difference, power-law or exponential. These schemes are developed assuming the simple convection-diffusion equation describes the physical problem.

The simple convection-diffusion equation assumes that the effects of transverse heat transfer are small; however, in regenerative processes found in most cryocoolers, transverse heat transfer is usually the dominant term describing the fluid-solid system. Although a scheme like the exponential formulation gives an exact solution to the convection-diffusion equation, its use in a regenerator model leads to a larger number of nodes and many iterations [61]. The implicit correction method is developed based upon an exact solution to the transverse heat transfer-convective problem. Axial conduction and diffusion are treated as small perturbations.

Although the numerical implementation of the implicit-correction scheme is a little more time consuming than the methods described by Patankar, the method converges rapidly and requires a relatively small number of nodes to give accurate results.

5.3.3 Boundary Conditions and Convergence

The model domain makes the boundary conditions easy to specify. For the solid equation the boundary conditions are,

$$\begin{aligned} T_s(x=0) &= T_H, \\ T_s(x=N) &= T_H. \end{aligned} \tag{5.37}$$

The boundary conditions for the fluid are set knowing that flow is from left to right, the fluid enters the cylinder after leaving the hot heat sink, and the heat transfer coefficient in the void space prior to the heat exchanger on the right hand side is small;

$$\begin{aligned} T_f(x=0) &= T_H, \\ \frac{d}{dx}T_f(x=N) &= 0. \end{aligned} \tag{5.38}$$

The solid and fluid equations are iteratively solved until the relative error in any nodal temperature is less than 10^{-5}. Furthermore, the cycles are marched until periodic steady-state conditions are reached; steady-state is assumed when the relative change in the temperature profiles at the start of two consecutive cycles are less than 10^{-5}.

5.4 Magnetic Work Considerations

The numerical model described above is used to help explain observed experimental data and to provide insight into AMR behavior. Results discussed in this thesis are based upon this model. However the ability to model first-order materials and materials with significant hysteresis is of interest due to recent material developments (see Chapter 1.) Therefore, it is worth discussing what further modifications would be required to accurately model hysteretic magnetic systems.

The energy equation describing the magnetic refrigerant (Equation 5.7) is derived assuming the magnetization is a single-valued function of applied field i.e. reversible. Let us examine the magnetic work term without the reversible assumption. In general, the incremental magnetic work term can be written in the following form [67],

$$\delta w_{mag} = \vec{B}_a \cdot d\vec{m}_T \tag{5.39}$$

where $\bar{B}_a$ is the external magnetic field strength and $\bar{m}_T$ is the total mass magnetization; hence, δw_{mag} is the work per unit mass. If we assume the total magnetization is made up of a reversible component and an irreversible part we can write the following [68],

$$\bar{m}_T = \bar{m}_{rev} + \bar{m}_{irr}. \tag{5.40}$$

Using the above in Equation (5.40) the magnetic work is,

$$\delta w_{mag} = \bar{B}_a \cdot d\bar{m}_{rev} + \bar{B}_a \cdot d\bar{m}_{irr}. \tag{5.41}$$

Thus, the magnetic work done on the system is made up of a reversible change in magnetization and a dissipative term due to irreversible magnetization.

A magnetic field known as the demagnetizing field, H_d, is created in a body of finite size in the opposite direction to the magnetization and is proportional to the magnitude of magnetization [69]. Experimental measurements of magnetic properties tend to use small samples with a large aspect ratio and the long axis is oriented in the direction of the applied field. This is to ensure that the demagnetizing field is negligible. The demagnetizing field can be written as a function of the magnetization,

$$\bar{H}_d = -N_d \bar{M}. \tag{5.42}$$

N_d is a dimensionless number accounting for geometry and magnetization. In the case of uniform magnetization, a uniform demagnetizing field is generated only for the case of an elliptic body. Determining the magnitude of the demagnetizing field for any geometry is a difficult process when the magnetization is not uniform. To further complicate things, the magnetization of a material is a function of the sum of the applied field and the demagnetizing field,

$$\bar{H}_{in} = \bar{H}_0 - N_d \bar{M}, \tag{5.43}$$

so,

$$\bar{m}_T = \bar{m}(\bar{H}_0 - N_d \bar{M}). \tag{5.44}$$

Experimental measurements are performed so that N_d is near zero and the demagnetizing field can be neglected. In an AMR of finite size, the demagnetizing field may not be negligible. Not only is geometry a concern, but also the magnetization of the bed is a function of temperature and, therefore, position. Using magnetization data for Gd with an applied field of 2 T we find the following: at 295 K the magnetization is approximately 0.95 T ($\mu_0 M$), whereas at a temperature

of 250 K the magnetization is 1.6 T. For low field operation (0-2 T), this temperature effect could influence temporal response on an AMR.

For a cylinder with a uniform magnetization, a length to diameter ratio equal to 3, and the applied field parallel to the long axis $N_d \cong 0.08$. For a long cylinder with a perpendicular field $N_d \cong 0.5$[69]. These figures are for reference only. With low applied fields (<2 T), the demagnetizing effects are expected to be more significant than for high fields (>5 T). In the latter case, if the temperature is well below the Curie temperature, the refrigerant materials are magnetically saturated and the demagnetizing field will be much smaller on a relative basis to the applied field. As stated earlier the situation is much more complex in an AMR because, in general, magnetization is a function of position. The geometric-magnetic interaction on the magnetic work in an AMR is an area for further study.

Returning to the magnetic work, assuming the reversible magnetization is a function of H_0 and H_d we can write the total differential of the magnetization as,

$$d\bar{m}_{rev} = \left(\frac{\partial \bar{m}_{rev}}{\partial \bar{H}_0}\right)_{H_d} d\bar{H}_0 + \left(\frac{\partial \bar{m}_{rev}}{\partial \bar{H}_d}\right)_{H_0} d\bar{H}_d . \tag{5.45}$$

The incremental magnetic work is then,

$$\delta w_{mag} = \bar{B}_a \cdot \left(\frac{\partial \bar{m}_{rev}}{\partial \bar{H}_0}\right)_{H_d} d\bar{H}_0 + \bar{B}_a \cdot \left(\frac{\partial \bar{m}_{rev}}{\partial \bar{H}_d}\right)_{H_0} d\bar{H}_d + \bar{B}_a \cdot d\bar{m}_{irr} . \tag{5.46}$$

The terms in parentheses are differential susceptibilities; the former is equivalent to experimental susceptibilities when $H_d = 0$ while the latter is due to some general demagnetizing field. Based on the above considerations it is expected that this term will be a function of position in the bed, bed geometry, and time. For the second-order materials under consideration in this thesis, the irreversible magnetization term is usually small and is neglected in the model. Demagnetizing fields are also assumed small.

5.5 Demagnetizing Field

To the knowledge of the author, there have been no studies exploring demagnetization in AMRs; however, as discussed above, it could have a significant impact on AMR performance. For experiments performed at low applied fields, demagnetization is expected to have a larger impact for fields where the material is nearly magnetically saturated. However, since second-order magnetic materials operate near the transition temperature the material will not be saturated.

Thus, even for high field operation, demagnetizing fields may be a concern. A simple numerical study to investigate the influence of demagnetization was performed using finite element magnetostatic software.

An axis symmetric two-dimensional model of an AMR was created as shown in Figure 5.5. The modeled bed has a length to diameter ratio of three.

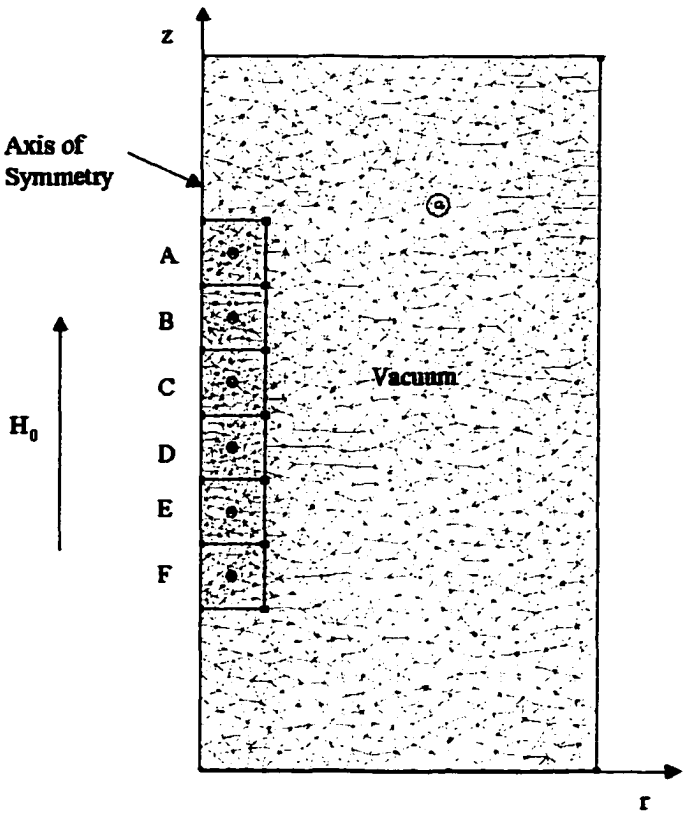

Figure 5.5 Finite element model of AMR bed using six sections with specified temperatures.

The modeled bed is broken into six sections, A-F, where the M versus H characteristics can be arbitrarily specified. Magnetization data for Gd as a function of applied field and temperature was taken from [36] and a routine was written to interpolate the data for an arbitrary field and temperature. The magnetization curves as a function of field at a constant temperature were then used to specify the section properties in the model. The different configurations studied are given in Table 5-1. In the first case, a Gd AMR at a uniform temperature of 270 K is modeled, thereby forcing each section to have similar constitutive relations for M(H). In Case 2, the temperatures are set to simulate an AMR with a temperature span from 310 to 270 K. Finally in Case 3, a layered bed composed of two materials is simulated. Sections A to D are for the first material

while the last two sections represent a second material operating above and slightly below the Curie temperature.

Table 5-1. Temperatures used to set the magnetization as a function of field for each section.

Section	Case 1	Case 2	Case 3
A	270 K	310 K	300 K
B	270 K	300 K	290 K
C	270 K	290 K	280 K
D	270 K	280 K	270 K
E	270 K	270 K	310 K
F	270 K	270 K	290 K

The effect of demagnetizing fields is to alter the field seen by the internal moments as compared to the applied field, H_0. In each simulation, the local field, H_i, is determined along the center of the AMR for a set applied field and this data are written to a file. The local field at the center of each section is then used to determine the local magnetization, M'. The magnetization is also calculated assuming there are no demagnetizing effects i.e. using the applied field. The ratio of these two values is defined as the relative magnetization as follows,

$$\frac{M'}{M} = \frac{M(H_i)}{M(H_0)}. \tag{5.47}$$

If there are no demagnetizing effects, the relative magnetization is equal to 1.

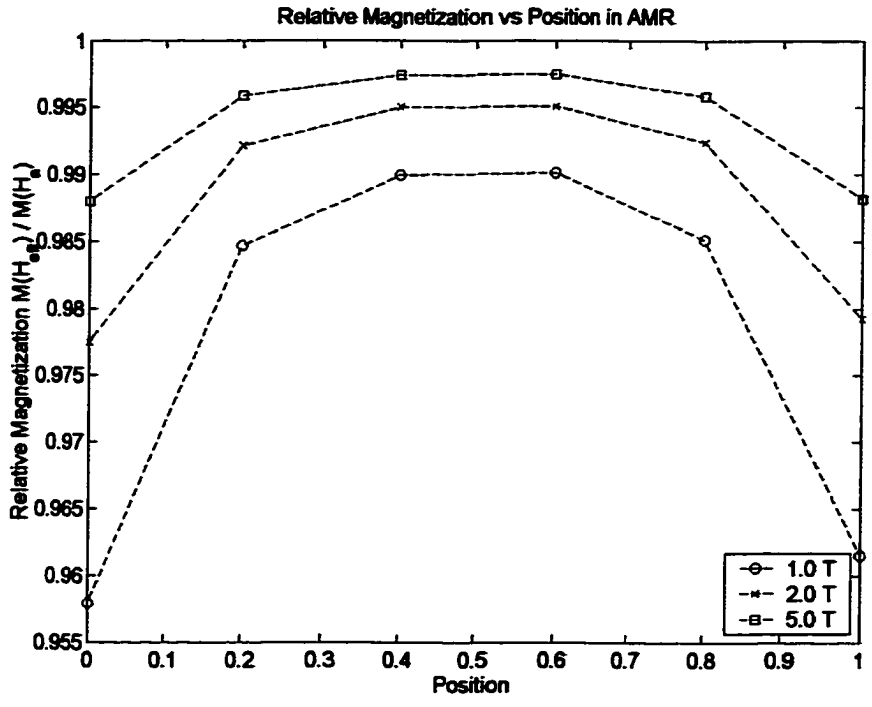

Figure 5.6 Relative magnetization versus position for a Gd AMR with a uniform temperature of 270 K and various applied fields (Case 1.)

The results for Case 1 are shown in Figure 5.6 where the relative magnetizations at the section centers are plotted. In this case, the demagnetizing field effects are small and symmetric. As one would expect, as the field is increased the relative magnetization approaches 1 due to the ferromagnetic behaviour exhibited at this temperature. For sufficiently large field strengths, the susceptibility of a ferromagnetic material becomes small and, hence, the magnetization is a weak function of field. The demagnetizing fields then have little effect on the magnetization. For these conditions, increasing the aspect ratio of the bed will decrease the demagnetizing field.

Figure 5.7 shows the relative magnetization for a Gd AMR with the temperature profile listed as Case 2. Here, the effects of demagnetizing fields are significant even at applied fields as high as 5 T. Again, as the applied field is increased, the relative magnetization approaches one; however, the hot end of the bed has a relative magnetization that is significantly higher than 1 even for an applied field of 5 T.

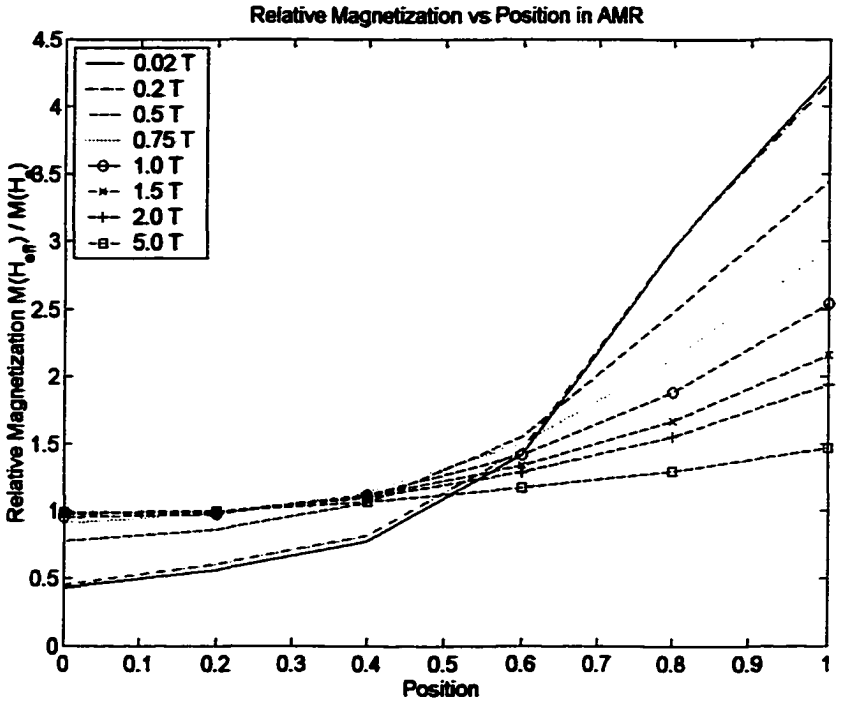

Figure 5.7 Relative magnetization versus position for a Gd AMR with an arbitrary temperature distribution and various applied fields (Case 2.)

What are the implications of these results? Clearly, because the local magnetic work in the AMR is proportional to the change in magnetization, demagnetizing fields will influence the energy and entropy flows in the regenerator. The strong impact of demagnetization shown in Figure 5.7, particularly for low fields (B < 2 T,) suggests that a solution of the magnetostatic problem is necessary for accurate modeling. For the Case 2 situation, the application and removal of the field will have temporal and spatial impacts when H_a is applied over some finite time. In terms of magnetocaloric effect, demagnetizing effects distort the actual MCE as a function of temperature. In Case 2, the MCE on the hot end will be larger than expected.

As a final example, a hypothetical two-material layered AMR was simulated with Case 3. It is assumed that the second material has magnetization isotherms equivalent to Gd. The specified temperature profile simulates a "warm" material predominantly operating at temperatures less than the Curie temperature, and a "cold" material operating around its Curie temperature. The "warm" material comprises the sections A-D and the cold material occupies sections E and F.

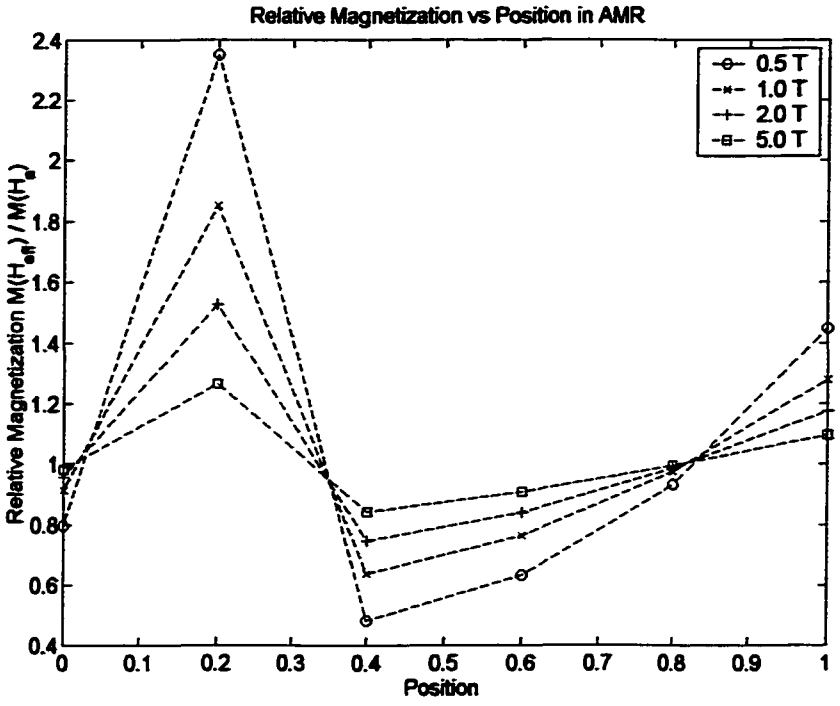

Figure 5.8 Relative magnetization versus position for a Gd AMR with an arbitrary temperature distribution and various applied fields (Case 3.)

The relative magnetization results for Case 3 are again non-intuitive; however, some trends are evident. Material that is at temperatures greater than the Curie point shows the largest response to demagnetizing fields and higher applied fields tend to reduce these effects. The large impact on the "cold" material, which is predominantly paramagnetic in behaviour, is a cause for concern. Entropy generation is proportional to the slope of the MCE as a function of temperature (see Chapter 2) and the interface between the two materials is an obvious location where a discontinuity in MCE could exist. The demagnetizing field could make this worse. Thus, entropy generation at a material interface is something that should be investigated in more detail.

Chapter 6
Experimental Results

This chapter describes initial experiments with the AMR Test Apparatus. Three Gd AMRs are tested, each of a different aspect ratio and refrigerant mass. The impacts of field-flow phasing are investigated revealing a strong influence of phase advance on temperature span. Characteristics of the AMR performance are discussed and related to apparatus design.

6.1 Introduction

The AMR Test Apparatus is designed to be able to test beds at temperatures from 300 K to 20 K. The hot heat sink can be a fluid such as water (for room temperature tests), liquid nitrogen (for tests below 77 K) or some intermediate fluid for testing of AMRs below room temperature and above liquid nitrogen. Initial experiments were performed using Gd AMRs with the hot heat sink maintained with water. The nominal flux density for the majority of tests was 2 T with some additional testing at 1.75 and 2.25 Tesla. The primary variables being measured were the fluid temperatures immediately before and after each AMR bed. Table 6-1 lists the independent parameters used in the test with their associated ranges.

Table 6-1. Independent experimental variables with their ranges.

Variable	Range
He Pressure (atm)	4 - 8
Total Displacer Stroke (cm)	12 - 24
Displacer Offset (degrees)	-30 – 60
Frequency (Hz)	0.2 – 1.0
Gd Mass per AMR (g)	63 – 188
Flux Density (Tesla)	1.75 – 2.25
Φ_{ref}, (utilization)	$13 - 74 \times 10^{-3}$

Using a peak heat capacity for Gd of 380 J/kg-K and the ranges for the parameters listed in Table 6-1 allows a reference value for the dimensionless parameter Φ to be determined. The actual range of utilizations investigated is also listed in Table 6-1.

6.2 Gd Test Results

6.2.1 One Section AMR

The first experimental runs were performed with Gd AMRs with a diameter to length ratio equal to one. The mass of refrigerant in each regenerator totaled approximately 63 g and was made up of spherical particles with diameters in the range $212 > d_p > 180$ microns. Fabrication of the regenerators is described in more detail in Chapter 4. Once the apparatus was proven to be operating correctly the regenerators were increased in size. Aspect ratios of two and three with refrigerant masses of 125 g and 188 g respectively were tested. An example of the AMR performance using 63 g Gd AMRs (total mass 125 g) is shown in Figure 6.1:

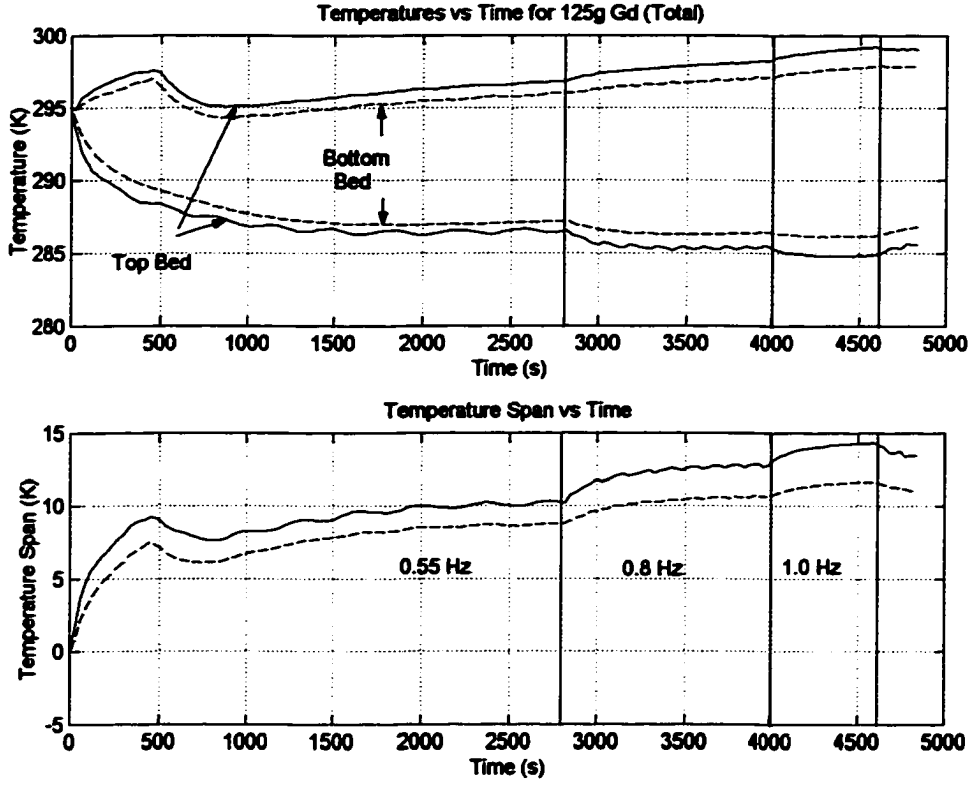

Figure 6.1 Test results for 63 g Gd AMRs with no load, B = 2 T and an operating pressure of 6.5 atm. Operating frequencies of 0.55, 0.8 and 1.0 Hz are shown.

The plot in the top of Figure 6.1 shows the temperatures on the hot and cold ends of the regenerators. The solid line shows the temperatures for the bed at the top of the cylinder while the dotted line is for the bottom regenerator. At the start of the run, the PRTs are at approximately

295 K. Initially, the hot temperatures rise and the cold ends drop sharply. This is because the cooling water flow is off. Once the water flow is turned on, the hot temperatures drop back to near 295 K. The hot temperature continues to rise because the cooling water flow is insufficient to regulate the hot end temperature completely. The plot at the bottom of Figure 6.1 shows the temperature span for the two beds; this is calculated simply as the difference between the hot and cold end temperatures. The solid vertical lines in the plots show where the operating frequency has been changed. The test starts at a frequency of 0.55 Hz and ends at 1.0 Hz.

A number of interesting points can be observed for the test. First, a temperature span of approximately 10 K is generated using a field of 2 Tesla. For a very pure sample of Gd at 295 K, experimental measurements of the magnetocaloric effect with the same field strength give a value of approximately 5.6 K. Clearly, the beds are acting as regenerators. Another characteristic that can be seen is that the top bed shows a significantly higher temperature span ($\Delta T_t = T_{Ht} - T_{Ct}$) than the bottom bed for all frequencies. The hot temperature, T_{Hb}, is lower for the bottom bed and the cold temperature, T_{Cb}, is higher. It can be seen that the smaller temperature span for the bottom bed is not simply due to a different T_H. As the test progresses the system approaches steady-state and then the frequency is increased. There are points where T_{Hb} is the same as T_{Ht} at some previous time; however, the lower temperature span for the bottom bed still exists.

6.2.2 Temperature Span Anomaly

One explanation for the different temperature spans produced by the two beds is that the lower bed sees a smaller effective field change than the top bed. It is hypothesized that there are two ways this could occur: (1) the position of the solenoid is offset with respect to the cylinder zero position; or, (2) the applied field is modified by the presence of magnetic material. The first item is considered an unlikely cause because the apparatus was set-up with this is mind. Instead, the second condition is more likely to be the root cause. Although care was taken during the apparatus design to minimize the amount of ferromagnetic material this could not be completely avoided due to component availability and cost. Furthermore, the distortion of the field due to other magnetic materials is more significant when the applied field strength is low. Most ferromagnetic materials magnetically saturate at flux densities less than or near 2 T. If the applied field were to be high (i.e. 5 – 7 Tesla), the effects of magnetic components on total field would be less significant. Regardless, the apparatus has been designed such that the position of the solenoid can be adjusted with respect to the cylinder. In future tests, adjusting the magnet position should

reduce the temperature span difference between the top and bottom beds if field distortion is in fact the cause.

Another factor that may be involved is a lack of symmetry in the system due to the two beds operating somewhat independently. This is explained as follows: the two AMR beds are thermally coupled by the flow of the heat transfer fluid through the cold section of the cylinder (or a cold heat exchanger plus connecting lines); in this apparatus the gas flow is simple harmonic. If the mass flux is large, a gas particle will pass completely through the first regenerator, the cold section and the second regenerator. In the opposite extreme, if the amplitude of the flow wave is small, some of the gas in the cold section will never leave that space – this condition can be considered one of weak coupling between the two AMRs. In terms of the governing equations describing the AMR system, the parameter Φ can be used as a metric for the degree of coupling between the two beds. For a fixed geometry and bed size, as Φ increases so does the coupling.

The parameter Φ now has additional importance. Not only does Φ have a large impact on the fluid-solid interaction in an AMR bed, it can also characterize the interaction between two AMR beds for a given geometry. If we imagine the fluid at the beginning of a cycle, we can identify a surface at the end of one regenerator. As the blow progresses this interface moves with the fluid and for a sufficiently long blow, the interface will move through the cold section to coincide with the cold face of the other AMR bed. At this point, thermal information from the first bed has been convected to the second bed. If a temperature gradient exists through the cold section then the coupling will depend on the total energy flux i.e. the convection and diffusion components together. We will assume that the diffusion component is negligible and define a reference value for the regenerator coupling as follows:

$$\Phi_0 = \frac{V_C \rho_C c_p}{M_b c_B}. \tag{6.1}$$

Φ_0 is simply the ratio of the thermal mass contained in the cold volume to the thermal mass of the AMR. The mass in the cold section is the density of the fluid, ρ_C, times the volume of the cold section, V_C. The mass of the AMR is M_b. A coupling parameter, K, can now be defined as the ratio of the thermal mass flux for a given blow period to the thermal mass contained in the cold volume. In terms of the parameter Φ, this becomes,

$$K \equiv \frac{\overline{\Phi}}{\Phi_0}, \tag{6.2}$$

where $\overline{\Phi}$ is defined as,

$$\overline{\Phi} = \frac{c_p}{M_b c_B} \int_0^{\tau_2} \dot{m}(t)dt. \tag{6.3}$$

K, the coupling parameter, can be thought of as the ratio of the total capacity flux for half of the cycle to the flux required to move the imaginary interface through the cold section, Φ_0 (one end of a regenerator to the other.)

In the AMRTA the integral in Equation (6.3) is determined by the swept volume in the fluid displacer which is a function of the cross-sectional area, A_d, the total stroke, S_T, and the fluid density in the displacer ρ_d. Thus, the coupling parameter can be written as follows,

$$K = \frac{\overline{\Phi}}{\Phi_0} = \frac{S_T A_d \rho_d}{V_C \rho_C}. \tag{6.4}$$

The condition where $K = 1$ is when the thermal information from the end of one regenerator is convected to the end of the other.

The question arises as to how large is the coupling in the experiments? If we assume the fluid is an ideal gas and the pressure is constant throughout the flow circuit, the coupling parameter can be rewritten as,

$$K = S_T C_g \frac{T_C}{T_d}. \tag{6.5}$$

In Equation (6.5) the area and volume information have been replaced with a coefficient describing the geometry, C_g, and the ratio between the temperature in the cold section, T_C, and the temperature in the displacer, T_d, replaces the density.

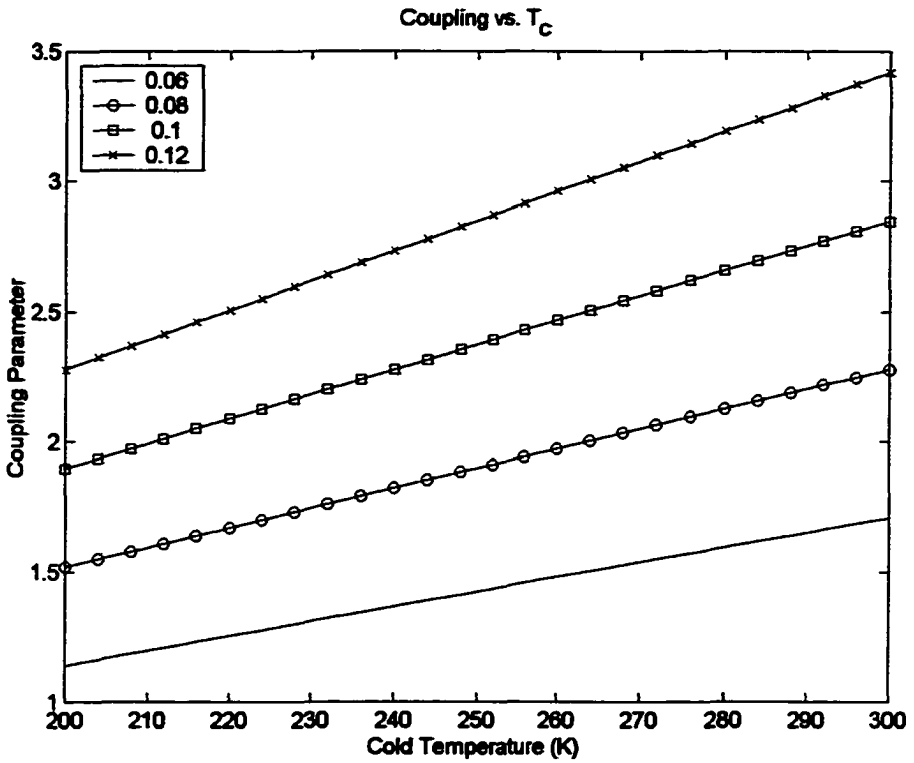

Figure 6.2 The dependence of coupling, K, between the AMR beds as a function of temperature. Various displacer strokes are shown in metres. (These values are half of the total stroke.)

Figure 6.2 shows the coupling (K) between the two regenerators as a function of temperature in the cold section. The displacer temperature is assumed 300 K. The strokes are equivalent to the amplitude of the displacer waveform and, thus, are half of the total stroke. For the AMRTA the geometric coefficient, C_g, is 14.24 m^{-1}. For the experiments reported herein, the minimum cold temperature reached is 279 K; thus, the coupling between the beds exceeds 1.5 for all tests. This lends further evidence that distortion of the magnetic field is the cause of the temperature span anomaly; however, this is still not clear. The thermal coupling between the regenerators should be thought of as a combination of large K and large utilization, Φ. The former accounts for the device geometry whereas the second parameter indicates the strength of the fluid thermal disturbance relative to the regenerator thermal mass.

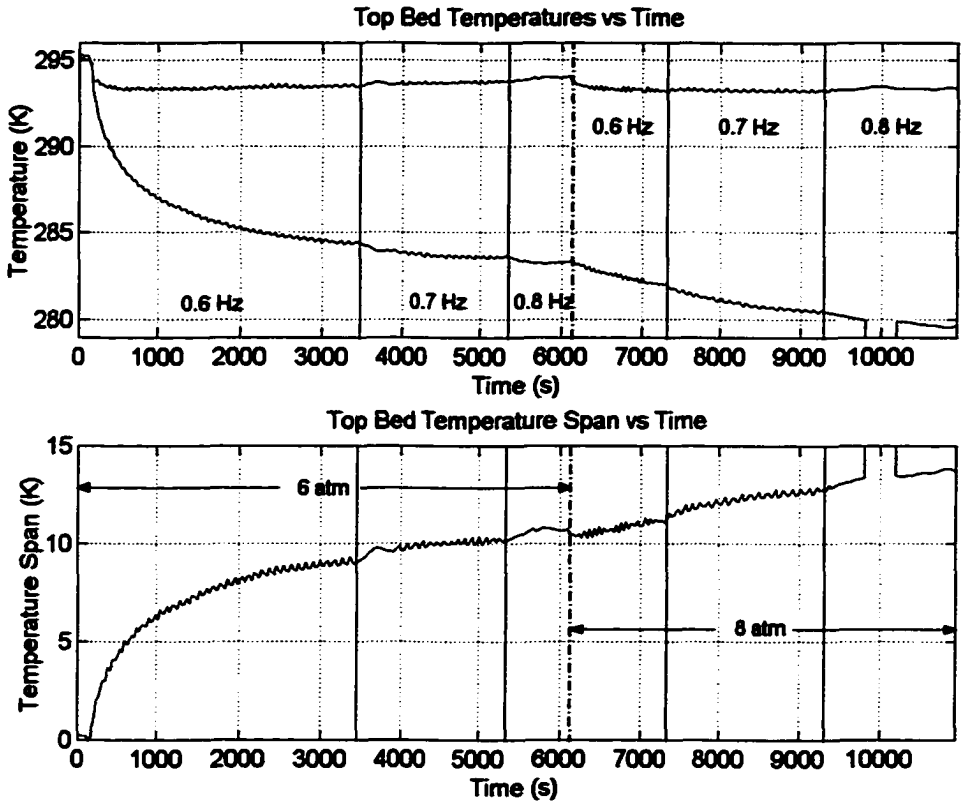

Figure 6.3 Test results for 125 g Gd AMR with no load and B = 2 T (top bed only). Cooling water flow is on full maintaining a relatively constant hot end temperature.

6.2.3 Two Section AMR

By adding more material to the AMRs and doubling the aspect ratio to two, a bed with mass of approximately 125 g is created. An experiment with 125 g Gd AMRs is shown in Figure 6.3. Unlike the previous experiment, the cooling water flow is fully on in this test and the hot temperature is held nearly constant near 294 K.

A number of different operating conditions are shown in Figure 6.3. It should be noted that the discontinuity in T_C near 10 Ksec is due to a temporary loss of the sensor signal. Initially, the AMR is pressurized to 6 atm and is run at 0.6 Hz. As the test progresses, the frequency is increased to 0.7 Hz and then 0.8 Hz. The pressure is then boosted to 8 atm and the frequency is again cycled from 0.6 to 0.8 Hz. Throughout the run the hot temperature remains fairly constant as the frequency is varied. When the pressure is increased to 8 atm a slight decrease in T_H can be noted; this has increased the fluid density and resulted in better heat transfer coefficient in the heat exchanger. Unlike the previous test shown in Figure 6.1 where T_H was not well constrained,

it is clear that an increase in frequency has increased the cooling power leading to a lower T_C. A similar response is noted for the increase in operating pressure. For a constant displacer stroke an increase in operating pressure leads to an increase in the mass flux. For the operating conditions in Figure 6.3, Φ is on the order of 0.04 and the fluid thermal mass is small relative to the refrigerant's; thus, increasing the mass flux has a positive impact on the temperature span in that the cooling power is increased. For these conditions, parasitic heat leaks limit the temperature span.

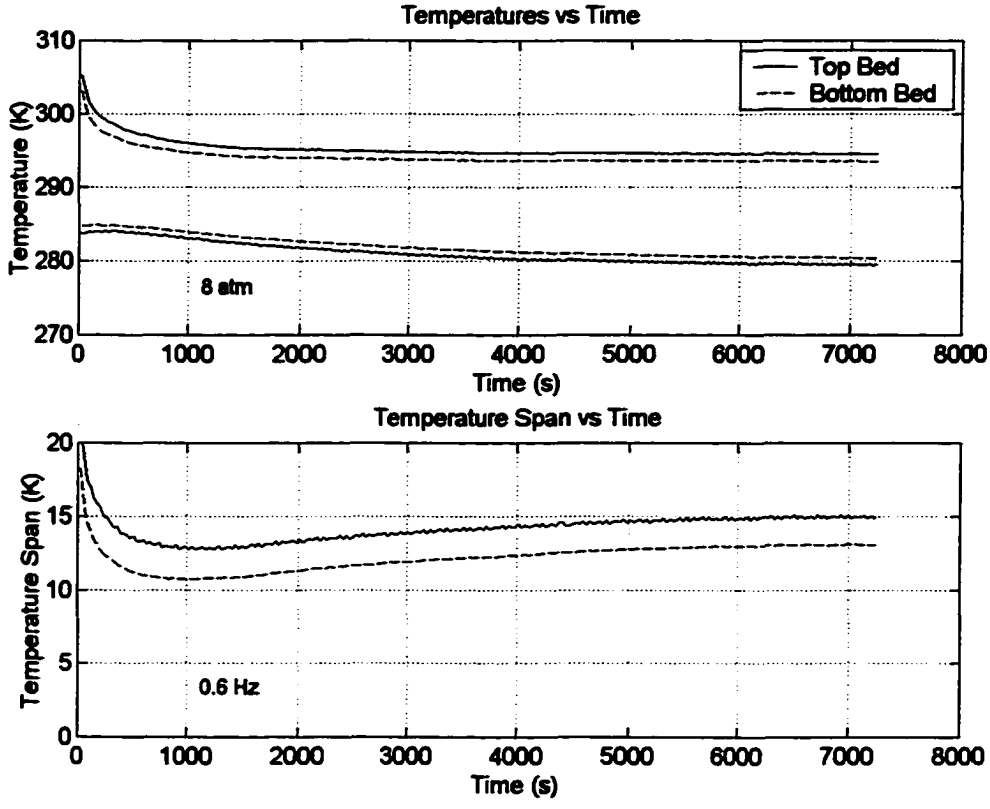

Figure 6.4 Experimental results for 188 g Gd AMRs with B = 2 T and zero loading. Operating pressure is 8 atm and the frequency is fixed at 0.6 Hz.

6.2.4 Three Section AMR

At the time of writing the largest aspect ratio tested is three and is for a 188 g Gd AMR. Figures 6.4 and 6.5 show performance data for the 188 g AMRs with various operating conditions. For the run shown in Figure 6.5, the cooling water flow has been restricted to allow T_H to reside above the Curie temperature. In Figure 6.4, the cooling water flow is initially small and then increased. Once the system reaches steady-state T_H is near 294 K and the temperature

span is 15 K for the top bed and 13 K for the bottom bed with an operating pressure of 8 atm and a frequency of 0.6 Hz. For similar operating conditions in Figure 6.5 the temperature span for the top bed is just over 20 K while the bottom bed is approximately 3 K less. During testing, it was found that the greatest temperature spans are generated when T_H is greater than the Curie temperature and T_C is less; this characteristic was found to be true for all three AMRs tested (63 g, 125 g and 188 g.) Also, for all three cases, the lowest absolute temperatures are reached (T_C) when T_H is as low as possible.

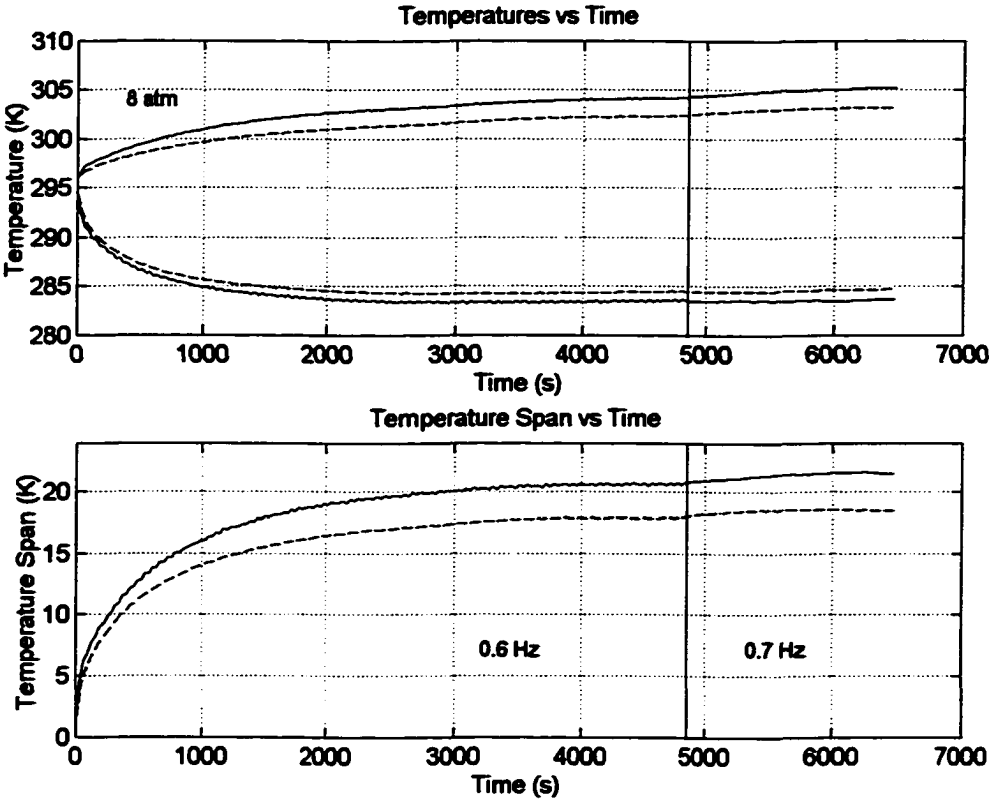

Figure 6.5 Experimental results for 188 g Gd AMRs with B = 2 T and zero loading. Operating pressure is 8 atm and cooling water flow is small.

As expected, the single material AMR displays non-linear operating characteristics in the vicinity of the Curie temperature where an inflection point exists in the temperature dependence of the magnetocaloric effect. With the Gd AMRs tested to date, the AMRTA has produced temperature spans that are comparable to results from other researchers for similar field strengths. However, in this case operating frequencies are more than double other devices in most cases and the temperature spans are generated with refrigerant masses that are nearly ten times smaller.

6.3 Phasing Anomaly

Experiments were performed near the Curie temperature with three different sets of Gd AMRs. Controlling the flow rate of water through the heat exchangers sets the hot heat sink temperature. This allows the heat sink temperature to be varied, but active control is not possible; thus, the heat flux through the regenerator has an effect on T_H. One key operating condition explored is the influence the hot heat sink temperature has on performance, in particular, how performance varies operating above or below the Curie point. As discussed previously, for all regenerators the maximum temperature span is generated when the AMR straddles the Curie temperature.

An unexpected phenomenon observed for all experiments is the strong influence blow phasing has on temperature span. Blow phasing is the angular offset between the cylinder position and the displacer position resulting in a phase difference between the AMR location relative to the magnetic field and the blow waveform. Figure 6.6 graphically shows this.

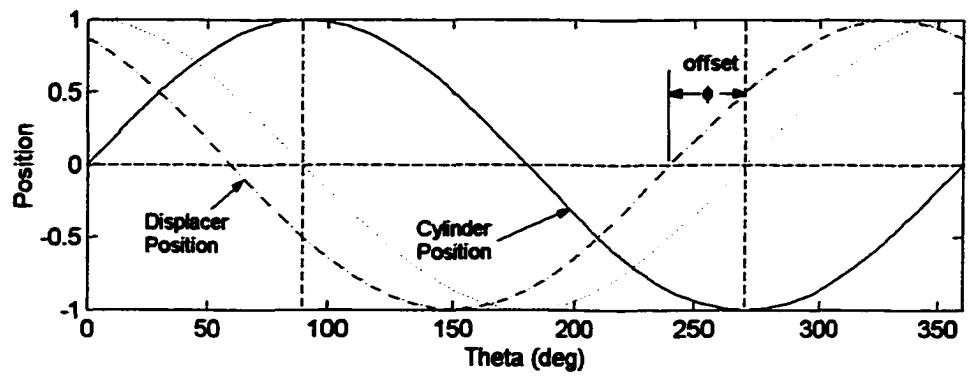

Figure 6.6 Introducing an offset in the phasing between the fluid displacer and the cylinder position advances the blow waveform relative to the magnetic field application.

A positive value for the offset indicates that the blow is advanced in time relative to the cylinder position. With no offset the displacer is shown as being 90 degrees out of phase with the cylinder, so that when the cylinder is at the maximum vertical position (bottom AMR in the high field region) the displacer velocity is maximum with the fluid flow in the negative direction.

The influence of phasing was examined experimentally, twice with the single section AMRs (63 g) and twice with the three section AMRs (188 g.) The first test with a single section bed was at a pressure of 8 atm and a frequency of 0.6 Hz and the second test used a pressure of 4 atm. The tests with the three section AMRs used a pressure of 6 atm and a frequency of 0.7 Hz and 0.6 Hz. For the first three tests T_H is near 294 K while the last test straddles the Curie temperature. These

particular operating conditions were varied to see if the phasing was related to the mass flow rate or temperature span.

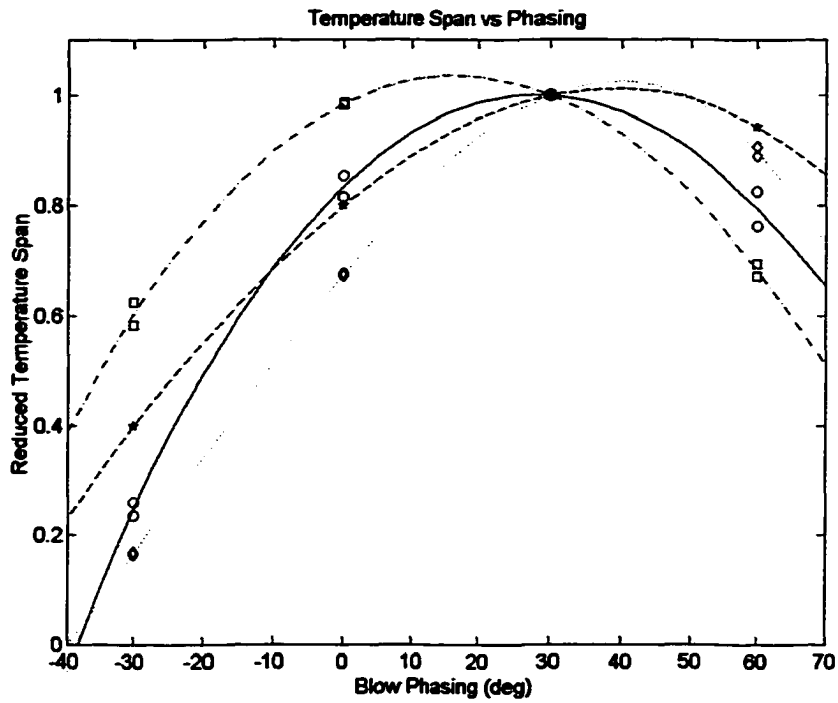

Figure 6.7 The reduced temperature span for four different operating conditions shows a strong dependence on displacer offset. The lines fitting the data points are cubic splines and are a guide to the eye only.

Figure 6.7 shows the reduced temperature spans for the four tests as a function of displacer offset. In each test the absolute temperature spans are normalized by the maximum spans. The temperatures of the bottom and top beds are averaged in order to fit a cubic spline to the data points. In all cases, the maximum temperature span is reached when the blow phase is advanced 30 degrees. The angular settings for the displacer position are limited to 30-degree intervals.

A couple of interesting points can be noted. Not only does phasing have a strong impact on temperature span, but even with the blow advanced as much as 60 degrees the performance is still quite good. This is not observed for a delay in the blow; for all cases, the temperature span is much smaller with the offset at –30 degrees. Another interesting observation is that the tests with the single section regenerators seem to maximize temperature span at lower displacer advances than the three section regenerators. The regenerators with an aspect ratio of three (188 g) appear to maximize temperature span with the blow phasing near 45 degrees according to the spline fits,

and are near their maximums at 60 degrees. These two tests also have the highest absolute temperature spans.

Field-flow phasing is an important phenomenon to understand for device design. For some AMR geometries, like a wheel concept, the manifold locations essentially fix the phasing. If this is done incorrectly, the above results suggest device performance could be impaired.

This phenomenon needs to be investigated more rigorously to clearly understand what is happening; however, a possible cause has already been discussed in Chapter 5. For the experiments reported here, the nominal applied flux density is 2 Tesla and, for the temperatures under consideration, the magnetization of Gd is as high as 1.4 Tesla. The effects of demagnetization fields are geometry and magnetization dependent; thus, given that the magnetization is a strong function of temperature, the effects of demagnetization fields could be causing the observed phasing anomaly. Further experiments should help clarify this if the temperature symmetry of the beds can be established by adjusting the cylinder position with respect to magnetic field peak.

6.4 Entropy Balance

Chapter 2 derives an expression describing the ideal magnetocaloric effect as a function of temperature, balance and regenerator symmetry. The equation is a result of assuming zero entropy generation in the AMR and, therefore, an entropy balance exists under periodic steady-state conditions. Cross *et al.* [21] derived the first expression describing the ideal adiabatic temperature change for the case of a balanced and symmetric AMR resulting in an expression of the following form,

$$\Delta T_{ad}^{ideal}(T) = \frac{T}{T_{ref}} \Delta T_{ref}. \tag{6.6}$$

This equation states the ideal magnetocaloric effect should be a linearly increasing function of temperature. This expression is a result of an entropy balance and, if correct, implies that if the magnetocaloric effect at the cold end of the AMR exceeds that at the hot end, the second law of thermodynamics will be defied. There are no previously reported experimental results for such an operating condition. With this in mind, experiments were performed with the AMRTA to see how a Gd AMR operates with T_C approaching the Curie point.

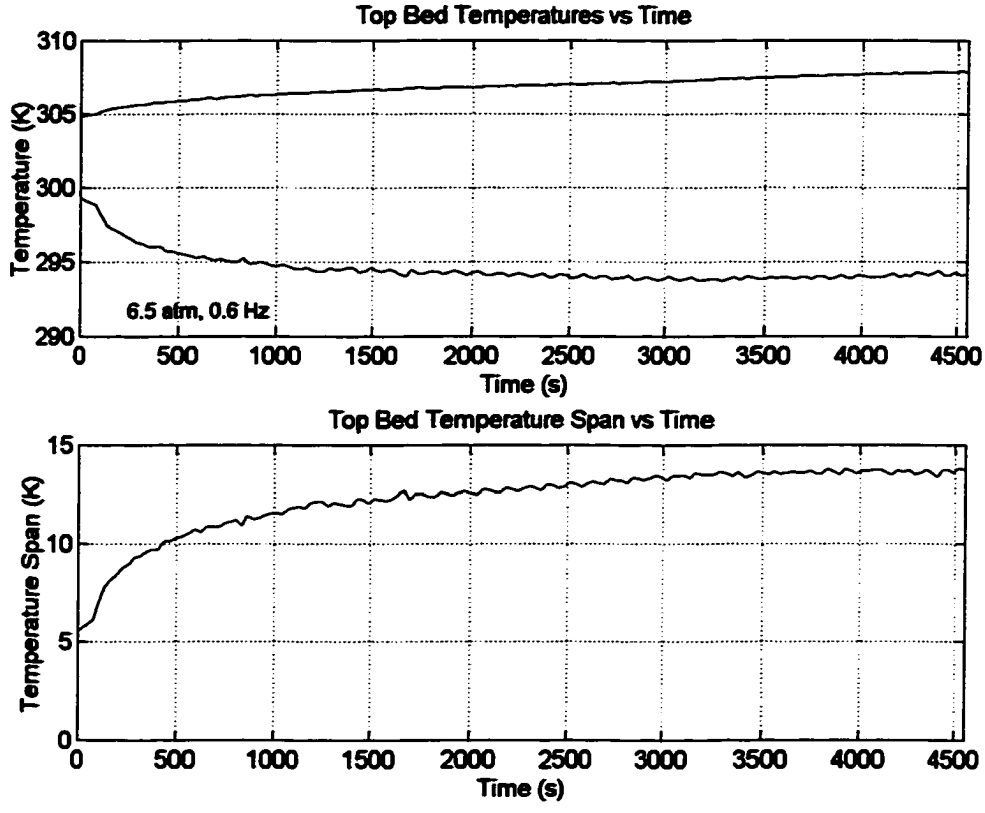

Figure 6.8 Gd AMR operation above the Curie temperature.

Figure 6.8 is a plot of experimental data for a 188 g Gd AMR operating near or above the Curie temperature (approximately 295 K.) T_H shows a small upward drift over time due to the inability to provide active temperature control to the hot heat sink. In general, the AMR behaves in a similar manner to other experiments where the temperatures are below or straddling the Curie temperature. The interesting feature of this test is difference between the MCE at the hot end and the cold end of the regenerator; the MCE at the cold end is greater than that at T_H. This operating state defies the second law if Equation (6.6) is true. The magnetocaloric effect at T_C and T_H for Gd with a 0-2 T field change have been plotted in Figure 6.9 using the data of Dan'kov *et al.* [36]. The actual MCE curve of the material used in the experiments most likely has an MCE peak occurring at a temperature less than 295 K. The Curie temperature for Gd depends on material purity, and is often reported to be in the range of 292–295 K.

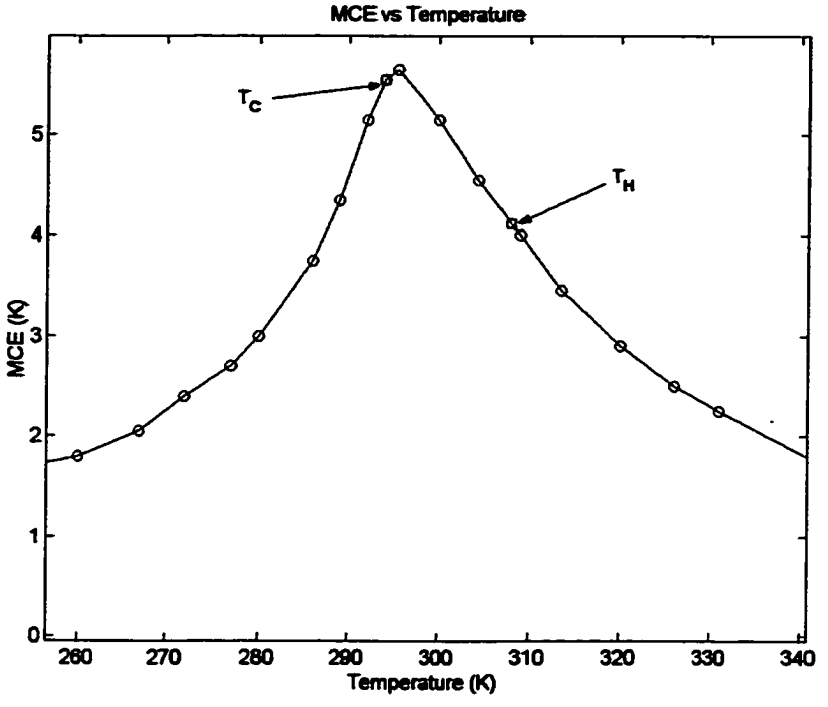

Figure 6.9 The locations of T_C and T_H on the MCE versus temperature curve for the test shown in Figure 6.8.

Although it is difficult to make a definite statement that this is a stable operating regime (because T_H is slowly rising,) the fact that T_C decreases initially suggests that there is a net flux of entropy from the cold end to the hot end. This may not be a preferred operating point for an AMR, but it is useful regime to examine for comparisons to analytical and numerical models. There is certainly more that can be learned and further experiments are warranted. As discussed earlier, understanding AMR behavior in this situation with a single material should also lead to further insights of how a layered AMR needs to be designed for a desired cooling power and temperature span.

Chapter 7
Numerical Results

At best, a numerical model is a predictive tool; however, the validity of any model depends on two key features: (1) the mathematical representation of the problem accurately captures the underlying physics; and, (2) the numerical model uses a proven algorithm giving solutions that match analytic results. Patankar [66] divides practical problems into two groups, A or B, differentiated by whether the problem satisfies feature (1), A, or not, B. Group A problems tend to be those producing accurate results and, thus, good predictability. Group B problems are those that may still require experimentation to solve. At this stage of development, models of Active Magnetic Regenerators can not be assigned to group A for one main reason: there has never been a validated model reported in the literature. Some of the reasons for this are discussed in Chapter 1. This chapter will present results of the model developed in Chapter 5 and compare some of the numerical results to experimental data to provide partial validation. The model is then used in a predictive manner to examine the impacts of various parameters and the performance of two material, layered AMRs.

7.1 Model Validation

A large number of independent parameters are needed to completely characterize an AMR. Results presented here are for second-order magnetic materials assumed to display property variations similar to Gd in the 0-2 Tesla range (see Chapter 5.) Helium is assumed to behave as an ideal gas with appropriate relations to describe the temperature dependent thermal conductivity, viscosity and heat transfer coefficient. Table 7-1 lists some relevant parameters.

Table 7-1. Model parameters.

Parameter	Value
Bed Length	75 mm
Bed Diameter	25 mm
Particle Size	200 μm
Bed Porosity	0.38
Peak Field	2 Tesla
Displacer Stroke (total)	20 cm
Displacer Area	13 cm^2
Matrix Conductivity	15 W/m-K

A value for the matrix thermal conductivity (inter-particle) was assumed. This is a difficult parameter to determine without experimentation; however, many studies report values much less than 15 W/m-K (an order of magnitude less in some cases) for spherical particle beds. Of course, this parameter is temperature and geometry dependent. Bulk thermal conductivities for rare earth metals near room temperature are on the order of 15 W/m-K [70] so this value can be used as a worst-case estimate.

The model domain is divided into 109 uniformly spaced grid points with 40 nodes allocated to each regenerator. The cold section uses 19 grid points and each void section uses 5 grid points. A complete cycle is simulated using an increment of 5 degrees (i.e. 72 time steps per cycle.) Unlike other models reported in the literature for time-dependent AMRs, the results described herein model a system with a sinusoidal waveform for applied field and mass flow rate. Other models have assumed step functions for field and flow. In general, due to the strong field and temperature dependency of the refrigerant properties, the accuracy of the model is expected to decrease as the utilization increases. As Φ increases the perturbation of the bed temperature tends to become larger. If the number of time increments is constant then the temporal discretization effectively becomes less accurate in modeling the physical system. A remedy for this is to increase the number of time steps per cycle.

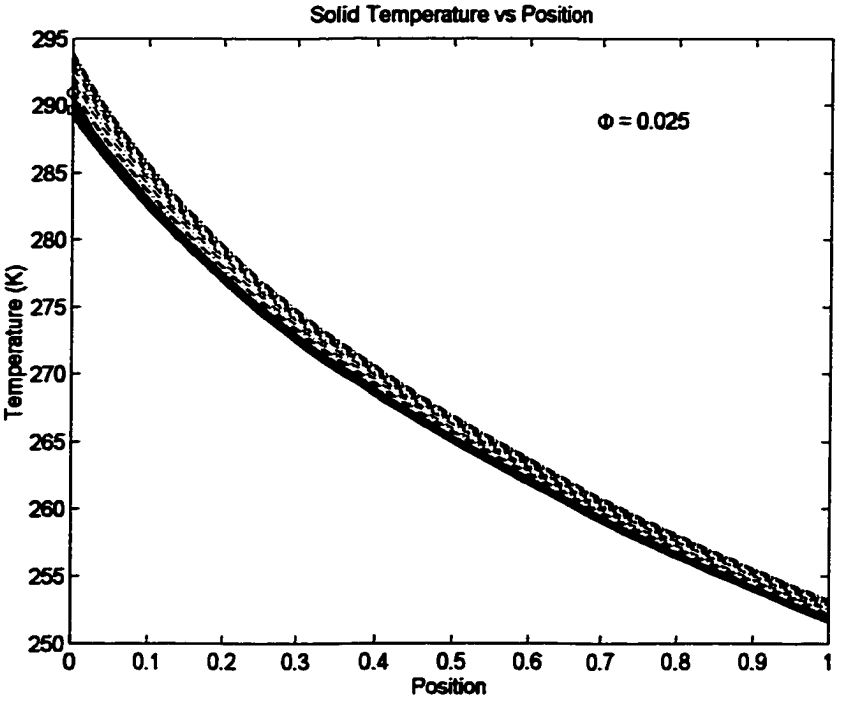

Figure 7.1 Solid temperatures as a function of position. (Solid lines are for the cold blow, dashed lines are for the hot blow.) B_p= 2 T, T_H = 295 K.

7.1.1 Initial Results

The numerical model developed in Chapter 5 was initially run with a pressure of 8 atm, a frequency of 0.7 Hz, a hot heat sink temperature of 295 K and a peak field of 2 Tesla. The resulting envelope of refrigerant temperatures at cyclic steady-state are shown in Figure 7.1. The solid lines are the temperatures during the cold blow (convection from high temperature to low temperature side) and the dashed lines are for the hot blow (mass flow from cold end to hot end of the regenerator.) The applied heat load is zero. Utilization has a strong influence on regenerator performance and a reference value is given in the plot for the particular operating conditions. This value is calculated using Equation (2.5).

A striking observation is the magnitude of the predicted temperature span. The model predicts a zero load T_C of approximately 253 K. Since the lowest temperature reached during the experiments was approximately 279 K, this result suggests that the mathematical model does not capture all of the underlying physics. One of the initial assumptions of the model was that the cylinder would be operating in a vacuum. This condition was not met during the experiments due to an undiscovered leak into the shell. Instead, the cylinder cold section was insulated using 10 mm thick closed-cell neoprene. This reduced, but did not eliminate the heat leak from the environment. Because the cold section comprises the longest section of the cylinder, a relatively small heat transfer coefficient can still lead to a significant rate of heat flux due to the large surface area available.

The model was modified to account for the possibility of parasitic transverse heat leaks through the wall of the cylinder. Assuming the thermal resistance is dominated by the wall and insulation and the thermal conductivity of G-10 (0.6 W/m-K) applies, the heat leak rate can be modeled as a simple diffusion problem in cylindrical co-ordinates. For each section of the cylinder the transverse heat leak is then determined by:

$$Q_t = \frac{2\pi L k_t}{\ln\left(\frac{r_o}{r_i}\right)}(T_f - T_0), \tag{7.1}$$

where Q is the rate of heat transfer, L is the section length, k_t is the transverse thermal conductivity, T_f is the fluid temperature in the cold section, T_0 is the temperature of the environment, r_o is the outer radius of the insulating layer and, r_i is the inner radius at the section location. An estimate of the transverse heat leak using appropriate dimensions an environmental temperature of 295 K and a cold section temperature of 280 K results in a value of approximately 20 W. For these same conditions, an estimate of the axial conduction down the tube walls results

in only 0.25 W. These results highlight the importance of attaining a good vacuum and the potential for increased performance with future experiments.

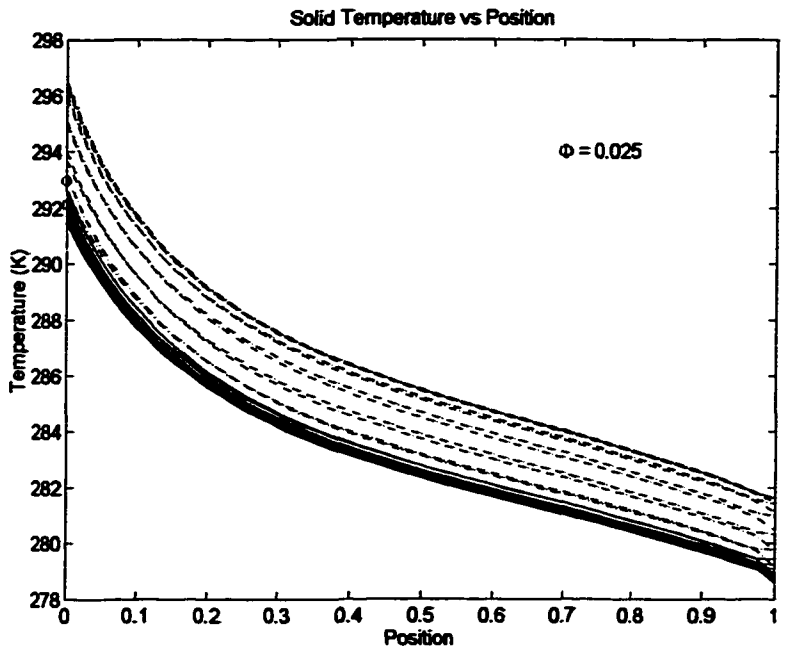

Figure 7.2 Solid temperatures as a function of location in a Gd AMR accounting for transverse parasitic heat leaks. $B_p = 2$ T, $T_H = 295$ K.

Figure 7.2 shows model results with the transverse heat leak included. The temperature span has decreased substantially and is now similar to the experimental results.

To further validate the model predictions, a number of simulations were performed with different frequencies and values of T_H corresponding to selected experimental conditions. Figure 7.3 shows how the model results compare to experimental data. Both plots have similar operating parameters except for frequency and T_H. The top plot shows data for frequencies of 0.2, 0.3 and 0.4 Hz with the hot heat sink nearly constant at 294 K. The bottom plot shows data for 0.6 Hz and 0.7 Hz with the cooling water flow throttled resulting in various T_H's. The low frequency results show that the model predictions are qualitatively similar to the data; however, a significant difference in T_C exists. Lowering the matrix thermal conductivity to 5 W/m-K moves T_C lower and closer to the data trend line. In the bottom plot, the model results compare well to experimental data where the operating frequencies are higher.

As discussed earlier, it is possible that the matrix conductivity is as much as an order of magnitude less than the assumed value of 15 W/m-K or more. In addition, the top plot seems to

confirm that the conductivity should be lower. However, the high frequency comparison seems to give good data using the greater matrix conductivity. The energy flux through the regenerator is made up of a convective term and a diffusive term; the relative importance of the two components is described by Peclet number and temperature gradient. For the temperature spans investigated experimentally and numerically, the temperature gradients are relatively small; thus, the diffusion term is important only when the convection term is sufficiently small. For a fixed displacer stroke and pressure, the convective flux rate is determined by the operating frequency. As the frequency decreases the impact of diffusion becomes more significant. This is reflected in the top plot where there is a discrepancy between model and experiment. As the frequency becomes sufficiently large (and the temperature span remains relatively small), the fact that the matrix conductivity is too large becomes irrelevant since convection dominates the physics. Hence, the good correlation between model and experiment for the high frequency data in the bottom plot. One can conclude that a lower matrix thermal conductivity may be warranted, but qualitative results of the model seem to follow the experimental trends. Furthermore, as the operating frequency is increased, the model predictions match experimental results closely due to the small temperature spans.

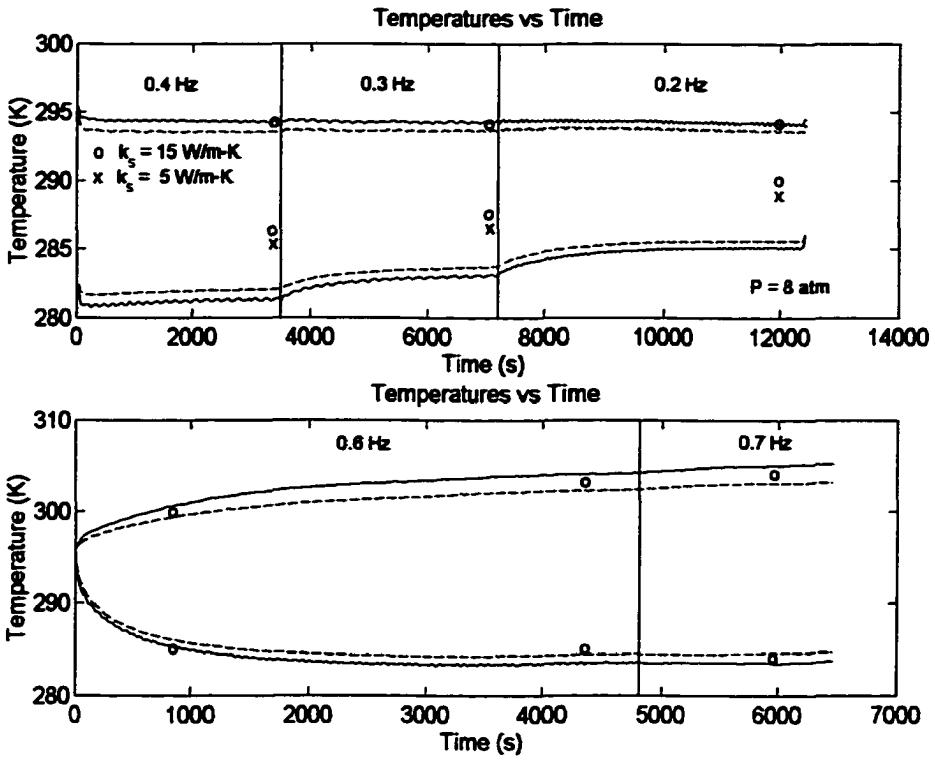

Figure 7.3 A comparison of model results (o, x) to experimental data (-/--). The points locate T_H and the average T_C from the model. Some model results using a matrix conductivity of 5 W/m-K are also given.

7.1.2 Numerical Phasing

One of the unexpected phenomena observed in the experiments was the strong influence flow phasing had on temperature span. The model was created with the ability to arbitrarily set phasing and this parameter was varied to see if the effect could be simulated. Unfortunately, the phasing effect could not be numerically recreated. In fact, a phase advance of 30^0 produced slightly lower temperature spans in most cases. It was initially thought that the applied field was distorted from the profile used in the model and so a new field profile was tried. The new profile assumed the high field region was larger and that the transition to low field occurred more quickly i.e. more of a step-like field application. Again, the phasing effect could not be numerically produced.

Subsequently, the idea of demagnetizing effects was explored (as discussed in Chapter 5.) It is hypothesized that the temporal impacts of demagnetizing fields are the reason for the phasing effect. At this time, the model does not incorporate the magnetic problem and, thus, means that it does not capture all of the relevant physics. Although this undermines confidence in the predictability of the model, it has been shown that there still appears to be some qualitative agreement with experiment. The unfortunate implication of this hypothesis is that the AMR problem must be modeled with at least two spatial dimensions using Maxwell's equations to properly account for demagnetizing effects, making this a numerically intensive problem to solve.

7.2 Single Material Simulations

Regardless of the problems mentioned above the model is a useful tool if we assume the demagnetizing effects are secondary in importance. With this in mind, the model will be used to explore performance characteristics near the phase transition region and with two material beds. It will be assumed that the system is operating in a vacuum and transverse heat leaks are negligible. New insights will be revealed and discussed.

7.2.1 Utilization

The experimental data in Figure 6.8 are interesting because they appear to defy a simple entropy balance. To examine how an AMR would respond with an increasing MCE at the cold end, simulations with T_H much greater than the Curie temperature were performed. Figure 7.4 shows the results for two simulations: one with $T_H = 330$ K (top), and another with $T_H = 305$ K (bottom.) In both cases, the system pressure is set at 8 atm.

As can be seen, the cold ends of the AMRs are at temperatures exceeding the Curie temperature of Gd. With the hot heat sink at 330 K and $\Phi = 0.022$ the temperature profile through

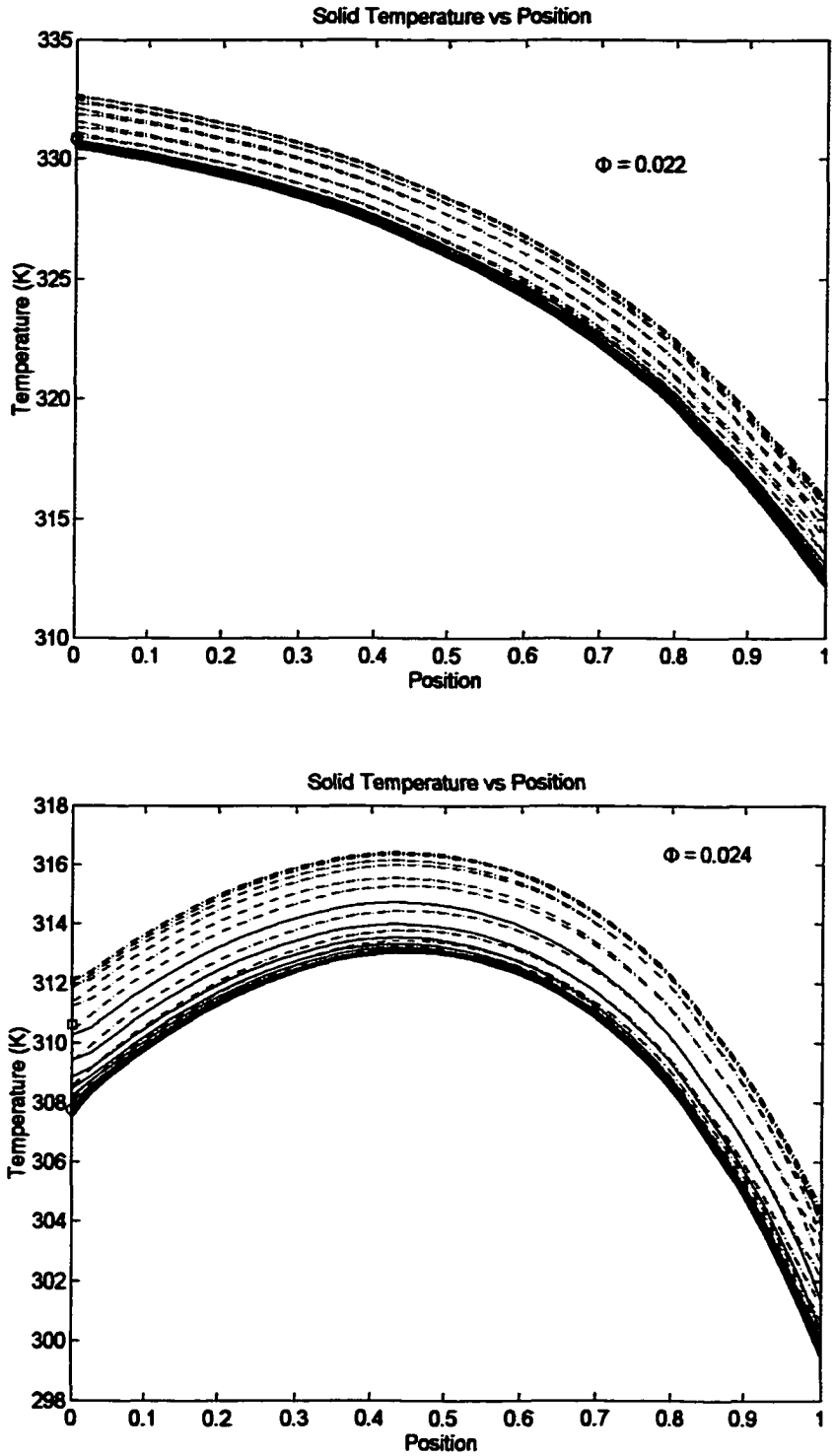

Figure 7.4 Gd AMR response operating above the Curie temperature with P = 8 atm. T_H = 330 K (top), T_H = 305 K (bottom.)

the regenerator is concave. Although the MCE at the cold end is greater than the hot end, the AMR is able to develop a temperature span. The fluid entropy balance through the AMR is satisfied due to thermal conduction and finite heat transfer. In general, for constant N_{TU}, the solid-fluid temperature difference is proportional to spatial temperature gradient. Thus, besides increasing diffusion, the temperature gradient near the cold end increases the solid fluid temperature difference and reduces the net fluid temperature change through the cold section. The net effect is that the ideal MCE condition is violated while the fluid entropy balance is not. (Remember that the ideal MCE derivation in Chapter 2 assumes that the N_{TU} is large so that the solid and fluid temperatures can be considered equal at all locations in the AMR.)

When the hot heat sink temperature is lowered to 305 K, the temperature profiles through the regenerator become more concave and the temperature span is approximately 5 K. This is startling behaviour. It appears as if a barrier on the cold end stops the regenerator from progressing to lower temperatures as the hot heat sink temperature is decreased. If one uses the analogy of a "potential barrier" to describe this behavior then it would be logical to think that a large enough perturbation should drive the cold end over the barrier. In the case of an AMR, the utilization, Φ, can be considered to be the perturbation. If the pressure is increased, so too is the mass flux; this, in turn causes the utilization to increase.

Compared to the situation with the hot heat sink at 330 K, the bottom plot in Figure 7.4 seems to be in a state that would require a smaller perturbation to transit through to a lower temperature. Figure 7.5 shows the resulting temperature span after increasing the pressure by only 2 atm to 10 atm thereby increasing Φ to 0.030. The no load temperature span is now on the order of 50 K.

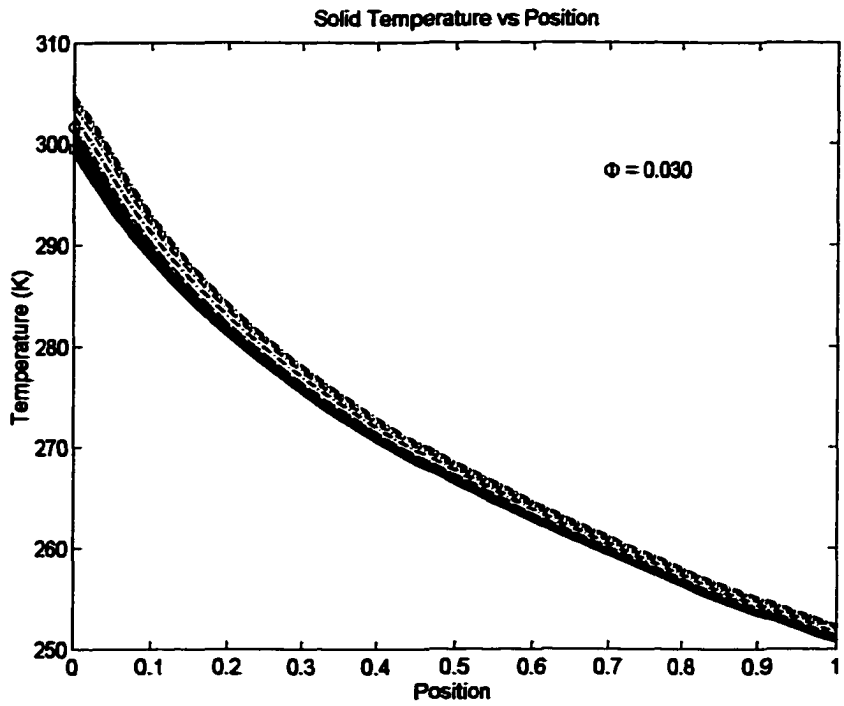

Figure 7.5 No load temperature profiles through a Gd AMR after increasing the pressure from 8 to 10 atm. $T_H = 305$ K.

The mass flow rate in the AMRTA is governed by the stroke of the displacer and the model is made to simulate this. Thus, to produce high mass fluxes it is convenient to adjust the pressure in the model. Clearly, very high pressures are not possible in a real device, but this of no real concern as the pressure is simply a way of simulating different mass fluxes.

Figure 7.6 shows the model results for the case in the top plot of Figure 7.4 after the pressure has been increased from 8 atm to 80 atm. In doing so, the utilization has been increased by a factor of ten and the temperature span is approximately 100 K. An inflection point can also be seen inside the bed near the Curie temperature. It is interesting to note that unlike the previous simulations where the cold blow profiles (solid lines) and hot blow profiles (dashed lines) were somewhat separated, the blow profiles now overlap, covering a similar envelope of temperatures.

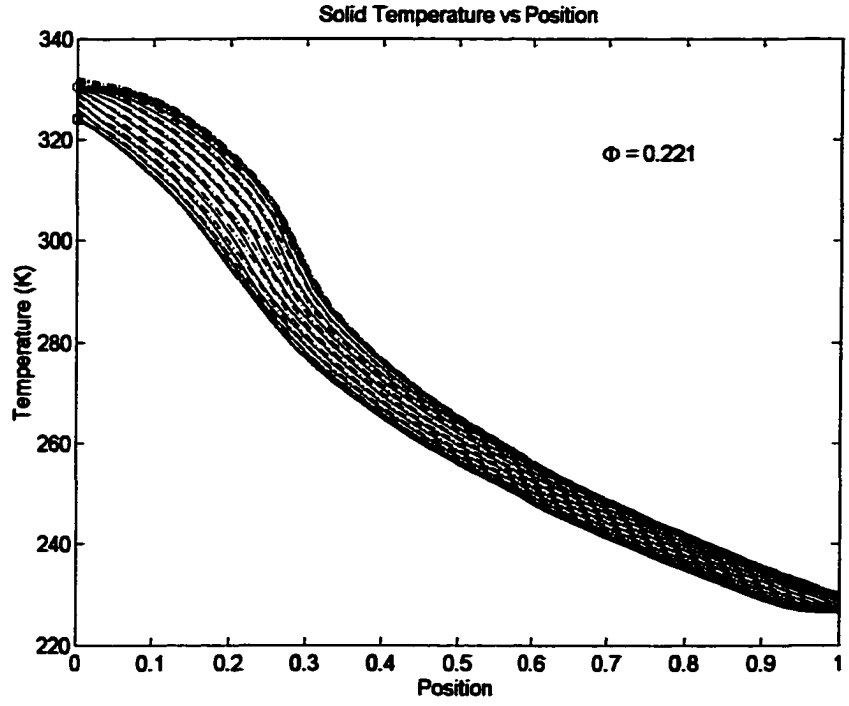

Figure 7.6 No load temperature profiles through a Gd AMR after increasing the pressure from 8 to 80 atm. $T_H = 330$ K.

The evolution of temperature profiles through the Gd AMR with the hot heat sink temperature at 305 K is shown in Figure 7.7. Figure 7.8 plots the temperature span as a function of utilization for the same conditions. Once the utilization is high enough to move T_C through the Curie temperature, the no load temperature span becomes relatively insensitive to Φ for the range of data shown. Model results in [38] for larger utilizations show the temperature span decreasing quickly in a $DyAl_{2.2}$ AMR for utilizations greater than 0.5; however, in that case the utilization was defined using the bed heat capacity at the hot reservoir temperature. Here, the utilization is defined using the zero field peak heat capacity at the phase transition $c_B(T = T_{Curie}, B = 0)$.

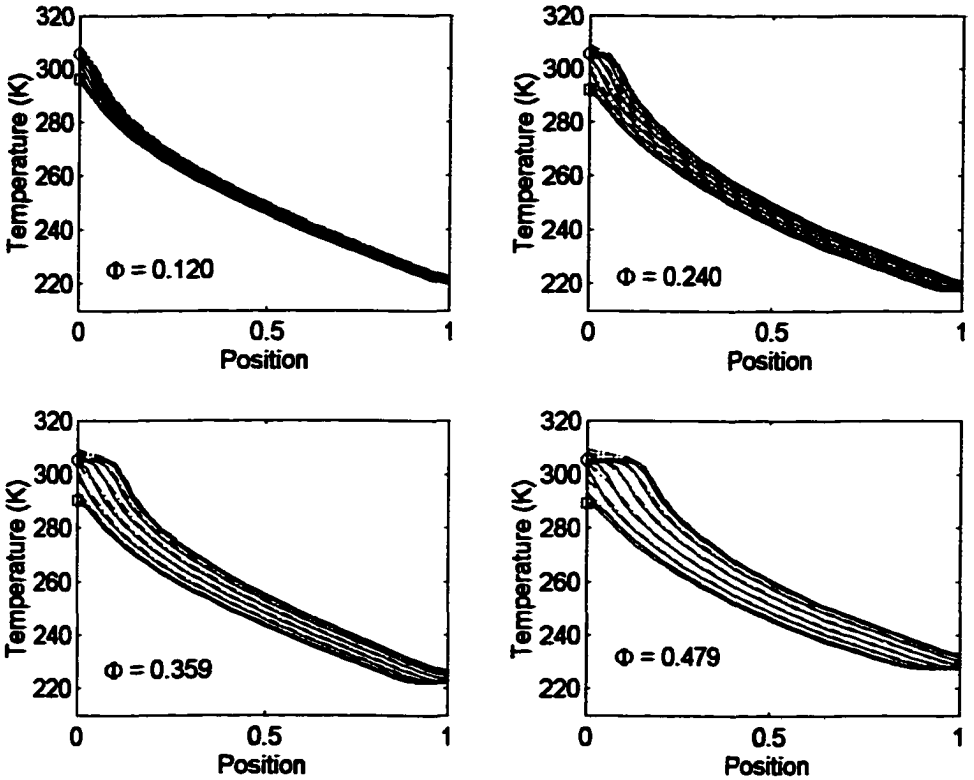

Figure 7.7 No load temperature profiles through a Gd AMR with $T_H = 305$ K and a field change of 0 to 2 Tesla.

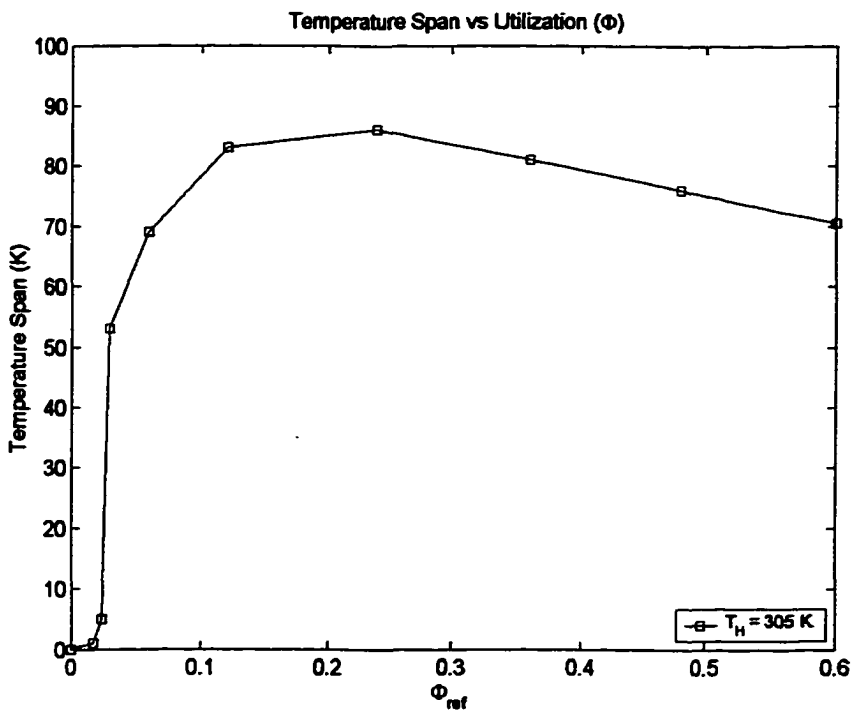

Figure 7.8 No load temperature span as a function of utilization for Gd with $T_H = 305$ K.

The performance of a Gd AMR with various loads is shown in Figure 7.9. The operating parameters are the same as those for Figure 7.8. At low utilizations, the temperature span is reduced significantly as the cooling load is increased. Although the zero load temperature span is decreased at utilizations greater than 0.25, the cold reservoir temperature becomes much less sensitive to loading.

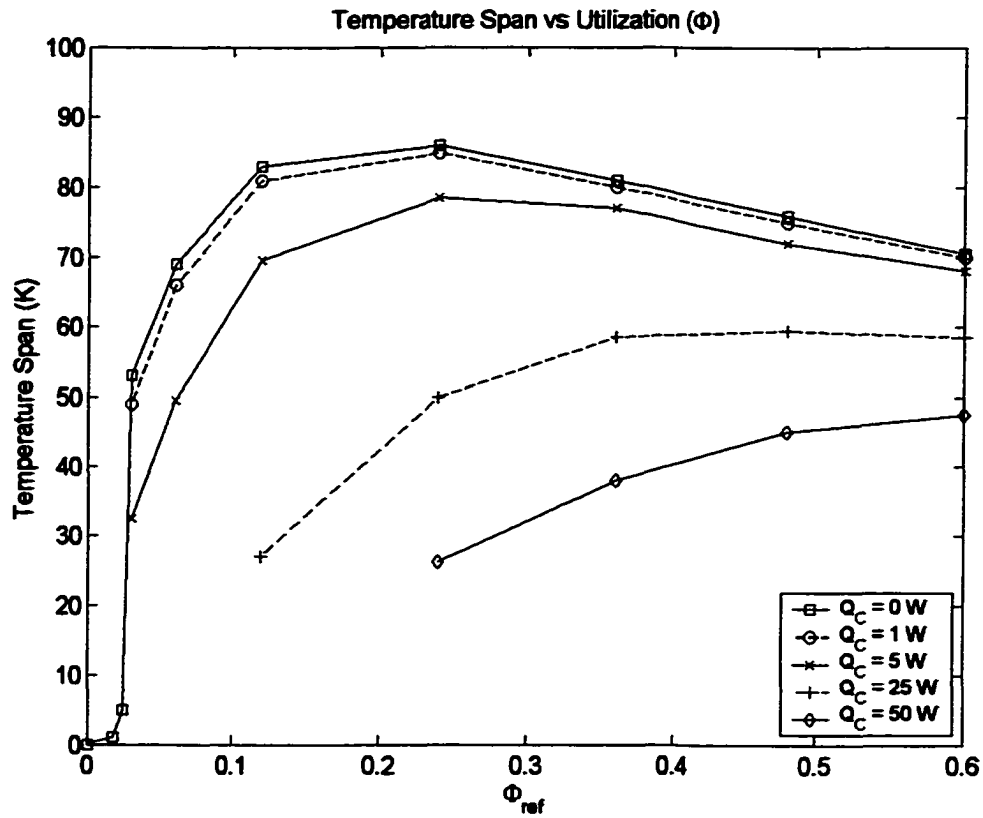

Figure 7.9 Temperature span as a function of utilization for Gd with various loads.

7.2.2 Single Material Characteristics

The simulations of the system using a Gd AMR reveal the following points:

a. the temperature profiles in an AMR tend to be concave when operating above the Curie point and convex when operating below;

b. it is possible to operate an AMR above the phase transition temperature with the MCE on the cold end greater than the hot end when diffusion and finite heat transfer are present;

c. the temperature span produced by an AMR is not a monotonic function of utilization;

d. at low utilizations, the temperature span is very sensitive to a heat load; and,

e. for an AMR operating with $T_H > T_{Curie}$, but sufficiently close to T_{Curie}, the temperature span increases rapidly when some critical value of Φ_{ref} is exceeded.

The last two points are of considerable interest for a layered AMR, since the materials within the AMR will operate around their respective Curie points. A simple entropy balance suggests that the MCE must be an increasing function of temperature and this idea has traditionally guided single material and multi-material AMR design. The above results show that this is not a necessary requirement; however, for a balanced AMR with zero entropy generation, it is. Also, the stipulation "sufficiently close" in point *e* is required because if T_H is far above the Curie temperature then the cold temperature will never be lower than the Curie temperature due to finite heat transfer and diffusion.

The transport of entropy through the AMR is performed by the fluid; hence, the ideal relation for temperature change does not directly describe the solid MCE (the assumption of equal solid and fluid temperatures was implicit.) Thus, even if the MCE function of the refrigerant defies the ideal entropy balance relation, the AMR can still satisfy the second law when finite heat transfer or diffusion is present (as in any real regenerator.) As the single material simulations show, when the AMR is operating where the adiabatic temperature change is a decreasing function of temperature, the temperature profiles are concave. Near the cold end of the bed, the spatial derivative of temperature is large so that with finite N_{TU} a significant difference between solid and fluid temperatures is created. The net change in temperature for the fluid at a particular location is less than the solid and, where the temperature changes rapidly, the difference between solid and fluid increases. When mass flow rate is increased (utilization), the N_{TU} decreases thereby promoting a larger temperature difference between the solid and the fluid. For operation above the Curie temperature, the second law can be satisfied because the net fluid temperature change at the cold end is less than the refrigerant.

The above considerations suggest that the rapid increase in temperature span when T_C is near the Curie point is not just because of increasing utilization; N_{TU} is also important. However, for a fixed regenerator geometry and heat transfer fluid, utilization can be considered an independent variable whereas N_{TU} is a derived parameter. Equation (5.18) also shows that the combination of Φ and N_{TU} governs the strength of the coupling between the solid and fluid. Clearly, further examination of points "d" and "*e*" is warranted.

7.3 Two-material Simulations

The single material AMR simulations revealed that the zero load temperature span is a strong function of utilization when the hot end of the AMR is above the Curie temperature and the cold end of the AMR is above or near the Curie temperature. In this section, modeling results with two materials are used to further explore operation near the transition temperature. Furthermore, the no load performance of some two material AMR beds is examined.

7.3.1 Gd-$Gd_{0.76}Tb_{0.24}$

The use $Gd_{0.76}Tb_{0.24}$ with Gd in a layered AMR is of particular interest because the peak MCE of $Gd_{0.76}Tb_{0.24}$ at 278 K with a field change of 0-2 Tesla is 5.8 K. For the same magnetic field change the peak MCE for Gd is 5.65 K. A bed composed of these two materials defies the MCE scaling suggested by Equation (6.6). Figure 7.10 shows the no load performance for the composite bed with various length fractions of Gd to $Gd_{0.76}Tb_{0.24}$.

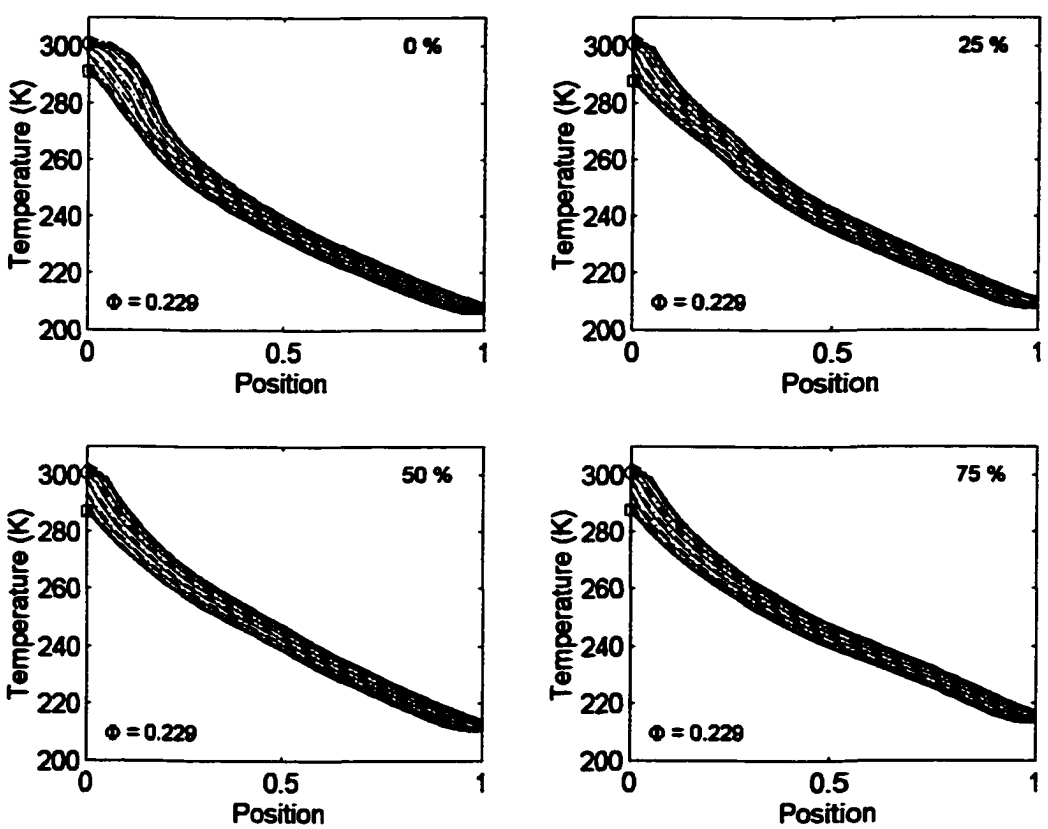

Figure 7.10 No load temperature profiles for two material layered AMRs composed of Gd (hot end) and $Gd_{0.76}Tb_{0.24}$. Four length fractions of Gd are shown (0%, 25%, 50%, 75%.) The utilization is determined using the peak heat capacity of $Gd_{0.76}Tb_{0.24}$ (406 J/kg-K.)

For all of the simulations the pressure of the system is 80 atm, thereby giving a fixed mass flux per cycle. The peak heat capacity of $Gd_{0.76}Tb_{0.24}$ is set at 406 J/kg-K. Four bed compositions are shown: 100% $Gd_{0.76}Tb_{0.24}$ (top left), 25% Gd – 75% $Gd_{0.76}Tb_{0.24}$ (top right), 50% Gd – 50% $Gd_{0.76}Tb_{0.24}$ (bottom left), and 75% Gd – 25% $Gd_{0.76}Tb_{0.24}$ (bottom right.) It is interesting to note that for these conditions the maximum no-load temperature span is produced with the AMR made up of $Gd_{0.76}Tb_{0.24}$ only. It is difficult to see any obvious impact of the layered geometry looking at the temperature profiles other than small irregularities at the interfaces. Although the MCE of $Gd_{0.76}Tb_{0.24}$ is larger than Gd at their respective Curie temperatures, the cold end of the bed passes through the Curie temperature of 278 K.

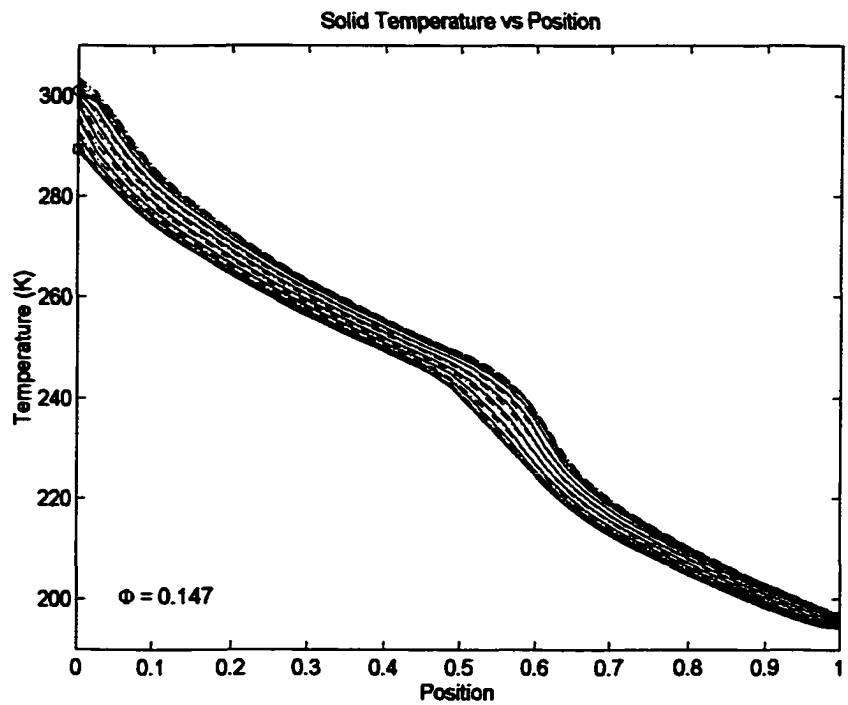

Figure 7.11 No load temperature profile for an AMR composed of 50% Gd and 50% Tb by length.

7.3.2 Gd-Tb

Temperature profiles for a layered AMR composed of 50% Gd and 50% Tb are shown in Figure 7.11. The hot heat sink temperature is 300 K. Terbium has a large peak heat capacity at 472 J/kg-K and, thus, even with a system pressure of 60 atm, the resulting utilization is relatively small at approximately 0.15. For this AMR, the layering structure is clearly seen in the resulting

temperature profile. Not only is there an obvious inflection in the curves near the transition temperature of Tb, but the temperature span is also significantly greater than the Gd AMR.

Large heat capacity is beneficial because it makes utilization small for a given fluid flux and therefore the perturbation of the refrigerant temperature is decreased. As is well known, from the theory of ideal passive regenerators small utilizations (large thermal mass) tend to be more efficient. However, in real regenerators if the utilization is too small the temperature span will be limited. The heat transfer fluid must pump entropy produced in the regenerator in addition to the entropy load from the cold end and, if the fluid entropy flux is too small, conduction, viscous losses, and insufficient heat transfer will reduce the net entropy being transferred through the regenerator.

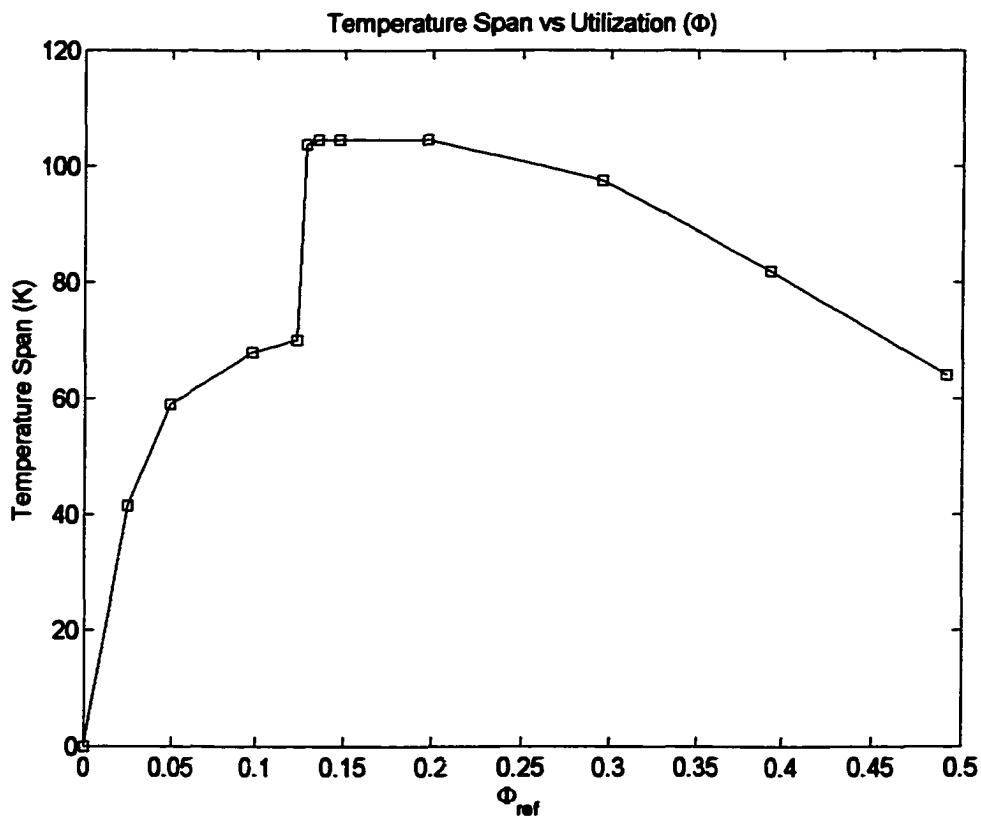

Figure 7.12 Temperature span of a 50% Gd – 50% Tb AMR as a function of utilization. The hot heat sink temperature is 300 K, the field change is 0 to 2 Tesla, and the utilization is referenced to the peak heat capacity of Tb.

The no load temperature span of a 50% Gd – 50% Tb AMR as a function of utilization is shown in Figure 7.12. The most striking observation is the abrupt increase in temperature span near a utilization of 0.13. The temperature decreases approximately 35 K in a stepwise manner.

Some of the reasons for this behaviour were described in 7.2.2. Further insight is possible if one focuses on the solid cycle above the Curie temperature and the symmetry is considered.

7.3.3 Heat Capacity Sensitivity

One of the advantages of the model is the ability to arbitrarily set the properties of a magnetocaloric material. If the MCE is a property derived from thermodynamic variables, then the heat capacity cannot be changed without affecting the adiabatic temperature change. Here, the heat capacity can be varied while leaving the MCE unchanged or the reverse can be performed. While this may simulate materials that are currently unknown, it allows one to determine the impacts of these parameters separately, providing insights into what constitutes a "good" magnetocaloric material for AMRs.

It has been shown for both a single-material and two-material AMR that some critical utilization is needed to force the temperature span to progress through the vicinity of the phase transition temperature. To better understand this behaviour, the impact of heat capacity is examined for the case of the Gd-Tb regenerator discussed above. All parameters are fixed except for the heat capacity. In particular, the system pressure is set to 40 atm. Four different scenarios are shown in Figure 7.13.

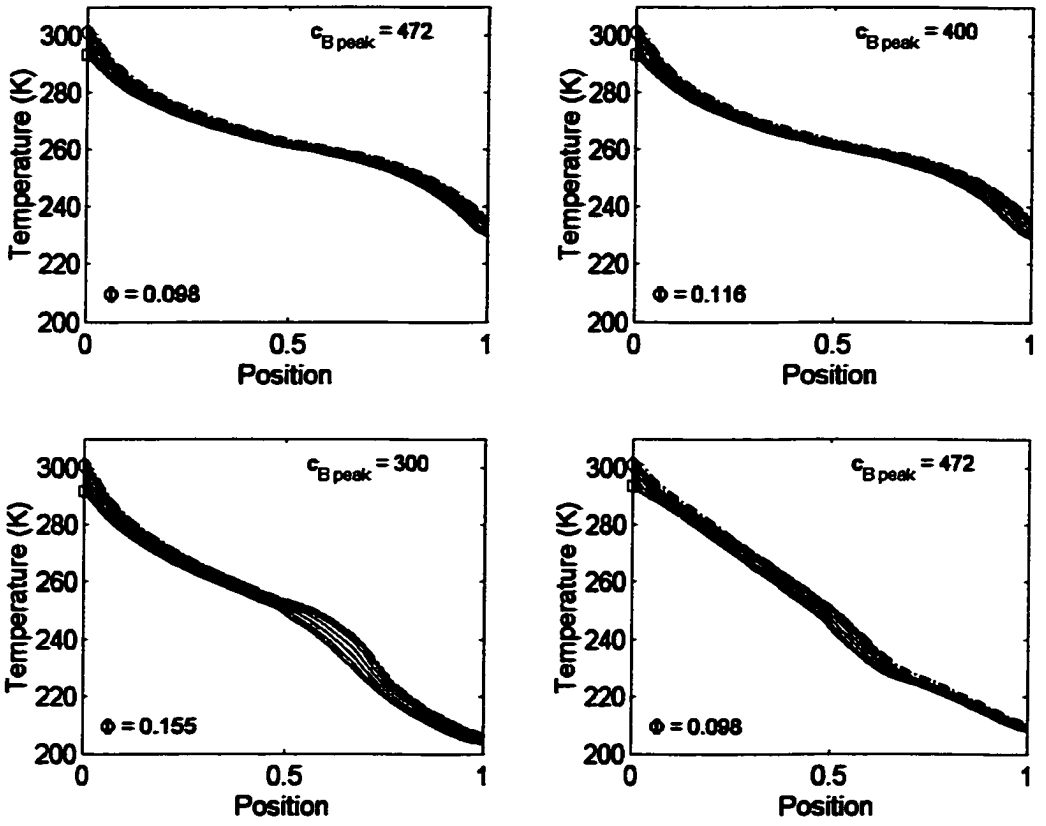

Figure 7.13 No load temperature profile for an AMR composed of 50% Gd and 50% Tb by length. All parameters and properties are fixed except for the refrigerant heat capacity.

The case in the top-left plot is for an AMR with actual heat capacity data for Tb and the plot in the top-right shows the results assuming the peak heat capacity of Tb is 400 J/kg-K. In both simulations, the temperature span has stopped near the transition temperature of 231 K. The plot in the bottom-left shows the temperature profiles with an assumed peak heat capacity of 300 J/kg-K. In this case, the utilization is large enough to move the cold temperature well past 231 K to a steady-state temperature of approximately 205 K.

The simulations with field dependent heat capacities assume that the relative difference between the low field and high field values are the same as for Gd. Thus, as the peak heat capacity is decreased, the absolute difference between the low, $c_B(T,B=0)$, and high field, $c_B(T,B=B_H)$, heat capacities (at the same temperature) decreases. The plot in the bottom-right of Figure 7.13 shows the model results when the heat capacity is independent of field. For this simulation, the heat capacity for both refrigerants is assumed to be temperature dependent only and equal to their zero field values. In this case, the temperature span has increased approximately 20 K and the cold temperature is near 210 K.

The assumption that heat capacity is temperature dependent only does not make the refrigerant symmetric; however, it does make the refrigerant symmetry greater than one for temperatures exceeding the Curie point. This is in contrast to the real symmetry, which is less than one for temperatures above T_{Curie} (see Figure 2.4). Symmetry less than one implies converging low field and high field entropy curves whereas symmetry greater than one gives diverging lines. In essence, specifying the refrigerant symmetry is another way of defining the MCE. For balanced flow conditions, the entropy curves should diverge, thus, changing the symmetry values to be greater than one acts, in a sense, to lessen the entropy mismatch of the refrigerant.

7.4 Local Work

When an AMR is operating in a periodic steady-state condition, a net flow of energy occurs from the cold end to the hot end. The divergence of this energy flux is equal to the local work [42],

$$W_x = \frac{dQ}{dx}. \tag{7.2}$$

It is interesting to see how the magnetic work is distributed for both the single-material and two-material simulations. Using the temperature profiles from the model and the magnetization data of [36] an algorithm was written calculating the net magnetic work at each location. The magnetic work is given by the area within the locus of magnetization verses applied field points according to,

$$W_x = (1-\alpha)A\oint B \cdot dM\ . \tag{7.3}$$

M is the volume magnetization and $(1-\alpha)A$ is the area of magnetic material at a location in the AMR (accounts for porosity).

Figure 7.14 shows the local work per unit length for two different AMRs. The top plot shows a Gd AMR operating with $T_H = 305$ K and a pressure of 160 atm, while the bottom plot is for a 50%Gd-50%Tb AMR with $T_H = 300$ K. All other parameters are the same and there is no cooling load. To determine the magnetic work of Tb the magnetization data of Gd was scaled using the ratio of the saturation magnetizations for the two materials. For the Gd AMR, most of the work is being performed near the hot end of the regenerator. In both cases, the majority of work input

occurs near the transition temperatures. This is to be expected since $\left(\frac{\partial m}{\partial T}\right)_B$ is maximized near the phase transition temperature.

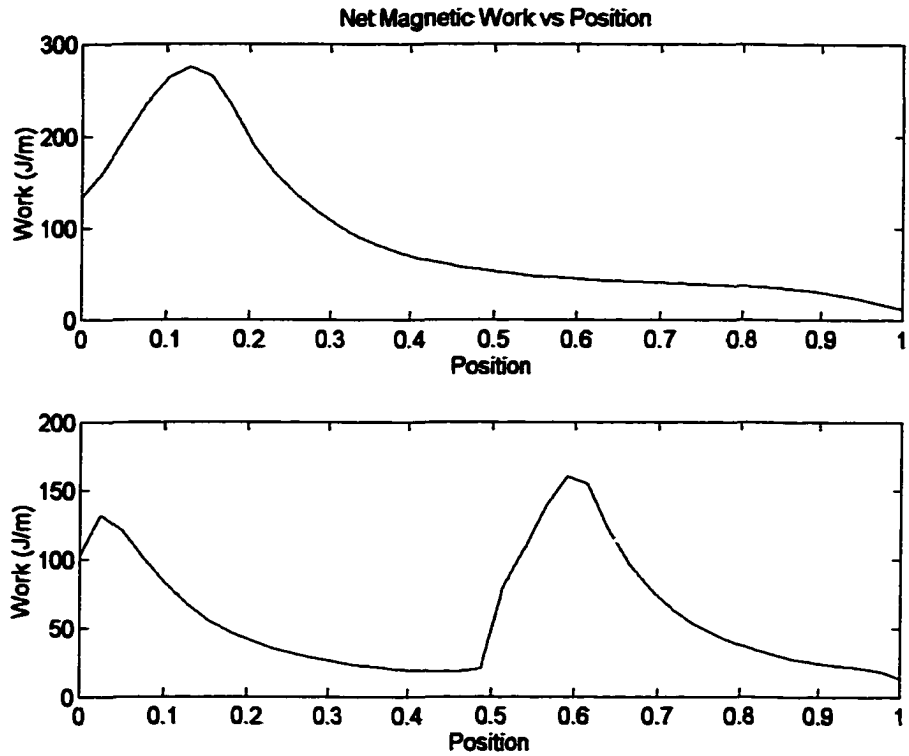

Figure 7.14 Local work per unit length with with no cooling load. The top plot is for a Gd AMR (T_H = 305 K), and the bottom plot is for a Gd-Tb (50%-50%) AMR (T_H=300 K).

In a manner similar to that of a simple compressible cycle, a magnetic indicator diagram can be drawn showing the local work on a field versus magnetization plot. Figure 7.15 is an example of this using the AMR data in the bottom plot of Figure 7.14. The various plots correspond to the hot end (x = 0), the cold end (x = 1) and locations in between. The indicator diagram is another way of showing the local work. However, an indicator diagram is more valuable than the presentation in Figure 7.14 because it allows the local cycle to be compared to an idealized cycle. As was shown in Chapter 2, for a balanced AMR the ideal MCE is a linearly increasing function of temperature. If one assumes a linear temperature profile exists through the AMR, a simple analysis shows that the local work per unit length should be constant for an ideal cycle [71]. Both Figure 7.14 and Figure 7.15 clearly show that the local work is not constant and that it can vary rapidly with real materials.

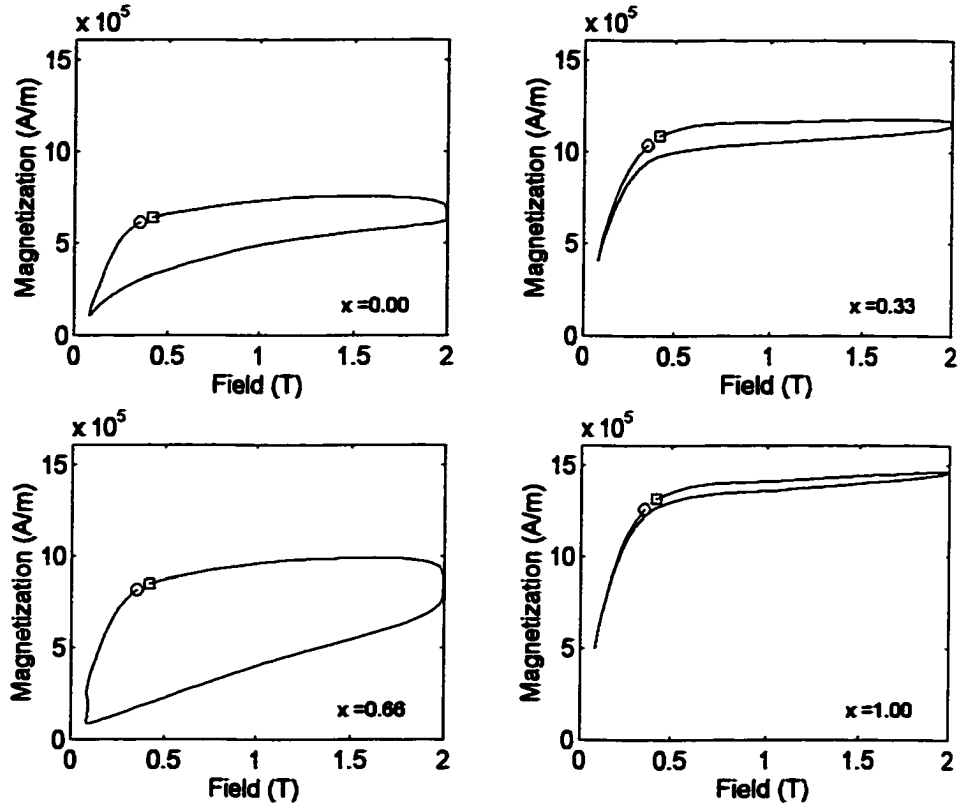

Figure 7.15 Indicator diagrams for various locations in a 50% Gd – 50% Tb AMR.

7.5 Summary

A number of simulations have been performed for AMRs operating both above and around the phase transitions. Perhaps the most significant results are those for the Gd-Tb simulations. It has long been known that there exists an upper limit on utilization for a regenerator to work over a desired temperature span. Passive results have shown that, ideally, small utilizations produce the most effective regenerators (where conduction and flow losses are minimal.) It has also been reported that decreasing utilization increases the no load temperature span of AMRs [59]. Contrary to these findings, results of simulations reported here have shown a minimum utilization is needed to establish a desired temperature span. This minimum has been termed the critical utilization and is defined by the near stepwise jump exhibited in AMRs with $T_H > T_{Curie}$. For a single material AMR operating near or below the transition temperature, the critical utilization is small. For a multi-material AMR or a single material AMR with $T_H > T_{Curie}$, the critical utilization can be significant as was shown in the Gd-Tb AMR simulations.

The jump phenomenon raises new questions regarding entropy transport in AMRs operating above refrigerant transition temperatures. Further analysis is required to clarify the impacts of symmetry, entropy production, and energy-work interactions; however, it appears that layering will succeed for appropriate operating conditions.

Chapter 8
Conclusions

8.1 Summary

In its entirety, the work reported in this thesis describes an investigation into the performance of AMRs using second-order magnetic refrigerants. The goal of this work is to increase our understanding of AMR behaviour near the ordering temperature so that the potential of this technology can be realized. Although this is important for single material AMRs, it is more imperative for the development of devices with large temperature spans requiring more than one refrigerant in the regenerator bed – so called, layered AMRs. Single material AMRs are now being investigated for commercial application; however, layered regenerators have not yet been proven. One of the motivations for the development of this idea is the possibility of creating a highly efficient device for hydrogen liquefaction.

8.1.1 Thermodynamic Analysis

The course of this study begins with a simplified analysis of AMR thermodynamics. Previous work is reviewed, and new relationships between material properties and the "ideal" AMR cycle are derived. By focusing on the heat transfer fluid and assuming small utilization, an expression describing the entropy generation per unit length in an AMR is derived. This expression is used to determine the ideal MCE for an AMR as a function of temperature and balance. For an AMR acting as a refrigerator, increasing the balance parameter tends to rotate the ideal MCE curve as a function of temperature in the direction of increased slope. An entropy balance is performed on the refrigerant producing a relationship similar in form to the ideal MCE differential equation. It is shown that an ideal magnetocaloric material requires the symmetry of the refrigerant to equal the balance parameter in the limit of small utilization. Previous studies have discussed the relationship between the ideal MCE and the entropy curves of a magnetocaloric material for a balanced AMR only.

8.1.2 Experimental Apparatus

Chapters 3 and 4 describe the design and fabrication of an experimental apparatus to test AMRs dynamically. A superconducting magnetic field generator is constructed using a NbTi solenoid recovered from an immersion cooled device. This device is completely separate from the

AMR subsystem and can be used in other experiments. Testing of the magnet produced a peak field of 2.5 Tesla at 185 Amps before joule heating caused the first stage temperatures to increase and the HTS leads to quench. This problem limited the useable field to approximately 2 Tesla. Higher field strengths would be preferable; however, time constraints required work to proceed with the rest of the apparatus design. With additional modifications, the full field of 5 Tesla may be attainable; however, the performance was deemed sufficient for initial experiments with the test apparatus.

A means of passively balancing the forces in a reciprocating active magnetic refrigerator was examined. Model results predict that a tuned condition could reduce the drive torque by approximately 50%, but the tuning parameters are extremely sensitive to operating conditions. Small variations in magnetic field strength, bed material, frequency, or temperature span require a large change in the counter-balance mass and the throw of the connecting rod (the offset was found to be relatively insensitive to operating conditions.) The sensitivity of the system, and the size of the masses required for useful balancing, makes the use of this form of passive balancing impractical.

Combing the field generator with the refrigeration subsystem creates the AMR Test Apparatus. The device is capable of testing AMR beds in the room temperature regime and at cryogenic temperatures as low as 20 K. It is composed of a vertically oriented reciprocating cylinder containing two AMR beds. The complete AMRTA extends the operating envelope to higher frequencies using smaller amounts of material. In this regard, the device is a unique tool that can be used to study and prove AMRs prior to their use in other magnetic refrigerators.

8.1.3 Model Development

The third part of this thesis concerns the development of a numerical model describing AMR energy transport. A recent algorithm intended for porous media with high heat transfer coefficients is used to solve the coupled non-linear energy equations. Problems with AMR modeling are discussed, in particular the lack of data regarding magnetic refrigerant properties. A way to avoid these problems is suggested by using a single well-characterized refrigerant as a prototype. Unlike previous models, the model domain encompasses a cold volume and additional hot volumes on either side of the regenerators to more accurately capture the device characteristics. Finally, the effect of demagnetizing fields on AMRs is briefly discussed and shown to be important for the case of refrigerants operating in or near the paramagnetic phase.

8.1.4 Experiment

The fourth part of this study describes experimental results of the AMRTA using Gd. These results are used to partially validate the model predictions. In all experiments a strong relationship between blow phasing and no load temperature span was discovered. The greatest temperature spans were developed when the AMRs were operating around their phase transition temperatures and with the blow advanced approximately 30 degrees. The phasing effect could not be simulated using the model and is believed to be due to the effects of demagnetizing fields. To date, operating frequencies have been as high as 1 Hz with a capability to operate at up to 1.2 Hz. Using a maximum field of 2 Tesla, no load temperature spans of 13 K, 18 K, and 20 K were produced with 125g, 250g, and 375g of gadolinium respectively. These temperature spans are comparable to devices of other researchers; however, 5-10 times less refrigerant is used in this apparatus. Further experiments are planned once the vacuum leaks are solved.

8.1.5 Numerical Simulations

The last stage of the thesis is a numerical investigation into AMR performance with the hot end being above the ordering temperature of the refrigerant. Prior to this work, operation under these conditions had not been studied in detail; however, an understanding of performance under these conditions is important for developing AMRs made up of multiple materials. Simulations of two-material layered beds are performed where the hot-end material is Gd and the cold-end material is $Gd_{0.74}Tb_{0.26}$ or Tb.

The performance of passive regenerators is commonly characterized in the ideal form with two parameters, the reduced length and the reduced period. In general, a large value of reduced length and a small reduced period produce an effective passive regenerator. The ratio of these parameters is the utilization; thus, small utilizations are best for ideal passive regenerators. Contrary to this, it has been shown here that in the case of an AMR operating above the refrigerant transition temperature, the temperature span of the regenerator increases nearly stepwise once some minimum utilization is exceeded. Thus, from the perspective of temperature span, small utilizations can produce poor performance in AMRs. Both single and multi-material simulations reveal a jump phenomenon occurring when the AMR cold temperature nears and exceeds the ordering temperature. The point where this occurs is termed the critical utilization.

To clarify understanding of this phenomenon, entropy balance, symmetry and energy-work interactions in the AMR are discussed. Although no single mechanism can be identified as causing this behaviour, utilization and N_{TU} have a strong impact on system dynamics. Only a

preliminary examination has been undertaken in this work, and experimental validation of this phenomenon is still required. This is an area for further work.

8.2 Synthesis

While the jump phenomenon was not experimentally validated in this work, it does explain previous experimental results for a Gd-Tb AMR reported by researchers at the David Taylor Naval Research Center [19, 20]. In these two studies, Green *et al.* used a pulsed field to test an AMR composed of Gd alone and then a Gd-Tb AMR. With the Gd AMR, they noticed that the no-load temperature was reduced by decreasing the operating pressure and the stroke of the fluid displacer. As a result, they programmed the displacer to reduce the stroke as the cold temperature decreased. From 290-250 K, the stroke was decreased by approximately 80%. The no load temperature span obtained with Gd was approximately 50 K.

Green *et al.* then used a Gd-Tb AMR in the same device and to their surprise could only produce a temperature span of approximately 24 K. The difference in performance between this bed and the Gd AMR could not be explained although the MCE and field profile produced by the solenoid were thought to be responsible.

The numerical results in Chapter 7 can explain the results of both experiments. For the Gd AMR, reducing the pressure and stroke, decreased the utilization. From Figure 7.9 we can see that the no load temperature span for a Gd AMR increases as utilization is decreased up to a point. This is the effect observed in [19]. Unfortunately, the same conditions were used for the tests with the Gd-Tb AMR i.e. the stroke (utilization) was reduced as the cold temperature decreased. As can be seen in Figure 7.12, utilizations less than the critical value will give much smaller temperature spans in the Gd-Tb AMR. Instead of decreasing the stroke as they did with Gd, Green *et al.* should have increased the stroke in an attempt to produce a larger temperature span.

8.3 Recommendations for Further Work

With a working apparatus, a number of questions raised in this thesis can be addressed experimentally as well as numerically. The following items are recommended for action:

a. Solve the vacuum leak – this should allow greater temperature spans to be produced and to increase the cooling power of the device. At the time, leak-checking was unsuccessful, and, instead of delaying the experiments until the leak was found, it was decided that room temperature tests could be carried out with no vacuum. To do this, the cylinder shell

was insulated with a layer of closed-cell neoprene to reduce heat leaks to the cylinder cold section and to the regenerators. It appears that the major leaks have now been found and corrected. It should be confirmed that a pressure on the order of 10^{-4} or better can be sustained for future tests. This is imperative for low temperature testing.

b. Make modifications to the magnet to increase the available field strength. The overall thermal conductance between the HTS leads and the first and second stages of the cryocooler must be increased. This can be done in two ways: use additional thermal links, or move the leads closer to the cryocooler. The latter requires more work in terms of machining and hours, but is the recommended course of action to permanently correct the problem. Furthermore, the normal leads should be optimized in favour of larger currents. The conduction losses down the leads are small relative to the joule heating so this will aid in attaining high field operation. Finally, all current carrying joints should be soldered to reduce contact resistances.

c. Increase utilization – although the fluid displacer performed well during testing, it became apparent that the ability to increase Φ further would be useful. In order to do this, the thermal capacity of the heat transfer fluid relative to the refrigerant must be increased. This means that to continue using helium, the mass flux of gas must be larger or the mass of refrigerant smaller. The latter is not recommended since less refrigerant reduces cooling power and would increase the effects of parasitic leaks. Currently, the displacer is rated to a maximum of 10 atm and has a maximum overall stroke of 24 cm. Coupled with the inside diameter, this limits the maximum mass flux. Using a denser fluid such as a water-glycol mixture would solve this problem for high temperature testing.

d. Modify the hot heat sink for active temperature control. The net heat flux into the hot heat exchangers tends to cause the hot heat sink temperature to float. An intermediate fluid loop coupled to a thermal controller would make the experiments much more controllable and repeatable.

e. Synthesize additional refrigerants. Selecting refrigerants based on MCE satisfies the entropy flux constraint through the AMR; however, this does not necessarily satisfy the solid to fluid cyclic entropy balance or energy balance. Ideally, MCE and refrigerant symmetry must be satisfied which means that the high and low field entropy curves cannot be arbitrary. Layering tends to focus on the MCEs, but does not help with the symmetry constraint. Composite materials with ideal symmetry-MCE curves should be synthesized and tested.

f. Experiments with layered AMRs need to be carried out. Tests using two-material layered AMRs should be performed to validate the model predictions. Ideally, both room temperature and low temperature (77-20 K) experiments are needed. The strong temperature dependence of material properties at low temperature makes this range more difficult; therefore, it is recommended that the former be performed first. Once two-material AMRs have been proven, the number of materials should be increased.

g. Modify the numerical model for low temperature simulations. Currently, the field and temperature dependence of refrigerant properties is based upon Gd and scaled for other materials with Curie temperatures near Gd. For low temperature simulations, this scaling will be less valid. Specific refrigerant properties should be included.

h. Include Maxwell's equations to solve the magnetostatic problem. The impact of demagnetization on AMR performance for low and high fields is significant for AMRs operating near and above the transition temperature. A model including the magnetostatic problem will require at least two spatial dimensions thereby making solution computationally intensive. Such a model may provide further insight into optimum flow-field phasing.

Besides the items described above, additional tests using Gd are warranted. Fully mapping the performance of this refrigerant as a function of utilization and cooling load will provide a useful baseline for further research. There are no published reports providing a full spectrum of data for a refrigerant in a single AMR apparatus. Currently, it is unclear to what degree reported results of AMRs are related to the characteristics of the particular device or to the operating conditions. This has made it difficult for independent researchers to provide insight into AMR operation. A well defined data set will allow others to study the AMR problem analytically and numerically without the time and expense associated with the construction of their own apparatus.

Appendix A
Force Modeling

To be an efficient means of producing refrigeration a Magnetic Refrigerator, like a gas cycle refrigeration process, must make use of the work produced in the relaxation process. In a gas cycle this means capturing the work of expansion, in a magnetic refrigerator this corresponds to the demagnetization work. Conventional MR configurations can be classified as reciprocating, rotary or pulsed field. Charging and discharging a superconducting magnet cannot be performed quickly without inducing transient losses; furthermore, pulsed fields have the disadvantage of requiring the power supply to provide work to charge and discharge the magnetic field as well as to produce the magnetic cycle. Rotary MRs are unique in that the magnetic forces can be made to cancel each other so that the net work is naturally the cycle work. The disadvantage of the rotary geometry is the complexity of the seal. Reciprocating MRs have the advantage of being easier to seal than rotary and can have operating frequencies that are much higher than a pulsed field. However, a significant disadvantage of reciprocating designs using a simple solenoid (whether moving beds or moving magnet) is the presence of large unbalanced magnetic forces resulting in a larger drive system. This is a serious drawback and one of the reasons that reciprocating MRs do not tend to display system efficiencies as high as theory predicts.

A common reciprocating MR configuration consists of a single solenoid with a moving cylinder inside the magnet. The cylinder carries two beds of magnetic refrigerant that undergo an Active Magnetic Regenerator (AMR) cycle. Other reciprocating MRs consist of moving magnets, or two co-axial magnets with a single moving cylinder [23]. The latter systems can be designed to be force balancing unlike those with single solenoids. Because the magnitude of the unbalanced forces can far exceed those required for the magnetic cycle, structural and drive system components need to be rated for a much larger capacity which incurs greater expense.

An AMR test apparatus that uses a single solenoid with a reciprocating geometry has been developed and described in Chapters 3 and 4. During the apparatus design, methods of passively reducing the unbalanced magnetic forces were studied. An analysis of quasi-static magnetic forces on rotary and reciprocating MR geometries has been carried out previously [18]. A more detailed model using the system Lagrangian has been developed to look at dynamic as well as static forces, the influence of passive components, and the resulting motion of the apparatus with a specific AMR bed and a known temperature profile. Components modeled include the AMR beds, a connecting rod, a counter-balance, a flywheel and dissipation due to a gas displacer. An

optimization of the passive component geometry was carried out to minimize the input drive torque.

Model Development

The apparatus under consideration is described in Chapter 4. Actual components included in the dynamic model are: the cylinder carrying the regenerator beds, the connecting rod driving the cylinder, the drive shaft (including crank-arm) and the gas displacer (representing a dissipation due to pressure drop through the system.) Hypothetical components meant to balance the forces are a flywheel, connecting rod and counter-balance. The drive motor is not included because the size of this component is a function of the system response and, ultimately, is the parameter that we want to minimize.

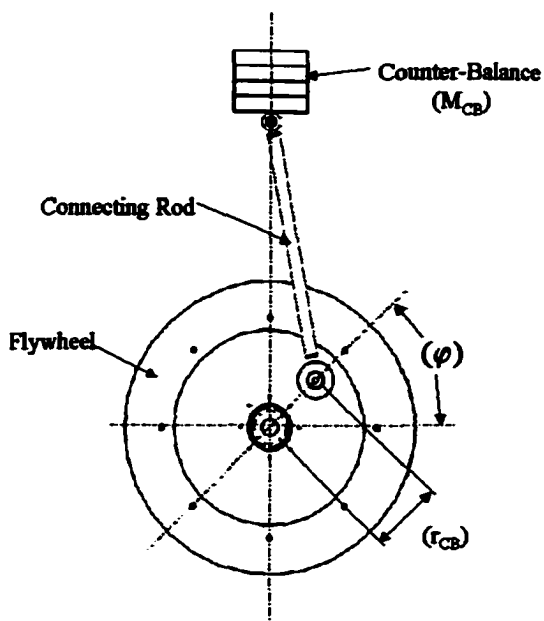

Figure A.1 The hypothetical passive components used to balance the reciprocating AMR apparatus.

The hypothetical parts are shown in Figure A.1 and will be termed the passive components. The passive components are intended to do two things: (1) store kinetic energy in an inertial mass to dampen out fluctuations in rotation speed; and, (2) produce a waveform out of phase and similar in magnitude to the magnetic forces in order to reduce the drive load by superposition. The counter-balance is simply a mass, M_{CB}, that reciprocates up and down by being attached to the flywheel at some radius, r_{CB}, and at some angular offset, φ (where the angular datum is when

the cylinder is in the center position, z=0.) The passive components are coupled to the cylinder drive shaft through a 2:1 gearbox (this is required so that the mass waveform matches the magnetic waveform as will be seen.) The counter-balance mass could be mounted on the periphery of the flywheel; however, this does not include the inertial effects that result from the reciprocating motion. Since the cylinder is reciprocating, the waveform is more closely matched by the coupling method shown in Figure A.1.

The apparatus dynamics can be conveniently described using Lagrange's equations,

$$\frac{d}{dt}\left(\frac{\partial L}{\partial \dot{\xi}_j}\right)-\frac{\partial L}{\partial \xi_j}=\Xi_j, \quad \text{where,} \quad L\equiv T\left(\xi_j,\dot{\xi}_j\right)-V\left(\xi_j\right) \tag{A.1}$$

T and V are the total system kinetic energy and potential energy respectively, ξ_j, are the generalized coordinates, and, Ξ_j, are the generalized forces acting on the system. In this case, the generalized coordinates can be reduced to a single degree of freedom in the angular position of the drive shaft, θ. The potential energy and kinetic energy of all components in the systems can be written in terms of θ and ω, the angular velocity. The forces acting on the system include the magnetic force, the drive torque required to overcome viscous dissipation in the heat transfer fluid, and the torque produced by the drive motor. Summing up the contributions due to each sub-component produces relations for the total kinetic energy and potential energy. Geometry and mass estimates for each component are used to calculate moments of inertia about the drive shaft axis.

The dissipation function represents the pressure loss through the gas transfer circuit. In particular, a helium circuit composed of the following components was modeled: a displacer coupled to two flex hoses, two heat exchangers, two regenerator beds, and cold section transfer tube. The generalized force due to viscous dissipation is determined using empirical correlations for pressure drop through the components of the fluid flow system. The dominant term is due to dissipation through the regenerator beds and is calculated assuming each bed is composed of spherical particles and is described by the Ergun equation. Because the gas displacer is directly coupled to the drive shaft, the gas mass flow rate can be written directly in terms of θ and ω as is required for this analysis.

The magnetic force acting on a volume of magnetic material can be determined by,

$$\bar{F}=\int_{Vol}(\bar{M}_v\cdot\nabla)\bar{B}_a dV \tag{A.2}$$

where M_v is the volume magnetization of material, and $B_a = \mu_0 H_a$ is the applied magnetic flux [62]. If it is assumed that the flux density and magnetization are uniform over a volume of material (exact for a differential volume) and that the magnetization of the material has little effect on the induced flux density (i.e. demagnetizing effects neglected), then the magnetic force on the volume is given by,

$$\vec{F} = M_z \frac{\partial B_z}{\partial z} \vec{k}. \tag{A.3}$$

In Equation (A.3), M_z is the total magnetic moment of the volume. There are several other terms that have been dropped due to symmetry (assuming the cylinder is on the solenoid axis) and because the only admissible variation results in reciprocating motion (in this analysis we are not interested in internal forces of the AMR beds). It is assumed that the magnetic materials have no hysteresis and that the net moment is aligned parallel to the applied field. The magnitude and gradients of B were determined using a 2-D, axis-symmetric model of the solenoid in Ansys™. A path was then defined for the position of the regenerators as they enter and leave the high magnetic region. Using this path, the field gradients required for Equation (A.3) were calculated and exported to a data file.

With the AMR volumes specified, it is possible to calculate the magnetic forces experienced by the magnetic material once the magnetization is known. The local magnetization of the material in the AMR beds is specific to the refrigerant type and the temperature profile through the AMR. The magnetic material properties were estimated using the mean field theory of molecular magnetic moments. As described in Chapter 5, the mean field model determines magnetization as a function of applied field and temperature.

The magnetization of the material is a function of temperature. To simulate the affects of the magnetic cycle an algorithm was created to set the temperature profile in the beds as a function of cylinder location. It was assumed that each section of the AMR bed undergoes a reverse Brayton cycle. The temperatures at the hot and cold end of the regenerators were specified arbitrarily and the temperature through the bed was specified for the beginning of the fluid blow from the hot to cold end of the AMR. Between the blow phases, the temperature change of the bed is determined as that resulting from an isentropic field change. The regenerative temperature change at each location of the bed is calculated based upon energy conservation between the heat transfer fluid and the regenerator bed. For a cylinder composed of two regenerator beds the net force on the

cylinder is determined by taking the sum of the individual bed forces where it is noted that each bed is 180 degrees out of phase with the other.

The final generalized force required to solve the dynamic equation is the drive torque. This is an arbitrary parameter. With a defined input torque, the dynamic model determines the resulting waveform as a function of time.

The last part of the analysis is optimizing counter-balance mass and geometry to maximize the effect of the passive components; this is seen as a reduction in the peak torque. The parameters to be optimized were the counter-balance mass, M_{CB}, the radial position of the mass crank pin on the flywheel, r_{CB}, and the angular offset of the mass with respect to the cylinder position, φ_{CB} (See Figure A.1.) The objective function to be minimized is the RMS torque, T_{RMS}:

$$\min T_{RMS} = \left[\frac{1}{2\pi}\int_0^{2\pi} T^2(\theta)d\theta\right]^{\frac{1}{2}}, \tag{A.7}$$

$$\begin{aligned} \text{subject to:}\quad & 0 \le M_{CB} \le 40\,\text{kg}, \\ & 0 \le r_{CB} \le 0.23\,\text{m}, \\ & 0 \le \varphi_{CB} \le 2\pi. \end{aligned} \tag{A.8}$$

T is the instantaneous torque as a function of angular position.

Table A-1. Force Model Parameters.

Parameter	Value
Magnetic Field Strength	5 T
Material	Gadolinium
Bed Diameter (D)	2.5 cm
Aspect Ratio (L/D)	3
Particle Size	300 um
Porosity	0.38
Gas Pressure	7 atm
Displacer Total Stroke	20 cm
Temperature Span	295-220 K
Frequency	1 Hz

Model Results

A reciprocating AMR test apparatus with the properties listed in Table A-1 was studied. The predicted magnetic forces on the regenerator beds and cylinder for a temperature span of 295 to 220 K as a function of position are shown in Figure A.2. As can be seen, although there is some force cancellation due to the presence of two beds, it is insignificant compared to the peak force experienced by a single bed. In the top plot, each regenerator experiences a peak force on the order of 600 N while in the bottom graph the peak cylinder force is 546 N – a reduction of only 10%. It is possible to optimize the field shape so that there is better force cancellation; however, this may lead to larger forces experienced by the individual regenerators due to larger field gradients. This is a topic for further study.

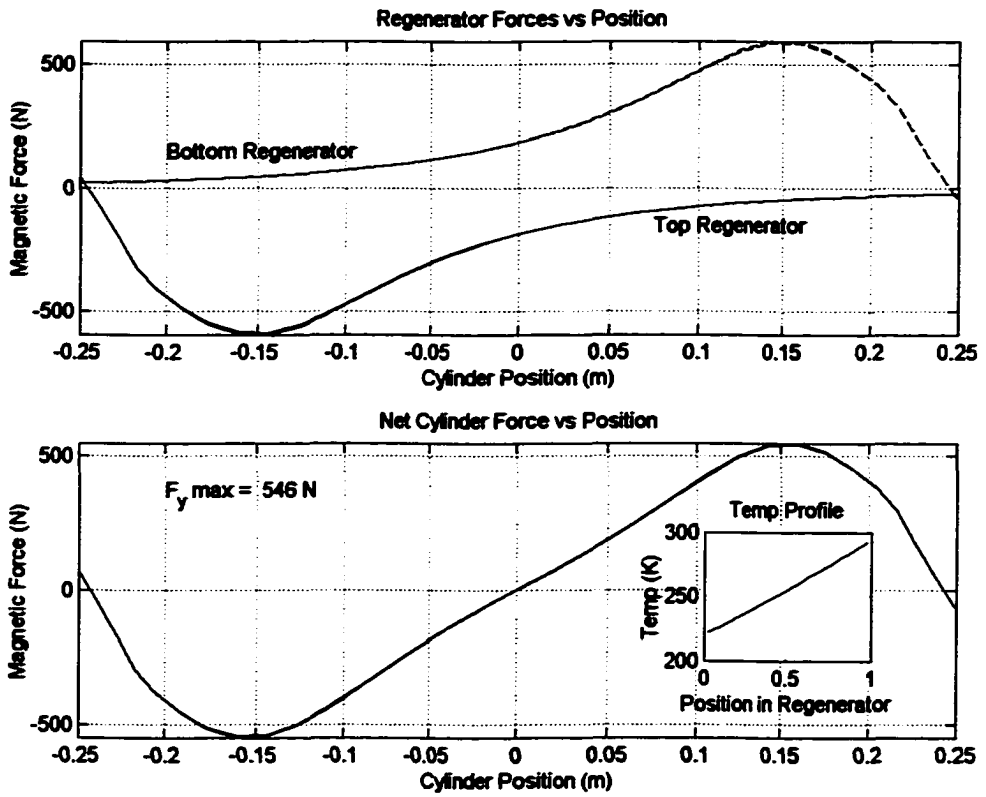

Figure A.2 Magnetic forces on regenerator beds composed of gadolinium. The net force on each bed is shown in the top plot and the sum of the two beds gives the net cylinder force shown in the bottom plot. The assumed temperature profile through the bed is shown in the inset at bottom right.

Although it can not be seen because the temperature span is far below the Curie temperature, a small net area is enclosed in Figure A.2. The algorithm for bed temperature as a function of

angular position creates a magnetic cycle involving net work input. As the material temperature moves away from the Curie point, the net magnetic work decreases and the area described by the curve becomes smaller. Because of this, the work input for the Gd cycle is not evident in the bottom plot of Figure A.2. As the temperature span decreases, or if the bed is made up of materials operating around their Curie temperatures, the change in magnetization due to heat transfer becomes more significant relative to the absolute magnetization. This will significantly impact the balancing parameters; however, it should also substantially decrease the total magnetic force acting on the regenerators which is beneficial.

A plot of cylinder, connecting rod, and gas displacer torque as a function of angular position is shown in Figure A.3. Summation of these three components results in a net input torque from the motor. A positive value for torque implies work input while the reverse is true for work output. Although averaging of the torque over a complete cycle results in a small work input, the extremes of the load are quite large and, moreover, are reversing.

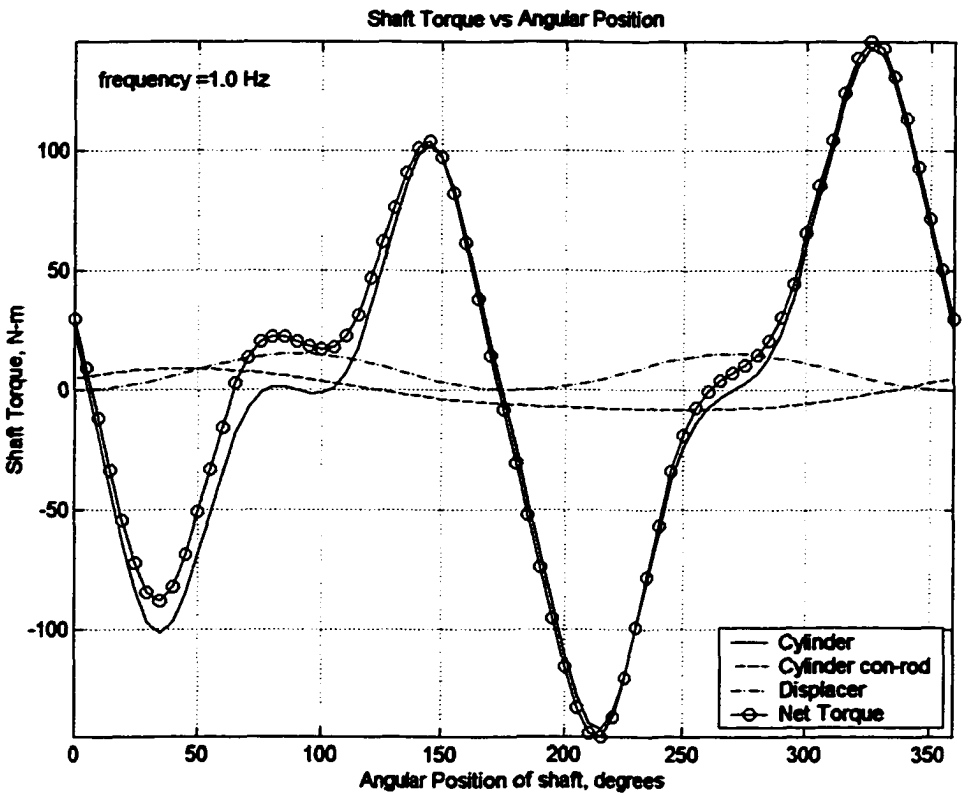

Figure A.3 Shaft torque as a function of angular position.

The system torque is largely due to the cylinder and results from inertial and magnetic forces. As shown in Figure A.3, the waveform for the cylinder torque has a frequency that is twice the rate of rotation. By coupling the counter-balance though a 1:2 gear-box and by adjusting phasing, a torque function is generated that opposes the cylinder. If the counter-balance is on the flywheel a sine wave results. A sine wave cannot match the plateau in the cylinder curve, whereas with the connecting rod geometry a plateau can be produced. This affect arises due to the inertial force reversal at each end of the connecting rod stroke. Unfortunately, the connecting rod from the flywheel to the counter-balance produces an additional, relatively large, reversing torque that complicates the total waveform.

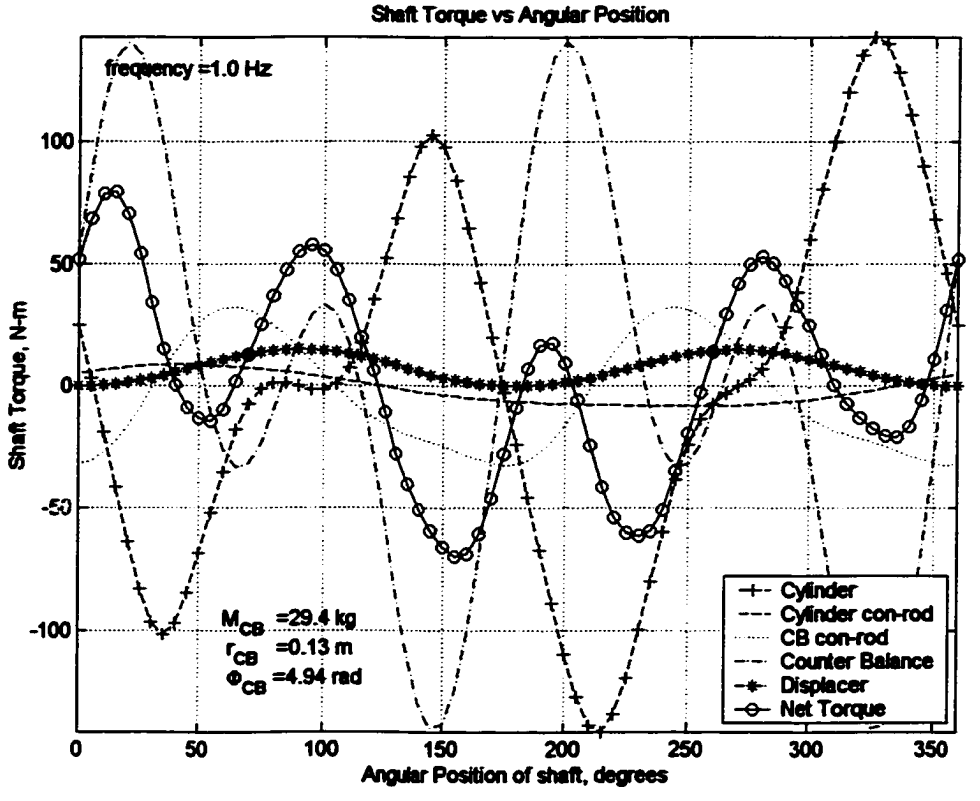

Figure A.4 Torque as a function of angular position for each component including passive balancing. Balancing parameters are the result of optimization.

Figure A.4 shows the net torque resulting from the addition of the passive balancing components. The parameters for the balancing components are the results of the optimization routine. This net torque now has an amplitude that is approximately 50% of the unbalanced configuration (75 N-m versus 150 N-m). An unfortunate consequence is the increase in the number of torque reversals. The effects of this can be explored by solving the equation of motion

for the system. For a given input torque the angular position and velocity are solved as a function of time. Unlike the previous calcluations where the frequency is fixed at a known value, the impact of the flywheel inertia becomes important. The purpose of the flywheel is to absorb the unbalanced forces and to smooth the reponse of the system to a constant drive torque. In practice, it is expected that the ripple in angular velocity would be less than predicted by the model. While the model assumes a constant input torque, a constant speed electric motor would vary the torque in an attempt to maintain angular velocity. A significant ripple may cause large vibration and increase fatigue. In this regard, it is desireable to minimize the variations in the velocity wave.

The sensitivity of the system to different regenerator volumes, magnetic field strength, temperature span, frequency, and magnetic refrigerant was examined. All of these variables can significantly change the magnitude of the magnetic force, thereby generating very different cylinder torques. It was found that the optimized parameters for the passive components varied significantly requiring a "dynamic" means to tune the system. The inability to effectively balance the drive torque over a sufficiently broad range of operating conditions is a serious drawback for this particular balancing scheme. These results indicated that passive balancing for the AMRTA would not be easy and another means of dealing with the unbalanced magnetic forces needed to be found.

The drive system needs to produce a constant angular velocity. To do this, the unbalanced magnetic force needs to be actively controlled. In the end, this problem was solved using a regenerative drive package consisting of DC motor and regenerative controller. The controller allows the angular velocity to be set by the user. At the points in the cycle where the cylinder is trying to drive the motor the controller adjusts the armature current so that the motor acts as a generator. The power is produced by the motor is then fed back into the grid. The efficiency for the controller alone is approximately 97% according to manufacturers specifications. Motor speed is maintained within 5% of the set speed.

References

1. Schrope, M., "Which way to energy utopia?," Nature, 414, (2001), pp. 682-684.

2. Dincer, I., "Technical, environmental and exergetic aspects of hydrogen energy systems," International Journal of Hydrogen Energy, 27, (2002), pp. 265-285.

3. Dresselhaus, M. S., and Thomas, I. L., "Alternative energy technologies," Nature, 414, (2001), pp. 332-337.

4. Schlapbach, L., and Zuttel, A., "Hydrogen-storage materials for mobile applications," Nature, 414, (2001), pp. 353-358.

5. Bejan, A., "Theory of heat transfer-irreversible refrigeration plants," Int. J. Heat Mass Transfer, 32, (1989), pp. 1631-1639.

6. Warburg, E., Ann. Phys. Chem., 13, (1881), p. 141.

7. Debye, P., Ann. Phys. Chem., 81, (1926), p. 1154.

8. Giauque, W. F., and MacDougall, D. P., "Attainment of temperature below 1 degree absolute by demagnetization of Gd2(SO4)3•8H2O," Physics Review, 43, (1933), p. 768.

9. Daunt, J. G., and Heer, C. V., "Addendum: Heat flow in metals below 1 K and new method for magnetic cooling," Physical Review, 76, (1949), p. 768.

10. Heer, C. V., Barnes, C. B., and Daunt, J. G., "The design and operation of a magnetic refrigerator for maintaining temperatures below 1 K," Review of Scientific Instruments, 25 (1954) pp. 1088-1098.

11. Van Geuns, J. R., Philips Res. Rep. Suppl., 6, (1966).

12. Brown, G. V., "Magnetic heat pumping near room temperature," Journal of Applied Physics, 47, (1976), pp. 3673-3680.

13. Pratt Jr., W. P., Rosenblum, S. S., Steyert, W. A., and Barclay, J. A., "A continuous demagnetization refrigerator operating near 2 K and a study of magnetic refrigerants," Cryogenics, 17, (1977), pp. 689-794.

14. Steyert, W. A., "Stirling-cycle rotating magnetic refrigerators and heat engines for use near room temperature," Journal of Applied Physics, 49, (1978), pp. 1216-1226.

15. Steyert, W. A., "Rotating Carnot-cycle magnetic refrigerators for use near 2 K," Journal of Applied Physics, 49, (1978), pp. 1227-1231.

16. Barclay, J. A., and Steyert, W. A., "Magnetic refrigerator development," Electric Power Research Institute, report EPRI-EL 1757, (1981).

17. Barclay, J. A., "The Theory of an Active Magnetic Regenerative Refrigerator," in Proc. of 2nd Conf. of Refrigeration for Cryogenic Sensor and Electronic Systems, (NASA Goddard Research Center), (1982).

18. Barclay, J. A., et al., "Design limitations on magnetic refrigerators imposed by magnetic forces," in Proceedings of the 4th Int. Cryocooler Conference, Eastown, MD, (1986).

19. Green, G., Patton, G., Stevens, J., and Humphrey, "Reciprocating magnetic refrigerator," in Proc. 4th Intl. Cryocooler Conf., Easton, Md. (1986).

20. Green, G., Patton, G., Stevens, J., and Humphrey, "Magnetocaloric refrigeration," David Taylor Naval Ship Research and Development Center, Report DTNSRDC-87/032, (1987).

21. Cross, C. R., Barclay, J. A., DeGregoria, A. J., Jaeger, S. R., and Johnson, J. W., "Optimal temperature-entropy curves for magnetic refrigeration," Advances in Cryogenic Engineering, 33, (1988), p. 767.

22. Cogswell, F. J., Iwasa, Y., and Smith Jr., J. L., IEEE Transactions on Magnetics, 24, (1988), pp. 1011-1014.

23. Seyfert, P., "Research on magnetic refrigeration at CEA Grenoble," Advances in Cryogenic Engineering, 35, (1990), pp. 1087-1096.

24. Green, G., Chafe, J., Stevens, J., and Humphrey, J., "A Gadolinium-Terbium active regenerator," Advances in Cryogenic Engineering, 35, (1990), pp. 1165-1174.

25. Gschneidner Jr., K. A., Pecharsky, V. K., "Magnetocaloric materials," Annu. Rev. Mater. Sci, 30, (2000), p. 387.

26. Tishin, A. M., Magnetocaloric effect in the vicinity of phase transitions, in Handbook of Magnetic Material, edited by K. H. Buschow, Amsterdam, Elsevier, 12, (1999), pp 395-524.

27. Pecharsky, V. K., and Gschneidner Jr., "Gd5(SixGe1-x)4: An extremum material," Advanced Materials, 13, (2001), pp. 683-686.

28. Giguère, A., Foldeaki, M., Ravi Gopal, B., Chahine, R., Bose, T. K., Frydman, A., and Barclay, J. A., "Direct measurement of the 'giant' adiabatic temperature change in Gd5Si2Ge2," Physical Review Letters, 83, (1999), pp. 2262-2265.

29. Tegus, O., Bruck, E., Buschow, K. H. L., and de Boer, F. R., "Transition-metal-based magnetic refrigerants for room-temperature applications," Nature, 415, (2002), pp. 150-152.

30. DeGregoria, A. J., Feuling, J. F., Laatsch, J. F., Rowe, J. R., Trueblood, J. R., and Wang, A. A., "Test results of an active magnetic regenerative refrigerator," Advances in Cryogenic Engineering, 37, (1992), pp. 875-882.

31. Zimm, C. B., Jastrab, A. G., and Johnson, J. W., "Design of active magnetic regenerative stage interfacing to a G-M cryocooler," Cryocoolers 8, Plenum, New York, (1995), pp. 657-664.

32. Wang, A. A., Johnson, J. W., Niemi, R. W., Sternberg, A. A., and Zimm, C. B., "Experimental results of an efficient active magnetic regenerator refrigerator," Cryocoolers 8, Plenum, New York, (1995), pp. 665-676.

33. Zimm, C. B., Johnson, J. W., and Murphy, R. W., "Test results on a 50K magnetic refrigerator," Advances in Cryogenic Engineering, 41, (1996), pp. 1675-1681.

34. Zimm, C., Jastrab, A., Sternberg, A., Pecharsky, V., Gschneidner Jr., K., Osborne, M., and Anderson, I., "Description and performance of a near-room temperature magnetic refrigerator," Advances in Cryogenic Engineering, 43, (1998), pp. 1759-1766.

35. Magnetic refrigerator successfully tested, Ames Laboratory news release, Dec, (2001), www.exteranl.ameslab.gov/News/release/01magneticrefrig.html.

36. Dan'kov, S. Y., Tishin, A. M., Pecharsky, V. K., and Gschneidner Jr., K. A., "Magnetic phase transitions and the magnetothermal properties of gadolinium," Physical Review B, 57:6, (1998), pp. 3478-3490.

37. Barclay, J. A., and Steyert Jr., W. A., Active Magnetic Regenerator, U.S. Patent No. 4 332 135, June (1982).

38. Matsumoto, K., Hashimoto, T., "Thermodynamic analysis of magnetically active regenerator from 30 to 70 K with a brayton-like cycle," Cryogenics, 30, (1990), p. 840.

39. Carpetis, C., "Numerical study of magnetic refrigerator including consideration of magnetic nanocomposites," Proc. of the XVIIIth International Congress of Refrigeration, Montreal, CANADA, (1991).

40. DeGregoria, A. J., "Modeling the active magnetic regenerator," Advances in Cryogenic Engineering, 37, (1992), p. 867.

41. Carpetis, C., "An assessment of the efficiency and refrigeration power of magnetic refrigerators with ferromagnetic refrigerants," Advances in Cryogenic Engineering, 39, (1994), p. 1407.

42. Hu, J. C., and Xiao, J. H., "New method for analysis of active magnetic regenerator in magnetic refrigeration at room temperature," Cryogenics, 35, (1995), pp. 101-104.

43. Hall, J. L., Reid, C. B., Spearing, I. G., and Barclay, J. A., "Thermodynamic considerations for the design of active magnetic regenerative refrigerators," Advances in Cryogenic Engineering, 41, (1996), pp. 1653-1663.

44. Smaili, A., and Chahine, R., "Thermodynamic investigations of optimum active magnetic regenerators," Cryogenics, 38, (1998), p. 247.

45. Spearing, I. G., Improving the Refrigeration and Gas Liquefaction Performance of Gifford-McMahon and Active Magnetic Regenerative Cryocoolers: A study of Flow Maldistribution, Unbalance, and Asymmetry, Ph.D. Thesis, University of Victoria, Victoria, (2000).

46. Wood, M. E., and Potter, W. H., "General analysis of magnetic refrigeration and its optimization using a new concept: maximization of refrigerant capacity," Cryogenics, 25, (1985), pp. 667-683.

47. Pecharsky, V. K., and Gschneidner Jr., K. A., "The giant magnetocaloric effect in Gd5(SixGe1-x)4 materials for magnetic refrigeration," Advances in Cryogenic Engineering, 43, (1998), pp. 1729-1736.

48. Barclay, J.A., Bose, T.K., Rowe, A. and Chahine, R., "Development of Magnetic Refrigerants for Magnetic Liquefaction of Hydrogen," Phase IV, Year 2, Annual Report for April 1, 2000 – March 31, 2001, Natural Resources Canada (2001).

49. Schuricht, S. R., DeGregoria, A. J., and Zimm, C. B., "The effects of a layered bed on active magnetic regenerator performance," Proc. of the 7th International Cryocooler Conference, Plenum, New York, (1993), pp. 614-620.

50. Kuz'min, M. D., and Tishin, A. M., "Magnetocaloric effect part 2: magnetocaloric effect in heavy rare earth metals and their application to magnetic refrigeration," Cryogenics, 33, (1993), pp. 868-882.

51. Zhang, L., Sherif, S. A., DeGregoria, A. J., Zimm, C. B., and Veziroglu, T. N., Cryogenics 40, (2000), p. 269.

52. Merida-Donis, W., Development of monolithic regenerator technology for low temperature (4 K) Gifford-McMahon cryocoolers, M.A.Sc. Thesis, University of Victoria, (1996).

53. Hasebe, T., Sakuraba, J., Jikihara, K., Watazawa, K., Mitsubori, H., Sugizaki, Y., Okubo, H., Yamada, Y., Awaji, S., and Watanabe, K. "Cryocooler cooled superconducting magnets and their applications," Advances in Cryogenic Engineering, 43, (1998), p. 291.

54. Wilson, M., Superconducting Magnets, Oxford University Press, New York (1983).

55. Caudle, K. J., Characterization of regenerator geometries, M.A.Sc. Thesis, University of Victoria, (1997).

56. Barron, R., Cryogenic Systems, Oxford University Press, New York, (1985).

57. Bejan, A., Convection Heat Transfer, John Wiley and Sons, Inc., New York, (1984).

58. Schmidt, F. W., and Wilmott, J. J., Thermal Energy Storage and Regeneration, Hemisphere Publishing Corporation, Washington DC, (1981).

59. Hashimoto, T., Numasawa, T., Shino, M., and Okada, T., Cryogenics, 21, (1981), pp. 647-653.

60. Smart, J. S., Effective Field Theories of Magnetism, W. B. Saunders Company, Philadelphia, (1966).

61. Sun, Z. F., and Carrington, C. G., "A new numerical scheme for convective dominated heat transfer in porous medium with strong temperature gradients," Transport in Porous Media, 21, (1995), pp. 101-122.

62. Thome, R. J., and Tarrh J. M., MHD and Fusion Magnets: Field and Force Design Concepts, John Wiley and Sons, Inc., New York (1982).

63. Pecharsky, V. K. and Gschneidner Jr., K. A., Journal of Applied Physics, 86, (1999), pp. 6315-6321.

64. Daney, D. E., "Regenerator performance with noble gas mixtures," Cryogenics, 31, (1991), p. 854.

65. Ogawa, M., Li, R., Hashimoto, T., "Thermal conductivities of magnetic intermetallic compounds for cryogenic regenerator," Cryogenics, 31, (1991), p. 405.

66. Patankar, S. V., Numerical Heat Transfer and Fluid Flow, Hemisphere Publishing Company, New York, (1980).

67. Callen, H. B., Thermodynamics and an Introduction to Thermostatistics, John Wiley and Sons, New York, (1985).

68. Jiles, D., Introduction to Magnetism and Magnetic Materials, Chapman and Hall, London, (1991).

69. Chikazumi, S., Physics of Magnetism, John Wiley and Sons, New York, (1964).

70. Reid, C., Development of Magnetic Refrigerants for Active Magnetic Regenerative Refrigerators, M.A.Sc. Thesis, University of Victoria, (1995).

71. Taussig, C., Gallagher, G., Smith, J., Iwasa, Y., "Magnetic refrigeration based on magnetically active regeneration," Proc. 4th International Cryocooler Conference, (1986).